Improved Energy Landscape Reconstruction and Imaging of Nucleic and Amino Acids via Atomic Force Microscopy

by

Patrick R. Heenan

B.A., University of North Carolina, 2013 (Computer Science)

B.S., University of North Carolina, 2013 (Physics)

M.S., University of Colorado, 2017 (Physics)

M.S., University of Colorado, 2017 (Computer Science)

A thesis submitted to the

Faculty of the Graduate School of the

University of Colorado in partial fulfillment

of the requirements for the degree of

Doctor of Philosophy

Department of Physics

2019

ProQuest LLC
789 East Eisenhower Parkway
P.O. Box 1346
Ann Arbor, MI 48106 - 1346

This thesis entitled:
Improved Energy Landscape Reconstruction and Imaging of Nucleic and Amino Acids via Atomic Force Microscopy
written by Patrick R. Heenan
has been approved for the Department of Physics

_____
Prof. Thomas Perkins

_____
Prof. Thomas Cech

Date _____

The final copy of this thesis has been examined by the signatories, and we find that both the content and the form meet acceptable presentation standards of scholarly work in the above mentioned discipline.

Heenan, Patrick R. (Ph.D., Physics)

Improved Energy Landscape Reconstruction and Imaging of Nucleic and Amino Acids via Atomic Force Microscopy

Thesis directed by Prof. Thomas Perkins

Atomic force microscopy (AFM) is a technique widely used to image or apply forces to surface-bound biomolecules in liquid. Traditional methods for imaging DNA and protein-DNA complexes in liquid have drawbacks: DNA conformations with an anomalous persistence length, low SNR, and/or ionic conditions detrimental to preserving native protein-DNA interactions. Here, we introduce a minimally perturbative method for imaging surface-bound DNA that improves data quality and quantity. In comparison to prior protocols, an eight-fold larger fraction (90%) of 680-nm-long DNA molecules were quantifiable, and the technique is viable for imaging DNA of many lengths and proteins in a variety of physiological buffers. In addition to improving AFM imaging, this work also advances the reliability and accuracy of single-molecule force spectroscopy (SMFS) AFM experiments. In particular, recent improvements in time resolution and data throughput of SMFS experiments highlight the need for high-precision, automated characterization of force-induced intra- and inter-molecular bond ruptures. We describe a new algorithm to automatically identify the locations of molecular ruptures in SMFS data. In order to improve molecular energy landscape characterization, we also applied the inverse Weierstrass transform to SMFS data and removed the energy associated with the AFM force probe, yielding the molecular free-energy landscape. Combined, these improvements in AFM methodology – minimally perturbative imaging of DNA-protein complexes, automated detection of molecular rupture events, and energy deconvolution of force probes – advance the quality and reproducibility of biophysical insights gained from AFM-based experiments.

Dedication

To Mom, my first and most important teacher.

Acknowledgements

I owe a vast debt of gratitude to my adviser, Tom Perkins. His ceaseless patience, constant empathy and advice when things weren't working, infectious excitement when things were working, and dedication to the craft and communication of science dramatically improved my capacity for research and research presentation.

In addition to Tom, other members of the Perkins lab provided camaraderie and specific contributions. Lyle Uyetake taught me many experimental, bulk molecular biology techniques. Matt Siewny gave me my first imaging and force spectroscopy tutorials. William 'John' Van Patten and Rob Walder taught me surface- and cantilever- functionalization techniques. Devin Edwards was a ceaseless source of advice, wetlab help, and debugging suggestions. Stephen Okoneiwski and David Jacobson provided constructive criticisms and sympathetic ears.

The professional staff of JILA deserve special recognition for their roles. The machine shop and clean room provided timely and robust service. The JILA shipping and purchasing departments ensured timely delivery and receipt of packages, and the custodial staff kept JILA clean and assisted in a variety of unexpected emergencies.

I also wish to acknowledge my friends and family for their less technical but no less important assistance. My partner Chase was an indispensable source of encouragement. In addition, my siblings, Erin and Palmer, and mother, Sarah, were ceaselessly supportive.

Contents

Chapter

Tables

Table

Figures

Figure

Chapter 1

Introduction

1.1 Atomic force microscopy as a platform for biophysical measurements

The complexity of biological systems necessitates simplification in order to develop scientific insight. Since biological processes often bridge multiple scales – from atoms and single molecules to single cells and beyond – the combinatorial complexity of biological interaction confounds simple explanation. Biophysics, or the physics of living systems, leverages the power of physics-based models to develop useful simplifications of complex biological systems. Biophysical approximations provide insight but require trade-offs between model accuracy and generalization. In particular, physics-based models take a reductionist approach, ignoring difficult-to-model behavior and providing insight only for a particular subset of problems. In single molecule biophysics, the physical properties of biological molecules are measured on a per-molecule basis. Due to experimental constraints, single molecule studies are often limited to simpler systems than studies which investigate ensembles of molecules or living cells. In other words, in single-molecule biophysics, the trade-off between reducing complexity and increasing model applicability often results in precisely studying a molecule or set of molecules, but measuring the system in relative isolation, compared to a more complex, native environment.

Despite the simplifications necessitated by single-molecule methods, well-established techniques have yielded decades of impactful research. Fluorescence microscopy excites fluorophore-

labeled molecules, measures emitted light by the fluorophore, and tracks the motion of labeled single molecules[1, 2]. A more complicated technique called fluorescence resonance energy transfer (FRET) microscopy leverages multiple different fluorophores and enables the measurement of inter- or intra-molecular distances [3, 4]. In contrast to passive observation of emitted fluorescent light, single molecule force spectroscopy (SMFS) measures the molecular response to applied force via molecular tethering to a force probe [5–7]. Combinations of SMFS and light microscopy techniques provide additional measurement power at the cost of added experimental complexity. Ultimately, some experimental techniques are more appropriate for certain systems due to trade-offs in sample preparation (*e.g.* necessity for labels) or measurement constraints (*e.g.* instrumental time response) [5].

Atomic force microscopy (AFM, [8]) is a technique widely used to apply forces *or* image surface-bound biomolecules. AFM-based imaging characterizes the properties of DNA and diverse proteins bound to DNA, including RNA polymerase, restriction enzymes, and nucleosomes [9–24]. In addition to imaging, AFM-based single molecule force spectroscopy (AFM-SMFS) has emerged as an important tool in determining the energetics underlying the folding and unfolding of individual proteins [25–28], protein-ligand bond strength [29, 30], and other mechanically robust biological systems [31–35]. This thesis leverages both AFM-SMFS and AFM-based imaging and is motivated by a desire to improve the insights gained from applying energy landscape reconstruction techniques to SMFS data (see Chapters 4 and 5) or physical models to topographs obtained by AFM imaging (see Chapter 3).

A variety of techniques reconstruct energy landscapes or estimate energy landscape parameters by leveraging AFM-SMFS. In Section 1.3, several energy landscape reconstruction techniques are reviewed, and their practical use is demonstrated using simulated data. The equilibrium techniques reviewed are the inverse Boltzmann technique [36] and the so-called 'rate-map' (unfolding rate versus rupture force) approach [37]. Non-equilibrium techniques for energy landscape reconstruction are demonstrated by the Jarzynski equality [38] and the rate map transformation [37].

Figure 1.1: Illustration of AFM imaging operation. (A) A cartoon of a cantilever poised above a surface, where the surface is color-coded according to its height above an arbitrary zero point. A laser (green) reflects off of the cantilever onto a quadrant photodiode. Diagram is simplified and not to scale. (B) As the cantilever moves across the surface, the relative change in cantilever angle is recorded over time as height. (C) Controlling the x and y position of the cantilever (blue line) assigns the height at each particular time (B) to a height (color-coded as in A) at a particular (x,y) position.

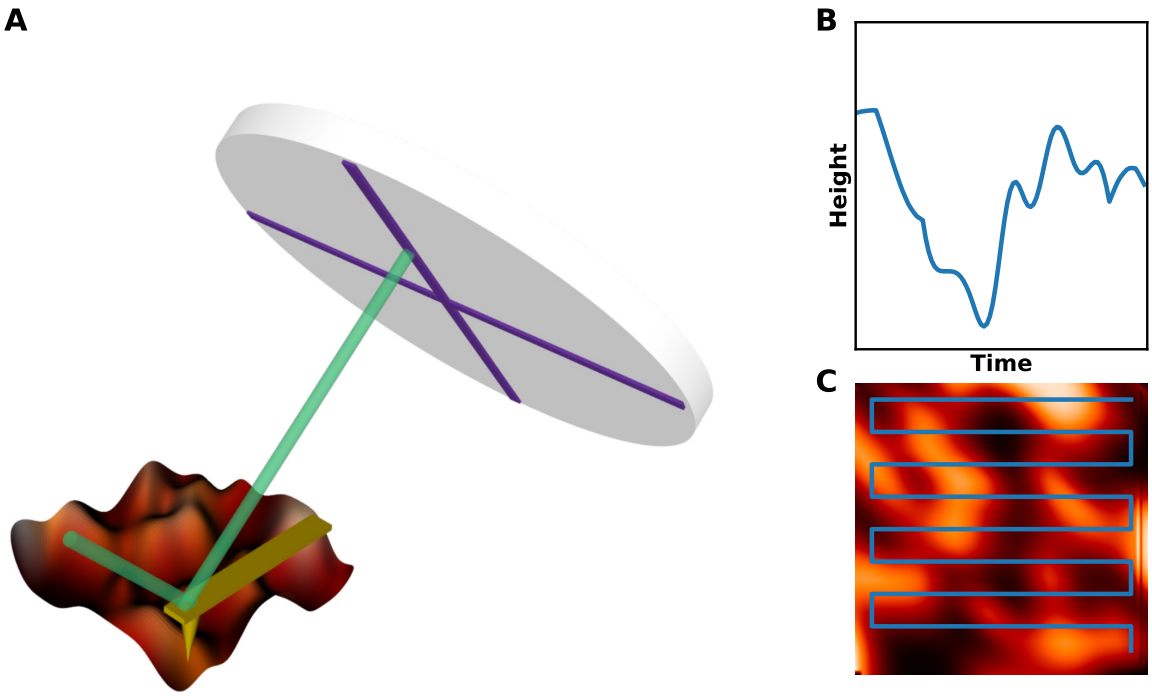

The rate map technique relies on the correct determination of event locations, motivating the automated event detection algorithm of Chapter 4. In addition, the energy associated with the measurement probe convolves with the biomolecular energy of interest and leads to a corrupted energy landscape estimation. Chapter 5 demonstrates the first AFM-based validation of the inverse Weierstrass probe deconvolution algorithm [39]. The goal of automated event detection or probe deconvolution in AFM-SMFS are identical: to obtain biological insights from AFM-SMFS in an unbiased and reliable manner.

In addition to enabling energy landscape reconstruction by SMFS, AFM is a powerful imaging platform for measuring the mechanical properties of surface-bound molecules. AFM requires surface-bound samples for reliable imaging, but adhering a molecule to a surface necessarily reduces molecular degrees of freedom and may perturb native behaviors or structures from their expected values. One well-known surface-induced perturbation of native structure is DNA's distribution of bending angles (*e.g.* Figure 1.4 *B*). In particular, air-based AFM imaging gives the expected distribution of DNA bend angles [40], but liquid-based AFM imaging historically observes a wider distribution of bending angles [23]. In other words, AFM imaging of DNA in liquid has historically measured excessively bendy or flexible DNA, as compared to other bulk or single-molecule methods. Chapter 3 demonstrates that the spuriously high apparent flexiblity of DNA is due to the details of the surface-DNA binding, and Chapter 3 provides a simple method for liquid imaging of surface-bound DNA while obtaining the correct DNA bending angle distribution. In addition, the imaging and deposition method is compatible with many protein systems and therefore provides a high signal-to-noise method of imaging protein-DNA interactions in liquid.

1.2 Liquid imaging of biomolecules via atomic force microscopy

In AFM-based imaging, light is reflected off of a microscopic cantilever onto a detector (Figure 1.1 *A*). Nanoscopic movements of the cantilever are recorded as changes in the position of the

Figure 1.2: Atomic resolution AFM images of the mica lattice are consistent with its expected crystal structure. (A) AFM images of the mica lattice. From left to right, each successive image is twice as large as the first, which is 5 nm by 5 nm. (B) Simplified diagram of the mica lattice, with the two canonical lattice vectors denoted by a and b. (C) The Fourier transform of the AFM images in the a direction ($\hat{a}$) yields a strong signal near the expected lattice spacing based on the crystal structure [41]. (D) As panel C, but for the $\hat{b}$ direction.

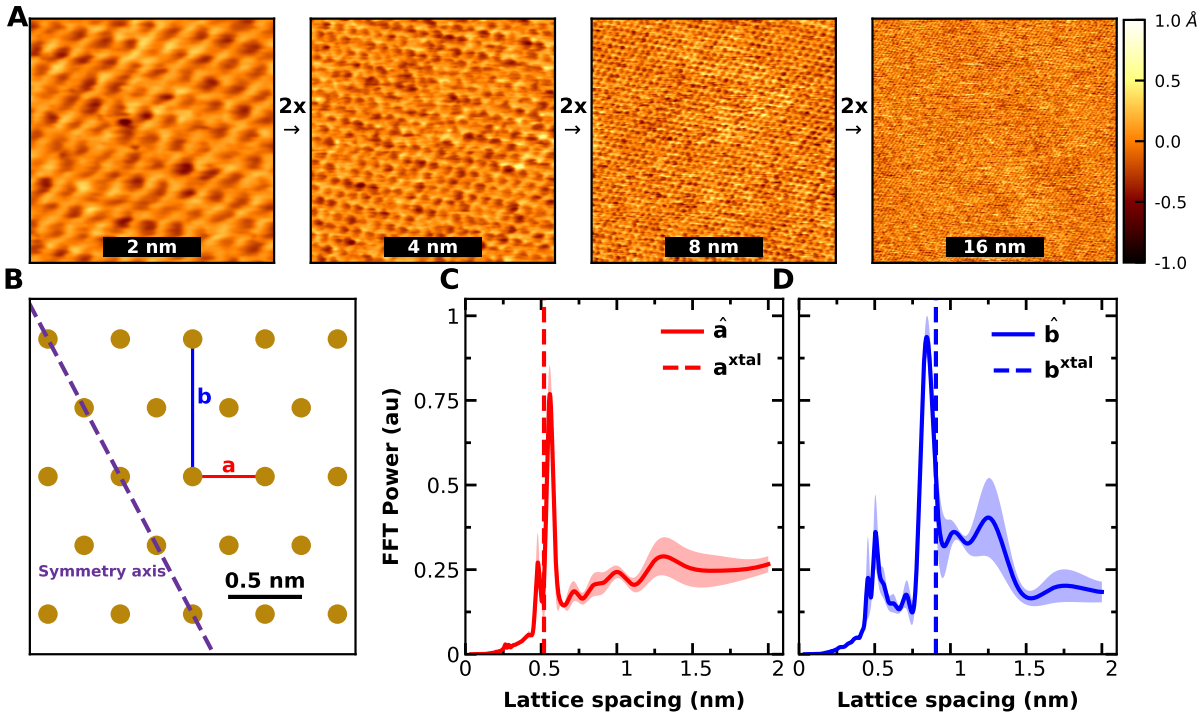

reflected light (Figure 1.1 *B*). Height topography, or assignment of a particular height over a two-dimensional matrix of positions, is measured by controlling the position of the cantilever in the xy-plane of the surface (Figure 1.1 *C*). For imaging discussed in this work (except Figure 1.2), 'tapping mode' imaging will be used, in which the cantilever is transiently in contact with the surface [42]. Tapping mode is generally more gentle than contact mode imaging, in which the AFM cantilever is in constant, high-force contact with a surface.

High signal-to-noise images of surface-bound biomolecules require low surface roughness and a surface binding strong enough to withstand typical imaging forces. Muscovite mica and glass are two common substrates for AFM imaging of biomolecules due to their relative flatness and versatility in binding mechanisms. Glass can be etched to achieve nanoscopic smoothness (Figure 1.3) and functionalized with various groups, as described in Chapter 4. Mica is a common substrate for AFM imaging due to the ease of cleaving mica along its 001 plane and obtaining an atomically flat surface (Figure 1.2) [9, 10, 43–47]. In addition, cleaved mica has a slight negative charge [41], which enhances adsorption of positively charged molecules, and the method of Chapter 3 describes how mica's surface charge can be flipped and thereby enables adsorption of negatively charged molecules. Reversing the surface charge polarity of mica typically relies on ion-exchanging mica's K^+ ions with a divalent cation [47] or coating the mica in positively charged polymers [48]. Since many biomolecules of interest are negatively charged at physiological pH (*e.g.* DNA, many proteins), the ability to switch the polarity of mica's surface charge is critical for strongly binding a diverse set of molecules to the surface and obtaining high-quality images.

The application of mechanical or polymeric models to AFM images yields biophysical insight. For extended polymers made up of N approximately straight segments of length l_i, the contour length, L_0, is $L_0 = \sum_{i=1}^{N} l_i$ (Figure 1.4 *A*). Segment bending is quantified by measuring the change in tangent vectors along the chain, $\theta(s)$, as a function of arc distance $s = \sum_j l_j$, where 'j' runs over the segments of interest (Figure 1.4 *B*). For a two-dimensional worm-like chain with segment length l, the quantity $\frac{l}{\sigma_\theta^2}$ is known as the persistence length p, where σ_θ is the standard deviation of

Figure 1.3: Surface roughness of glass depends on treatment. The surface roughness, defined as the standard deviation in surface height, is plotted for (from left to right) untreated glass, glass subjected to a potassium hydroxide (KOH) treatment, and KOH-treated glass immersed in a solution of silane-PEG (poly-ethylene glycol) for the indicated time, as described in Chapter 4. Images above the plot are representative of their respective conditions. The approximate roughness of mica is plotted as a horizontal line (see Figures 1.2 and 3.17).

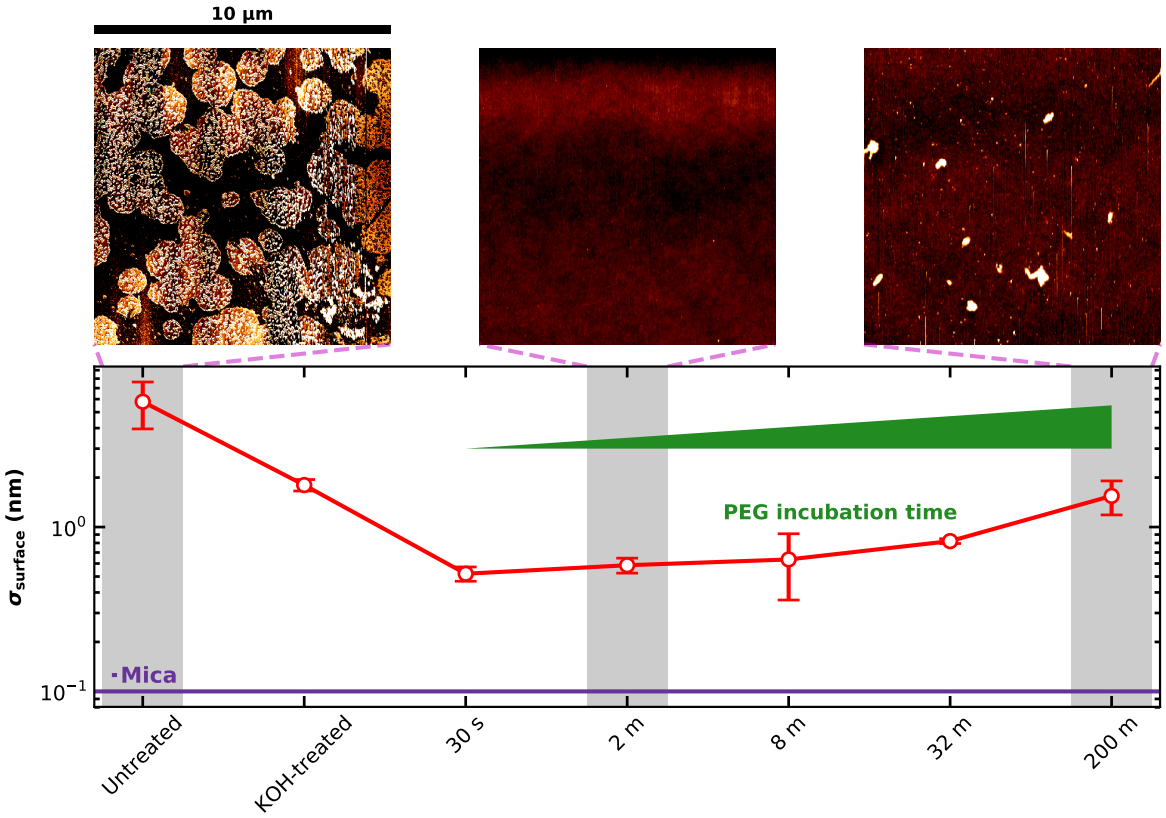

$\theta(s)$ (Figure 1.4 *B*, inset) [40]. The persistence length can also be estimated by the average squared end-to-end distance, $< R^2 >$, as a function of the arc length s between the points (Figure 1.4 *C*) [40].

Volumetric and areal measurements complement the polymeric measurements of L_0, p, and R^2. The width of a polymer, $w(s)$, may vary along the arc and provide evidence of morphology changes in the sample (*e.g.* binding partners, polymer isoform changes, polymer movement) (Figure 1.4 *D*). The width along the contour is quantified by establishing a direction perpendicular to the contour, $s_\perp$. For $s_\perp$ of length $2L_\perp$, given a position $p_s = [x, y]$ along the arc and angle $\theta(s)$, we define $s_\perp(s) = p_s + ds \cdot [\cos(\frac{\pi}{2} + \theta(s)), \sin(\frac{\pi}{2} + \theta(s))]$ for ds which varies from -$L_\perp$ to $L_\perp$. In other words, $s_\perp$ at a particular point p_s at an arc length of s is a line perpendicular to the arc tangent at p_s (Figure 1.4 *E*, colored lines). The height along this direction, $h(s_\perp)$, defines the cross section along the contour (Figure 1.4 *E*, inset), and the maximum height also provides a useful measurement for polymers with known diameters, such as DNA (Figure 1.4 *F*).

Figure 1.4 *(following page)*: Quantification of polymeric and geometric properties using AFM imaging. (A) (Top) Cartoon of a simulated 650-nm DNA molecule with a two-dimensional persistence length, p, of 50 nm. (Bottom) Dotted blue line represents the segments which sum to the contour length, L_0. (B) (Top) The angle between two tangents separated by contour (arc) length, s, is defined as $\theta(s)$. (Bottom, left) The distributions of bending angles for values of s as indicated. (Bottom, right) Despite the changing variance of the bending angle distribution, the ratio of the arc length s to the variance in the angle at a constant s remains constant. (C) (Top) Illustrative definition of the end to end distance, R, between two points A and B. (Bottom) The average value of R^2 (blue circles) follows the expected distribution for a two-dimensional worm-like chain (green line, see [40]). (D) A heatmap-style topograph, where color is proportional to height, of a polymer with an apparent bulge (bright area). Green arrows illustrate the dependence of the width of the polymer on arc length. (Inset) Width of the polymer as a function of arc. (E) As (D), except three colored lines perpendicular to the contour, $s_\perp$, illustrate the variability in cross-section. (Inset) The height along each colored line demonstrates that the cross-sectional area changes as a function of arc length. (F) Three-dimensional image of the region near bulge, with magenta line overlayed at the maximum height along the contour, $h(s)$, as indicated by the pink arrow. (Inset) The height as a function of arc length quantifies the increase in height of the bulge relative to the rest of the polymer.

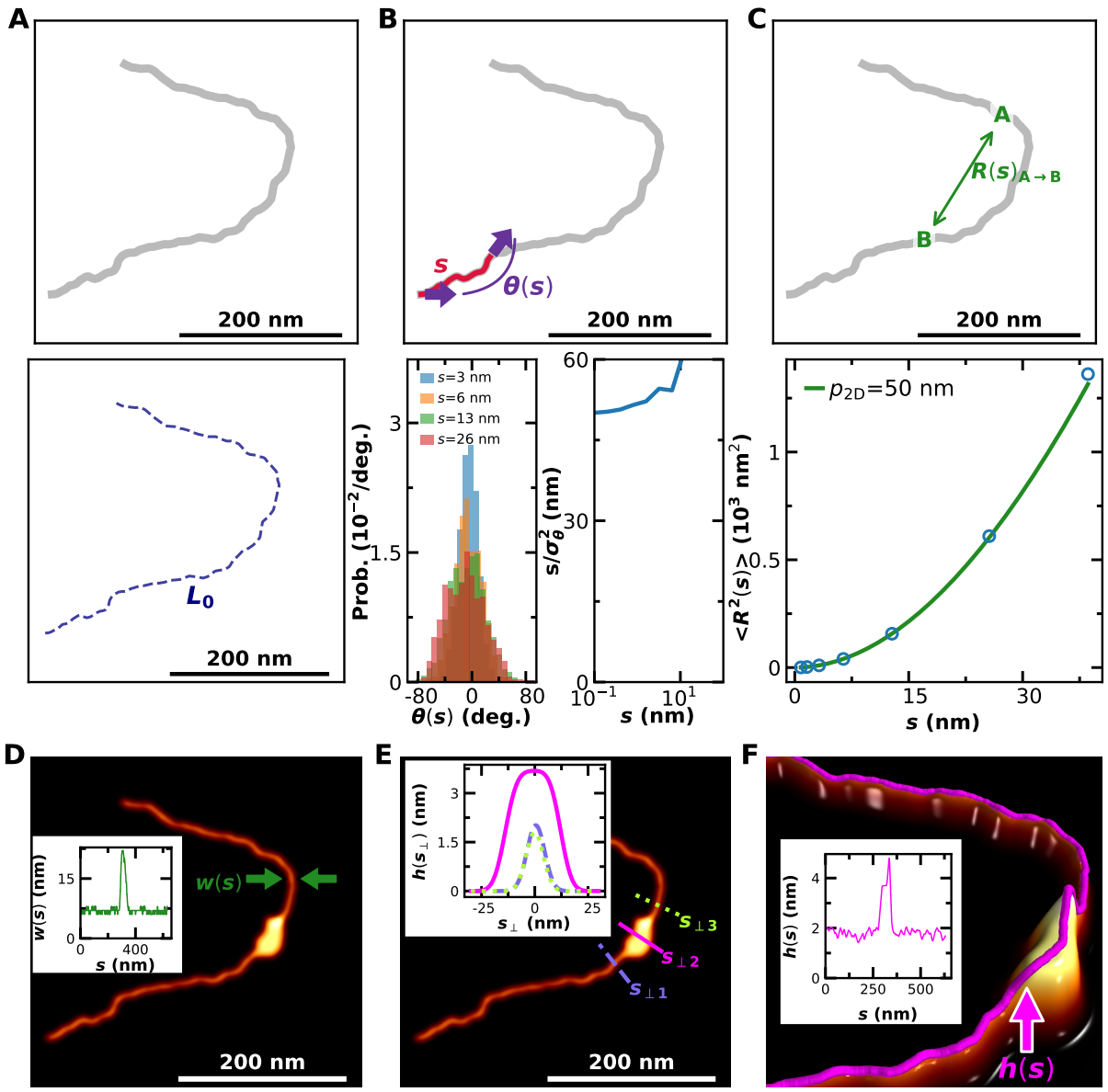
A
B
C
200 nm
s
θ(s)
A
B
R(s)A→B
L0
s=3 nm
s=6 nm
s=13 nm
s=26 nm
Prob. (10−2/deg.)
θ(s) (deg.)
s/σθ2 (nm)
s (nm)
p2D=50 nm
<R2(s)> (10³ nm²)
D
E
F
w(s)
w(s) (nm)
h(s⊥) (nm)
s⊥ (nm)
s⊥3
s⊥2
s⊥1
h(s) (nm)
h(s)

1.3 Single molecule force spectroscopy and energy landscape reconstruction

This section reviews techniques for energy landscape reconstruction used in this work. The techniques described are not comprehensive of the entire field, since it ignores some data collection methods (*e.g.* force-jump techniques [49]) and data analysis methods (*e.g.* the Crooks fluctuation theorem [50, 51]).

Experimental limitations of SMFS data typically require projecting free energy landscapes to a single dimension. Since most biomolecules have many atoms (and therefore many degrees of freedom), a one-dimensional projection is an enormous simplification but often a useful one [7, 53–55]. Figure 1.5 is an example of a one-dimensional free energy landscape as a function of the molecular extension. Local minima in the energy landscape are sequentially numbered with a state index 'i', and arrows denote energy differences or distances to adjacent transition states. As shown in the inset in Figure 1.5, the local free energy between a state and an adjacent barrier is well-approximated by the 'linear-cubic' model [52]. The free energy difference and extension change between a state i and the barrier to state j are denoted by $\Delta G_{ij}^{\ddagger}$ and $\Delta x_{ij}^{\ddagger}$, respectively.

Estimations of $\Delta G_{ij}^{\ddagger}$ and $\Delta x_{ij}^{\ddagger}$ are enabled by identification of transitions between states i and j in SMFS data. Applying a force F at an extension x tilts the free energy landscape by $-F \times x$, biasing the diffusion of the molecule along the landscape in a particular direction. In other words, the application of force in an SMFS experiment biases the frequency of transitions k_{ij} and the states i and j. Since forward and reverse transitions are both possible (*i.e.* $i \rightarrow j$ and $j \rightarrow i$), SMFS experiments which sweep over a broad range of forces (and therefore a range of $k_{ij}(F)$) more accurately measure the distances and energy differences associated with the relevant transitions. The sections that follow detail three techniques for SMFS data acquisition and analysis which apply forces, tilt the landscape, and thereby either reconstruct an entire energy landscape or estimate $\Delta G_{ij}^{\ddagger}$ and $\Delta x_{ij}^{\ddagger}$.

Figure 1.5: Illustrative definition of energy landscape parameters. A free energy landscape is shown as a function of molecular extension (blue line), with parameters taken from [37]. From state 'i' to state 'j', color-coded arrows denote the transition energy differences, $\Delta G^{\ddagger}_{ij}$, and the transition distances, $\Delta x^{\ddagger}_{ij}$. Note that states correspond to well minima. (Inset) A fit to the final barrier (blue) demonstrates the general applicability of the linear-cubic model [52] for approximating a local energy barrier.

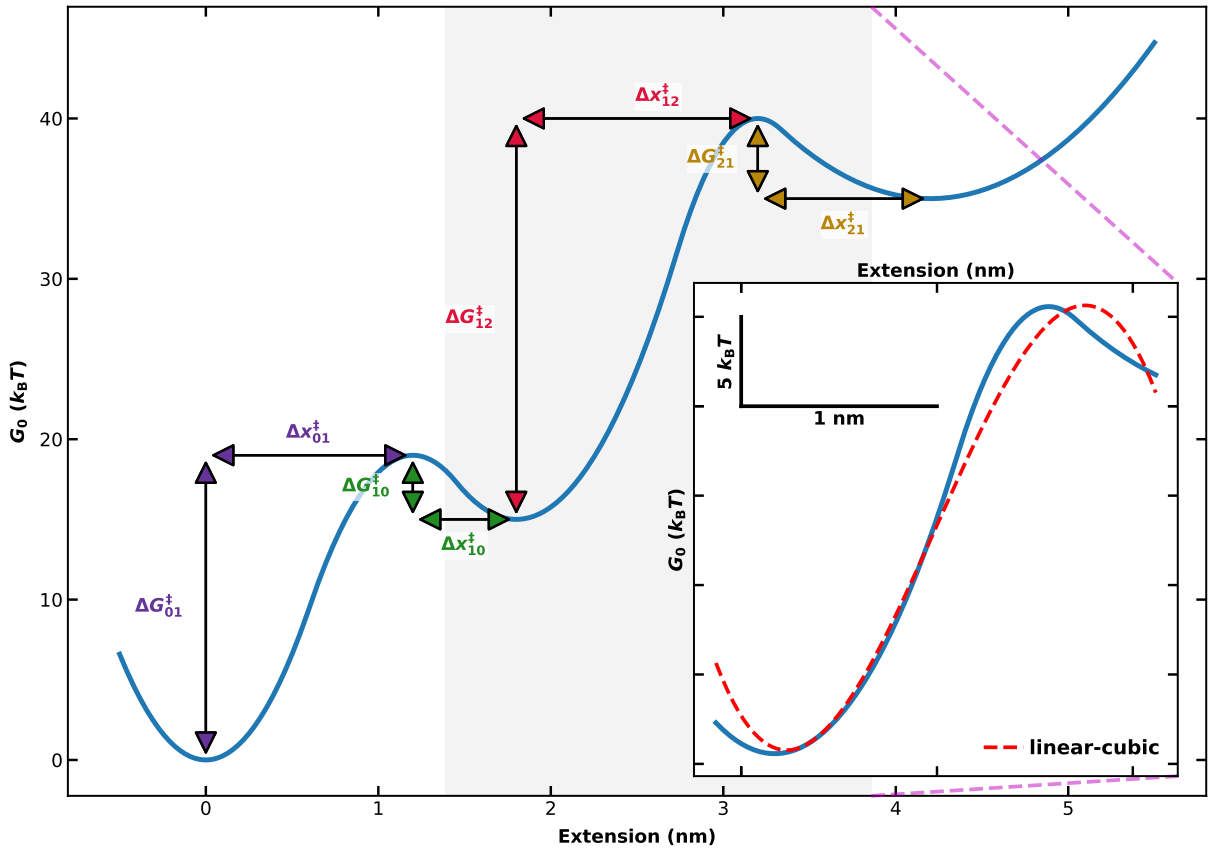

1.3.1 Equilibrium techniques for energy landscape analysis

A straightforward method of energy landscape estimation applies a constant force F at a temperature T and measures the probability of a molecule to be found over a range of extensions, $P(x)$ (Figure 1.6 *A*). From elementary statistical mechanics, the energy, $G(x)$, can be calculated from Boltzmann statistics up to an arbitrary zero energy constant:

$$G(x) = -k_{\mathrm{B}}T \cdot \log P(x) \tag{1.1}$$

where k_{B} is the Boltzmann constant. In practice, the observed extension distribution is widened by its convolution with the point-spread function of the measurement probe, $S(x)$ (Figure 1.6 *A*). However, the observed extension can be deconvolved using the following relation [36]:

$$p_{i+1}(x) = p_i(x) + r_0[1 - 2|p_i(x) - \frac{1}{2}|][P(x) - S(x) \times p_i(x)] \tag{1.2}$$

where r_0 is a relaxation constant, the initial condition is the measured extension (*i.e.* $p_0(x) = P(x)$), and '$\times$' represents Fourier convolution. The point spread function can be approximated by measuring the extension distributions of the system in the absence of any transitions and modeling the distribution as a Gaussian function with the measured width. Once the point spread function has been measured, iteratively removing it is straightforward (Figure 1.6 *B*), assuming convergence of the landscape (Figure 1.6 *C*). Once the probability distribution has been deconvolved, the energy landscape is obtained via Equation 1.1, and the landscape can be converted to a free energy landscape by tilting by $F \cdot x$.

In addition to Boltzmann-based reconstruction of equilibrium data, constant-force SMFS data also yield energy landscape barrier heights and distances (Figure 1.5) via unfolding and refolding transition frequencies [37]. The following relationship fits the force-dependent transition rate $k_{ij}(F)$

Figure 1.6: Demonstration of deconvolution of a force probe's point spread function. (A) Plot of the true ($P(x)$, purple solid line) and convolved ($P(x) \otimes S(x)$, dotted blue line) extension probability distributions. Point spread function, $S(x)$, is given as the dashed orange line. (B) Extension probability distributions from iterative deconvolution (*i.e.* Equation 1.2) of the convolved probability distribution in panel *A*. Distributions from earlier iterations are colored darker than distributions from later iterations, as indicated at each order of magnitude. (C) Extension-averaged relative error of deconvolved distributions of panel B demonstrate that the deconvolved probability distribution converges to the correct value. The error is calculated relative to the true extension distribution from panel *A* (*i.e.*, $P(x)$).

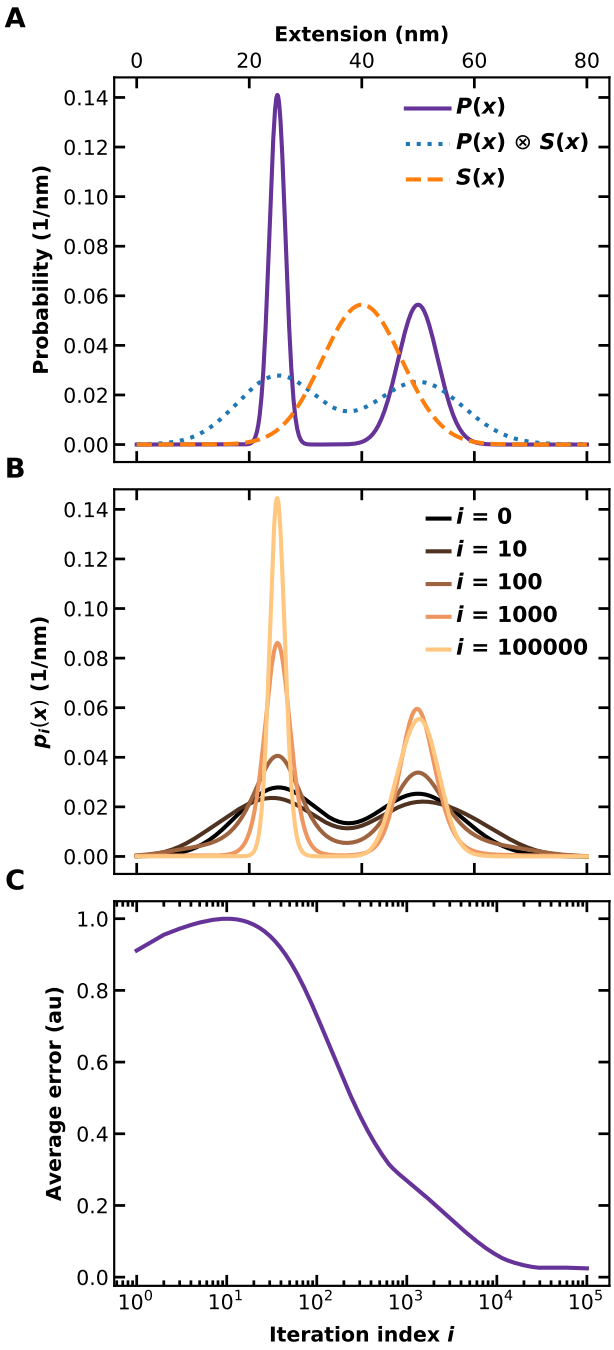

from state 'i' to state 'j' to the distance between the minima of state 'i' and the transition barrier, $x^{\ddagger}$, the zero-force transition rate k_0, and the energy between the minima of state 'i' and the transition barrier $\Delta G^{\ddagger}$:

$$\log(k_{ij}) = \log(k_0) + \{\frac{1}{\nu} - 1)c(F) + \Delta G^{\ddagger}(1 - c(F)^{1/\nu)}\}, \tag{1.3}$$

$$\text{where } c(F) = [1 + \frac{\nu\kappa x^{\ddagger}}{2\Delta G^{\ddagger}} \mp \frac{\nu F x^{\ddagger}}{\Delta G^{\ddagger}}(1 + \frac{(1-\nu)\kappa(x^{\ddagger})^2}{2\Delta G^{\ddagger}}), \tag{1.4}$$

and ν is the barrier shape (either 1/2 or 2/3), κ is the spring constant of the force probe, and $\mp$ is minus for the forward (unfolding) direction and plus for the backwards (refolding) direction. Note that when comparing rate maps from constant force and constant velocity techniques (see Section 1.3.2, below), the force in the constant force measurements, F, should be corrected for the difference of measurement potentials to F' as follows [37]:

$$F' = \frac{F \pm \kappa\frac{x^{\ddagger}}{2}}{1 + \frac{(1-\nu)\kappa(x^{\ddagger})^2}{2\Delta G^{\ddagger}}}$$

where the meanings are as before, except $\pm$ is a plus in the forward (unfolding) direction and a minus in the backwards (refolding) direction. The rates are straightforward to obtain by counting the number and duration of transitions in a force-versus-time trace (Figure 1.7 *A*–*C*). The first and last event must always be ignored, since they provide only a lower bound on the dwell time (or upper bound on the transition rate) for that particular transition. Once the rates are obtained as a function of force (Figure 1.7 *D*), fitting with Equation 1.4 yields the off-rate, energy difference between the state and the transition barrier, and distance to the barrier from the state (Figure 1.7 *E*).

Figure 1.7: Model-based reconstruction of equilibrium single molecule force spectroscopy data. (A) Representative samples of 200 second, simulated traces of extension versus time. Raw data (lighter colors) were generated at 100 kHz, and the darker data are filtered to 1 kHz using a second-order Savitsky-Golay. Data was simulated as described previously [39]. (B) Probability density of unfiltered extensions from column *A*. (C) Probability density of filtered extensions from column *A*. (D) The distributions of unfolding and refolding times, t_{unfold} and t_{refold}, for 200 second, simulated extension versus time traces. (E) The average rate of unfolding (k_{unfold}, red downward triangles) or refolding (k_{refold}, green upward triangles) versus the average of the folding and unfolding forces. Fit of Bell-Evans model to unfolding data (blue dotted line) does not capture the curvature as well as the Zhang-Dudko model [37].

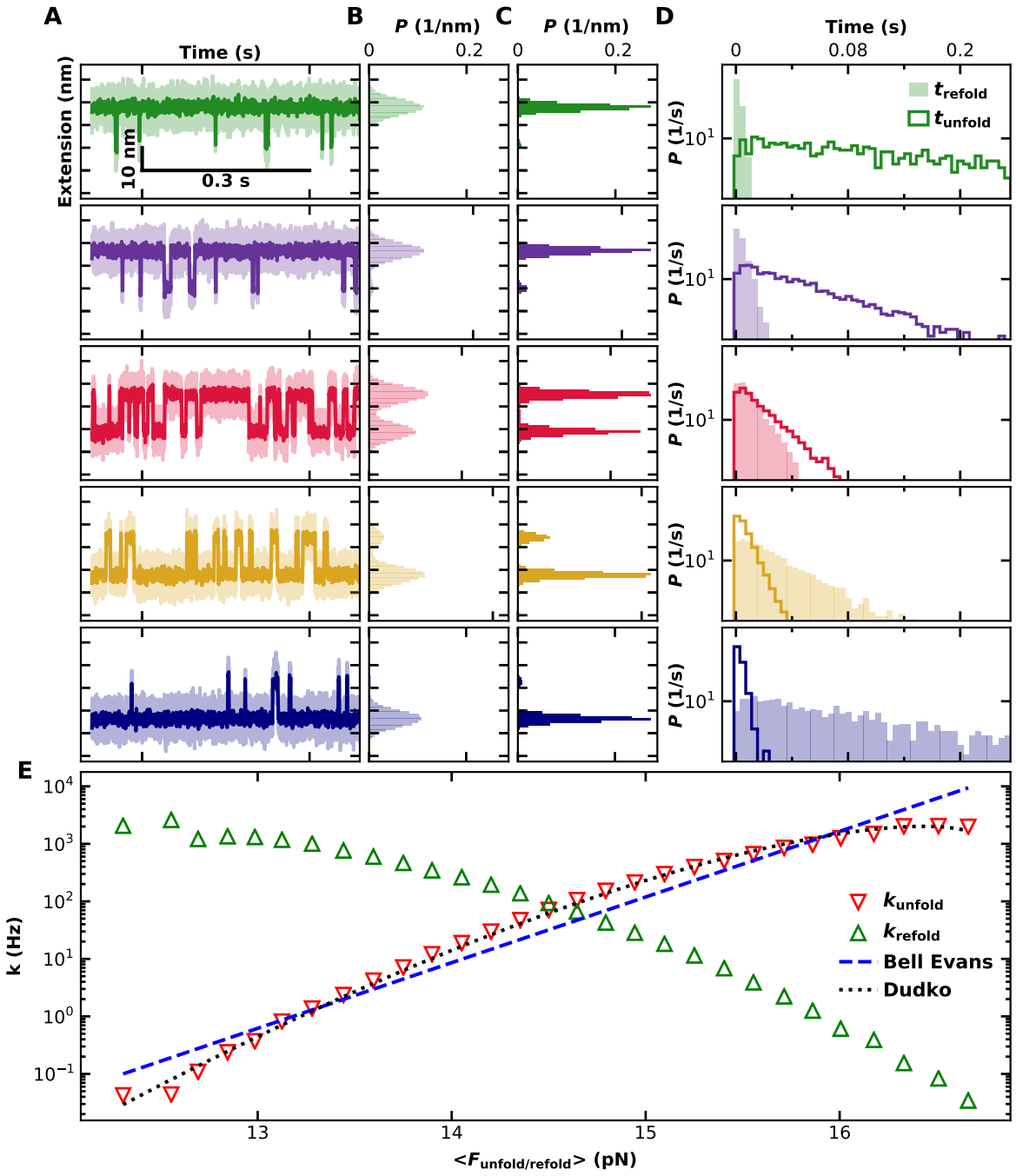

1.3.2 Constant velocity techniques

Constant-velocity measurements provide an alternative method of energy landscape reconstruction or energy landscape parameter estimation. In constant-velocity experiments, or 'force ramps', the force probe bias (*e.g.* AFM cantilever stage position) is changed at a constant velocity. The force-versus-time curves from force ramp experiments are transformed into transition rates by noting that for any particular transition from state 'i' to state 'j' under constant force, the number of molecules transitioning at a particular change in force $P_{ij}(F)|dF|$ must be equal to the number of molecules transitioning over that time period $P_{ij}(t)dt$. But the number of transitioning molecules must be equal to the number of molecules in the state $\mathcal{N}_i(t)$ multiplied by the relevant rate constant $k_{ij}(F(t))$:

$$P_{ij}(F)|dF(t)| = P_{ij}(t)dt = k_{ij}(F(t))\mathcal{N}_i(t)dt \rightarrow \boxed{k_{ij}(F((t))) = \frac{|dF(t)|}{dt}\frac{P_{ij}(F(t))}{\mathcal{N}_i(F(t))}} \tag{1.5}$$

This equation is easiest to understand using several examples at different loading rates. For each loading rate (Figure 1.8 *A*), we record the number of molecules (or independent force-extension curves) in a particular state 'i' at a particular time t, yielding $\mathcal{N}_i(t)$ or equivalently $\mathcal{N}_i(F)$, where F is the average force in a particular state (Figure 1.8 *B*). This requires the accurate detection of

---

Figure 1.8 *(following page)*: Model-based reconstruction of force ramp (constant velocity) single molecule force spectroscopy data. (A) A selection of simulated force versus stage position curves at the nominal loading rates indicated in the lower right. The average force in the folded and unfolded states ($< F(t)_{\text{folded}} >$ and $< F(t)_{\text{unfolded}} >$) obtained from the relevant regions of all curves are shown as red and purple dotted lines, respectively. (B) The population of curves in the folded state, $\mathcal{N}_{\text{folded}}$, as a function of rupture force, F_{R}. (C) The loading rate as a function of rupture force. (D) The number of transitions from the folded to unfolded state, $N_{(F\rightarrow U)}$, as a function of rupture force. Note that this is equal to $\Delta F \cdot P_{N\rightarrow U}$ in the theory parlance [37], where ΔF is the bin size. (E) The unfolding rate as a function of rupture force. (F) The concatenation of all unfolding rate data from panel E, where the colorbar gives the nominal loading rate. (G) Fitting the data from panel (F) to the Bell-Evans model [56] and Zhang-Dudko model [37] (blue solid line, black dotted line, respectively) to all of the data from panel (F) demonstrates the improved fit of the Zhang-Dudko model.

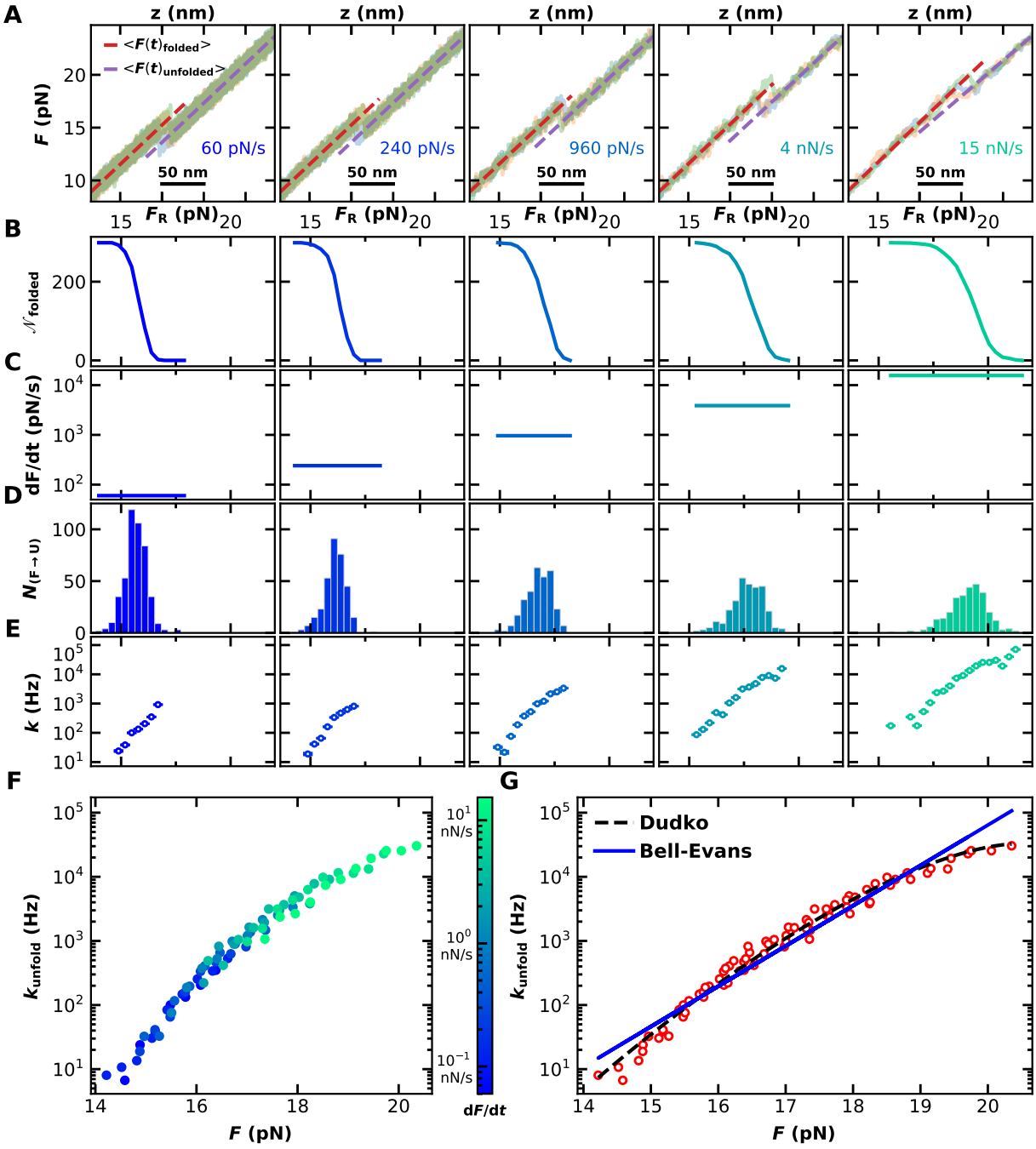
A
z (nm)
<F(t)folded>
<F(t)unfolded>
F (pN)
60 pN/s
240 pN/s
960 pN/s
4 nN/s
15 nN/s
50 nm
FR (pN)
B
Nfolded
C
dF/dt (pN/s)
D
N(F→U)
E
k (Hz)
F
kunfold (Hz)
F (pN)
dF/dt
10^1 nN/s
10^0 nN/s
10^-1 nN/s
G
Dudko
Bell-Evans

transition events for every force-versus-time curve at each loading rate tested, which is the subject of Chapter 4. With the transition events in hand, the force-versus-time curves in a particular state are combined to yield the average force and loading rate in that state at all times where there is a rupture (Figure 1.8 *A*). The state-specific average loading rates and rupture forces as a function of time facilitate calculating the loading rate ($\frac{|dF|}{dt}$, Figure 1.8 *C*) and *unnormalized* distribution of rupture forces ($P_{ij}(F(t))$, Figure 1.8 *D*) as a function of time or rupture force F_{R}. Importantly, $P_{ij}(F(t))$ is the number of transitions at that particular rupture force divided by the force bin width. Therefore, the entire distribution will **not** generally sum or integrate to one. With $P_{ij}, \frac{|dF|}{dt}_i$, and F_i in hand, Equation 1.5 yields the rate map as a function of force (Figure 1.8 *E*–*F*) and fitting equation 1.4 yields the relevant energy barrier parameters (Figure 1.8 *G*).

In addition to transforming non-equilibrium data using the rate map method detailed above, there are well-established techniques for reconstructing the energy landscape as a function of molecular extension. In particular, the basis for the inverse Weierstrass transform detailed in [39] and leveraged in Chapter 5 is the Jarzynski equality [38]. This equality relates the free energy change of a system (ΔG_0) to the measured work, W, as a function of an experimental control parameter 'z' (*e.g.* AFM stage position) as follows:

$$\exp -\beta \Delta G_0 = < \exp -\beta W(z) >_N \approx < W(z) > -\frac{\beta}{2}\sigma_w(z), \tag{1.6}$$

where the average is taken over all members of an ensemble (*e.g.* many force-extension curves), and the equality only holds in the limit of an infinitely large ensemble. The approximation holds in the limit of processes happening close to equilibrium. In addition, this equality assumes an infinitely stiff force probe; when this condition does not hold, the weighted histogram [57] or inverse Weierstrass transform [39] should be used to correct for the effect of the probe. Finally, the landscapes obtained in this manner are still subject to the point spread function of the force probe, and therefore should be deconvolved as described above (Figure 1.6). Table 1.1 lists common

tradeoffs associated with the energy landscape techniques presented in this section.

1.3.3 Benefits and trade-offs of techniques

Figure 1.9: Reconstruction of force ramp experiment using Jarzynski's equality. (A) Simulated force plotted as a function of constant-velocity stage position demonstrates transitions between unfolded and folded states. (B) Heatmap of 50 force-extension curves simulated as in panel A. (C) The mean work (left, purple axis) and standard deviation of the work (red lines, right axis) at each z, where the average and standard deviation are taken over the ensemble. Note that the mean and standard deviation of the work approximate the free energy for high-stiffness probes (see Equation 1.6) (D) The energy, as calculated using the Jarzynski equality (blue, solid line) or its approximation (red, dotted line).

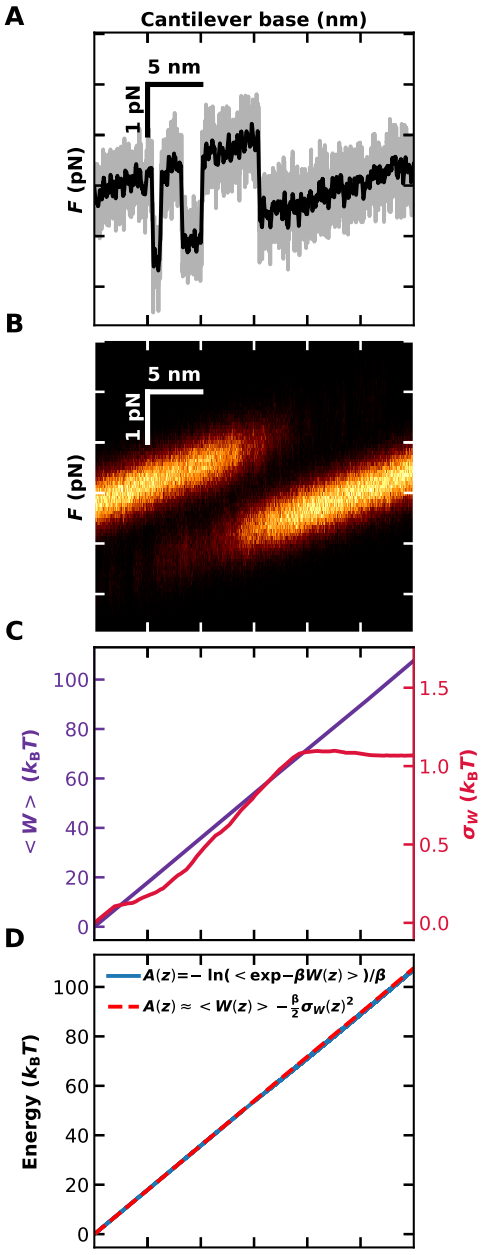

Table 1.1: Comparison of energy landscape techniques.

Technique	Limitations	Advantages
Rate map (Non-equil.) [37]	• Large N ($N_{\mathrm{FEC}} \sim 100$, $N_{\mathrm{tx\,per}\,v} \sim 10^3$) • Large v range needed (∼10-10^4 pN/s) • Requires binning – no analytic transformation to $k(F)$	• Samples $k(F)$ over large F range • Accounts for linker • Generalizes to many states • Necessarily yields kinetics
Rate map (Equilibrium) [37]	• Difficult to access $k(F)$ over range of F • Requires low drift over large time scales • Constant force measurements are technically difficult	• Analytic solution to $k(F)$ • Necessarily yields kinetics
Jarzynski-based reconstructions [38, 39, 57]	• Requires high-stiffness probe • Doesn't yield kinetic or diffusive information [39]	• Yields landscape over region, not just landscape parameters • Better leverages data from folding/unfolding experiments

Chapter 2

Experimental imaging and force spectroscopy protocols

This chapter describes additional details for sample preparation, data acquisition, and data analysis for imaging and single-molecule force spectroscopy (SMFS) by AFM. The information here is intended as a supplemental resource for the details in Chapters 3 and 4.

2.1 Imaging via atomic force microscopy

Atomic force microscopy (AFM) images of nucleic or amino acids are usually obtained by leveraging the atomic flatness and high charge of mica (see Section 1.2) and the capability of AFM to operate in biological buffers. At physiological pH, many molecules of interest (*e.g.* DNA, RNA, and proteins) have the same negative charge as mica [41]. The repulsive force between such negatively charged molecules and the negatively charged mica substrate must be converted into an attractive force to achieve stable imaging of well-bound molecules (see Chapter 3). As detailed in Section 1.2, the three-dimensional topographs obtained via AFM reveal geometric information (*e.g.* width, height, volume), polymeric information (bending angle distributions), and stoichiometric information (*e.g.* binding probabilities as a function of ligand concentration). Below, I describe challenges and advice related to obtaining high-quality AFM images and force curves of biomolecules.

2.1.1 Sample handling and wetlab techniques

Successful AFM experiments require carefully manipulating and recording many parameters (*e.g.* buffer condition, sample concentration, temperature). Often, dozens of individual choices or parameters lead to a particular experimental protocol. Without sufficient foresight, individual choices which previously seemed arbitrary or unimportant may prove critical to reliably obtaining and interpreting high-quality data. When faced with a choice in the laboratory, answering the following questions serves as a useful exercise to help guide decisions:

- How can this choice improve lab safety?
- How can this choice improve reproducibility?
- How can this choice reduce contamination or potential error?

For example, when faced with the question 'should the temperature of an organic solvent used during incubation of surfaces be kept at a known constant?', the answer should be 'yes', since this answer improves lab safety by preventing a potentially hazardous and unmonitored temperature change, reduces experimental error due to temperature variation, and improves reproducibility by ensuring a consistent temperature between subsequent experiments.

Usually, questions regarding safety, reproducibility, and error all have a consistent answer and solution. If a choice ever conflicts (*e.g.* something is reproducible but dangerous), safety should be placed in first priority. If considerations related to safety are at conflict with considerations of error or contamination, a new solution should be designed to avoid this conflict. Below, I record my 'best practices' for increasing the probability of successful experiments and decreasing the risk of danger or experimental contamination.

2.1.1.1 General lab hygiene

Pipettes are used for almost every aspect of work in the lab and therefore deserve special attention. Since accurate volumes are critical for reproducing scientific results, pipettes should be regularly (at least once per year) cleaned and calibrated. If they are contaminated by improper use (*e.g.* accidentally pipetting a large volume of liquid into the internal shaft of the pipette), they should be disassembled; thoroughly rinsed with water, ethanol, and water again; dried; and finally reassembled.

All glass and plastic wear for rinsing or liquid incubation should be thoroughly conditioned in their respective solvents. If a particular piece of glass or plastic will always be dry (*e.g.* a teflon holder for drying slides by N_2 gas), the container should first be rinsed in a compatible solvent, typically water or isopropanol, and then dried with N_2 gas. Prior to use, always check solvent compatibility charts to reduce the risk of contamination. For example, toluene is known to dissolve high density polyethylene, a common ingredient in many plastic containers [58].

Special care should be taken to reduce the risk of environmental contamination from the air or devices used for manipulation. For a long incubation (*e.g.* the three hour functionalization of Chapter 4 in toluene), reduce dust contamination of incubation chambers and solvent evaporation by covering the chambers with an inert material (*e.g.* a glass lid for toluene incubation chambers). In addition, prior to their use, tweezers and other surface- or cantilever- manipulation tools should be cleaned with isopropanol, water, then thoroughly dried by wiping in a KimWipe or application of N_2 gas.

2.1.1.2 Protein

Sample degradation is an often-confounding but easily prevented source of systematic error or experimental failure. Protein samples should generally be stored in an ultra-low (-80 °C) freezer,

Figure 2.1: Deposition of DNA onto $NiCl_2$-treated mica in a dithiothreitol (DTT)-containing buffer. Image of size 2 µm by 2 µm shows DNA bound to a surface prepared as described in Chapter 3, except 1 mM of dithiothreitol (DTT) was added to the usual deposition buffer (10 mM $MgCl_2$, 25 mM KCl, 10 mM HEPES, pH 7.5), before rinsing the surface in the same DTT-containing buffer, and finally proceeding with the rinsing steps outline in Chapter 3. In other words, an extra rinsing step is necessary to prevent DTT coming into contact with and thereby quickly reducing $NiCl_2$.

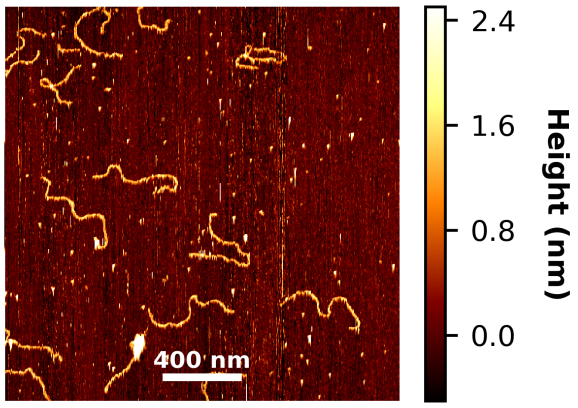

to better preserve properly folded protein [59]. Unless otherwise specified, protein should always be subdivided or aliquotted into smaller volumes at a working concentration, then each aliquot should be individually flash-frozen (often with 10% volume percentage glycerol). When in doubt for how to store a protein, consult prior literature and determine consensus storage parameters. As needed, frozen protein aliquots should be flash-thawed to room temperature and then refrigerated at 4 °C (*i.e.* on ice) to prevent thaw-induced misfolding [60]. For proteins with solvent-exposed cysteine residues, keeping a disulfide-reducing agent present in the buffer is often necessary to prevent oligomerization or misfolding of the protein via non-native disulfide bonds [61]. Note that one common disulfide-reducing agent, dithiothreitol (DTT), also reduces Nickel [62] and therefore is sub-optimal for use in the imaging buffers of Chapter 3. If DTT is required (instead of the Nickel-compatible TCEP), $NiCl_2$ should be replaced by $MgCl_2$ in equimolar amounts in the relevant buffers. Exposing mica pre-treated with $NiCl_2$ (see Chapter 3) to DTT does not appear to affect image quality, as long as all DTT is rinsed before any subsequent $NiCl_2$ is introduced into solution (Figure 2.1).

2.1.1.3 DNA

Degradation of double-stranded DNA by nicking is slowed by storing DNA samples at -20 °C [63]. To further reduce risk of enzymatic degradation of DNA, samples are often stored in a solution of 10 mM Tris (hydroxymethyl) aminomethane hydrochloride (Tris-HCl) and 1 mM Ethylenediaminetetraacetic acid (EDTA) at pH 8. EDTA is a chelator of divalent cations and enhances the stability of DNA, since many DNA-degrading enzymes (DNases) require divalent cations. Freezing, storage, and thawing occurs in the same manner as described above for proteins [64]. Especially for DNA substrates longer then a micron (about 3000 bp), all sample manipulation (*e.g.* pipetting) should be slow and gentle (less than 50 µL/s), to prevent nicking and preserve the population of DNA present during storage. Wide-orifice pipettes may also be employed to reduce the risk of shearing or nicking double-stranded DNA.

2.1.2 Sample deposition

High-quality AFM images require flat surfaces with well-bound samples. To prepare an imaging substrate, a mica disk should be secured with epoxy to a metal disk and stored in a dust-proof container such as a plastic wafer inside of a ParaFilm-sealed pipette box. Dozens of these metal-epoxied mica disks can be made at a single time, and the disks can be stored for months. Prior to this epoxying step, anything touching the mica (*e.g.* the metal disk or plastic wafer) should be air-dried after rinsing thoroughly with water, isopropanol, and water again in order to reduce potential contamination. Before deposition of any sample, imaging surfaces should be rinsed with water and dried with a KimWipe, to reduce dust contamination.

To promote equilibrated attachment, DNA and proteins with acidic isoelectric points (*i.e.* negative charges at physiological pH) are deposited onto mica treated with $NiCl_2$. Before deposition, the DNA and protein (if present) must be mixed to the desired concentrations in the appropriate buffer. For most imaging applications involving DNA, some divalent and monovalent salt will be present. As shown in Chapter 3, DNA is typically well-bound with 10 mM $MgCl_2$ and 25 mM KCl during deposition, but salt concentrations more representative of cellular conditions (3 mM $MgCl_2$ and 50 mM KCl) are also compatible with AFM imaging (Figure 3.11)

In addition to salt concentration, choosing the correct sample concentration is critical for a successful experiment. Deposition concentrations must be chosen to promote a reasonable number of molecules per image (and therefore reasonably high data throughput), but high concentrations will overwhelm the surface and lead to excessive molecular crossings. As a general rule of thumb, the average distance between the center of a molecule and its closest neighbor should be larger than twice the radius of the minimum circle enclosing the molecule, $R_{\min}$, but the average distance between neighbors should not be more than 20 $R_{\min}$. The concentration of DNA is set by the method at about 1.25 ng/uL (or about 1 nM for 2000 bp DNA), and the amount of protein (if present) is determined by the binding affinity of the protein for the DNA and the relative 'background' affinity

of the protein for the substrate. Deposition protein concentrations in the range of 10-1000 nM are typical.

Deposited DNA or protein-DNA complexes must be allowed to relax on the surface to disfavor kinetically trapped states. The imaging protocol described in Chapter 3 necessitates a series of gentle rinses to favor an equilibrated, 2D conformation of DNA (or protein) on the surface and disfavor the so-called 'kinetically-trapped' conformation in which a molecule is poorly bound to the surface and large fractions of its contour are in solution. *Gently* rinse surface-bound samples and never expose them to air, since a receding meniscus is capable of exerting large forces on a surface-bound sample and disrupting binding (Figure 3.12). In the case of surface-bound DNA, forces from partial de-wetting result in an increase in the fraction of kinetically trapped DNA and therefore a decrease in the amount of useful data. Put another way, the rinsing should be laminar and continuous, without any abrupt, macroscopic motion of the liquid droplet off of the surface. If there is any evidence that a surface may have been partially de-wet, the efficient thing to do is to prepare another sample, since sample preparation takes minutes and imaging a sample requires hours or days of time investment. In other words, do not waste time (hours) slowly imaging a surface which may be ruined, since preparing a new surface is relatively fast (minutes).

Surfaces with bound samples may be stored in liquid for use as a positive control at a later date. Care must be taken to avoid de-wetting the surface by adhesion of the water droplet onto any surface (*e.g.* the top of a plastic wafer) or drying the surface by evaporation. Evaporation can be slowed considerably, but not stopped, by placing a surface in a closed, plastic wafer inside of a pipette boxed filled 50-75% with liquid, sealing with ParaFilm, and placing in a 4 °C refrigerator. Over many hours, angstrom-sized precipitates often stably bind to the mica lattice, which increases the background noise (Figure 2.2).

Figure 2.2: Nanoscopic precipitates adhere to mica surfaces after many hours of imaging. (A) 500 nm by 500 nm images of 300 bp DNA taken with an SNL-10A at the indicated times, where the times are relative to the leftmost image. (B) For each image in A, the probability distribution of heights is shown. (Inset) Detailed plot for small heights shows that over time the heights near 0.5 nm become more common, corresponding to the surface precipitates. Note that the images were taken at different spots on the same surface.

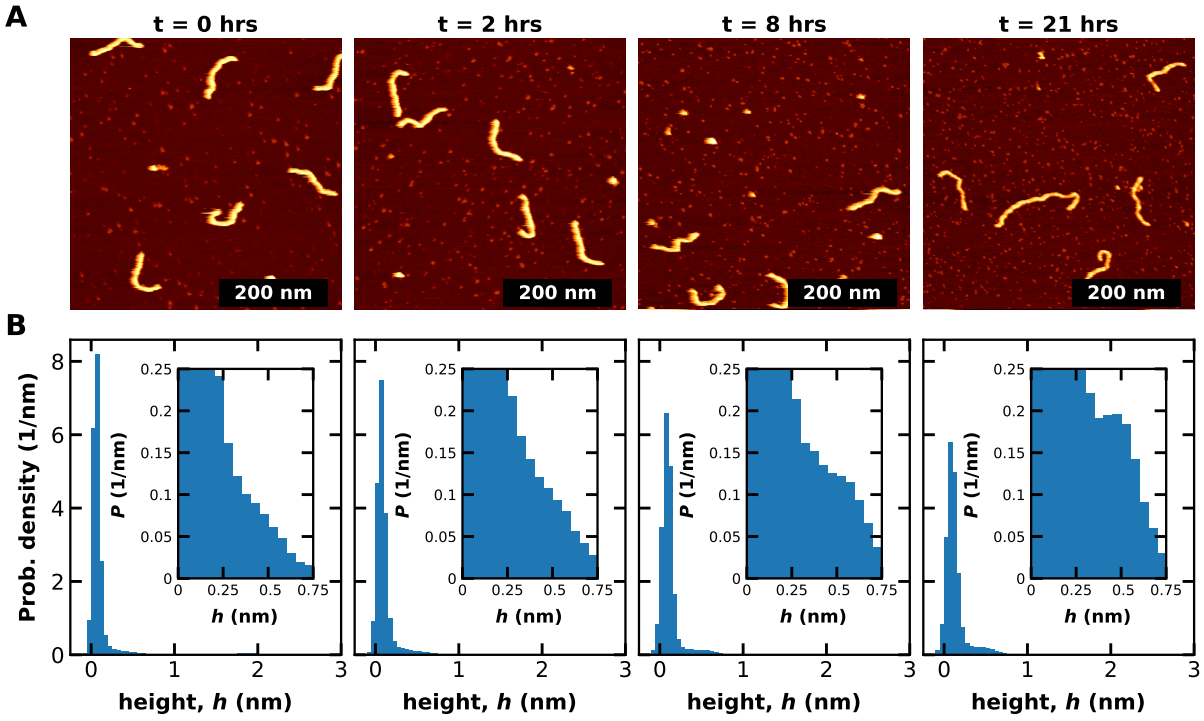

2.1.3 Data acquisition

The acquisition of publication-quality AFM images requires patience and constant attention to experimental details. Figure 2.3 is a flowchart illustrating the essential steps for running an imaging experiment, which we describe in detail below. Once a surface has been prepared as described in Section 2.1.2, the cantilever and surface are loaded. The cantilevers I use most commonly for imaging of DNA or DNA with bound protein are the Bruker SNL-10A and the Olympus BioLever Mini. Each cantilever has different physical characteristics and associated tradeoffs, as detailed in Table 2.1. In particular, the tip radius of the SNL-10A is generally smaller than the BioLever Mini and therefore capable of producing sharper images, but the BioLever Mini is less prone to drift and has a much larger range of achievable imaging amplitudes due to its much smaller size and lower drag.

Table 2.1: Imaging cantilever comparison. Comparing the physical characteristics of the cantilevers used in imaging studies in this work.

Cantilever	**Tip Radius**	**Cantilever Length**	**Benefits**	**Drawbacks**
Bruker SNL-10A	≈ 2 nm	120 µm	• Better resolution	• Easily dulled • High sample pressure • High drift
Olympus BioLever Mini	≈ 8 nm	7 µm	• Less drift • Less sample pressure	• Less reflective area • Poorer resolution

Once a cantilever has been chosen, all parts of the AFM instrument which contact the sample should be cleaned. In particular, since the AFM is not immune to contamination, the cantilever, cantilever holder, and AFM stage must be cleaned. The cantilever holder should always be secured in a housing prior to rinsing, to prevent spilling water onto the electronics. Before securing the cantilever in the cantilever holder, the holder should be thoroughly rinsed with water, ethanol, rinsed again in water, and dried. Unless the cantilever is functionalized, the mounted cantilever can

then be rinsed with water, ethanol, rinsed again in water, dried by application of a KimWipe, then transferred into the final, desired imaging buffer. In addition to reducing potential contaminates such as oil from commonly used cantilever gel packs, thoroughly rinsing the cantilever and cantilever holder helps wash away small (< 1 mm) shards of cantilever which are commonly created when manipulating cantilevers. Without such rinsing, cantilever shards or contaminants will settle onto the surface and potentially create experimental difficulties.

After mounting, rinsing, and transferring the cantilever into the desired imaging buffer, the surface should be centered on the AFM stage, with between 150 and 300 µL of imaging buffer above the surface, assuming a standard 15 mm-diameter metal substrate. Once the surface is mounted, the stage should be raised to accommodate the cantilever and prevent crashing the cantilever into the surface. After securely fixing the cantilever holder (and therefore the cantilever) onto the AFM, the holder is slowly lowered, until the cantilever is fully immersed in the bubble of the imaging surface.

Once the AFM-mounted cantilever is brought into contact with the sample liquid droplet, positioning the cantilever and detection laser focus a few microns above the surface is a pre-requisite for imaging. Any bubbles on the cantilever (observable as shadows in the live video panel) will cause drift and interfere with accurate measurement. Bubbles are removed by wetting and de-wetting the cantilever using the stage motors, or by reloading the cantilever. If the cantilever is re-positioned, the rinsing protocol should be repeated. Once the cantilever lacks any observable bubbles on the live video panel, the cantilever should be positioned about 50 µm above the surface, and the detection laser position should be adjusted to maximize the measured signal (usually by placing the laser in the center of the cantilever). The surface position can be found by sweeping the focus down to the metal substrate (which is highly featured and specular), and then slowly sweeping up until the liquid-mica interface is visible as diagonal lines at the corners of the live video panel.

Figure 2.3: Flowchart for AFM imaging operation. Operation starts at the text with the diamond background, and text to the right of each edge indicates when that edge should be followed. If there is no text, an edge should *always* be followed.

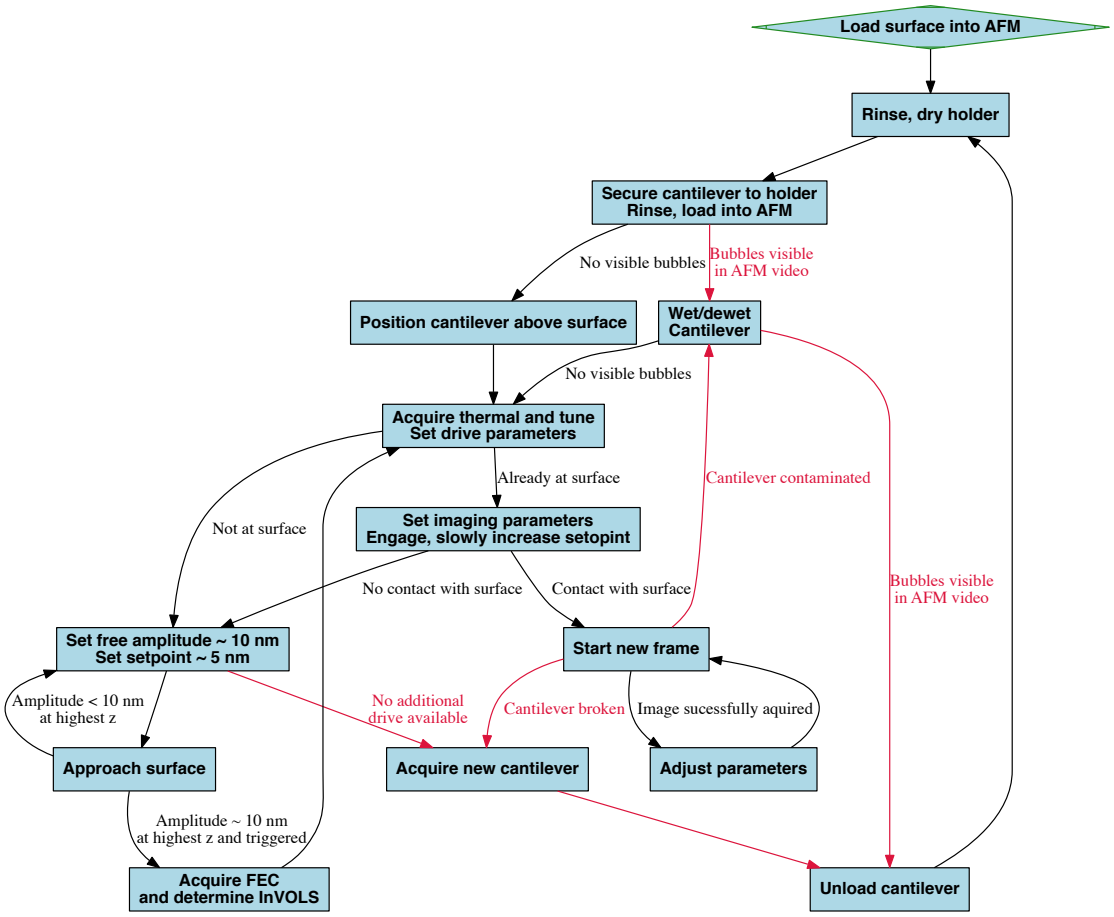

Figure 2.4: Imaging drive frequency should be chosen near the first thermal resonance of the cantilever. (A) The power spectral density (PSD, black) of an SNL-10A in liquid exhibits several resonances. (B) Detailed plot of PSD from panel A (grey, left axis) and deflection amplitude (red, right axis) near the first thermal resonance. Since the cantilever in liquid and many mechanical modes of the AFM are excited, the amplitude has a non-trivial dependence on the drive frequency.

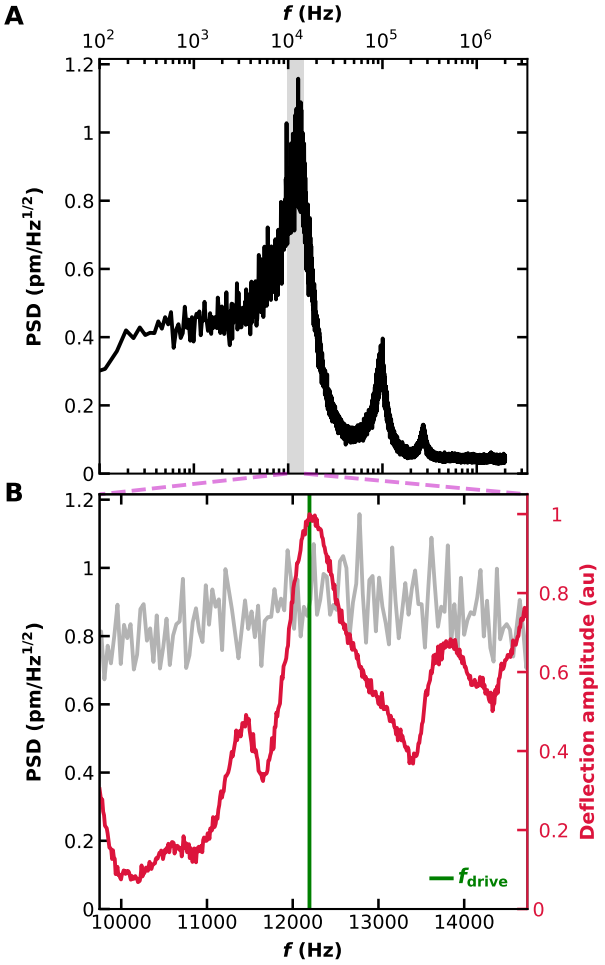

Once the cantilever is positioned above the surface, calibration is required to ensure physically meaningful measurements. A thermal power spectral density (PSD) should be obtained to determine the first resonance frequency of the cantilever (Figure 2.4 *A*). After determining this frequency, a 'tune graph' should be obtained, which is the dependence of the cantilever's deflection amplitude on the frequency applied to the piezo stage (Figure 2.4 *B*). The drive frequency, f_{drive}, should usually be as close as possible to the first thermal resonance frequency of the cantilever (*e.g.* green line in Figure 2.4 *B*). Since the transfer function of the cantilever in liquid is highly non-Gaussian, there may be more than one peak in the 'tune graph' near the first thermal resonance, and in this case multiple images should be taken at the peaks in the tune graph near the first thermal resonance in order to determine the optimal frequency. In other words, if multiple peaks in the tune graph are close to the first thermal resonance, f_{drive} should be chosen to obtain the lowest instrumental background noise.

Armed with a drive frequency close to the first thermal resonance frequency of the cantilever, the cantilever is moved much closer to the surface in preparation for imaging. The surface approach should be AC mode (*i.e.* tapping mode), to prevent damaging the tip by excessive force from a contact-mode approach. By setting the drive frequency close to the first thermal frequency (Figure 2.4), and choosing an approach free amplitude of several nanometers, the cantilever should be responsive during the approach and reduce the risk of damaging the tip. As the tip drops towards the surface, the free amplitude will drop as the cantilever experiences larger drag. As a rule of thumb for surface detection, a free amplitude of 10 nm (*e.g.* roughly 300 mV for an SNL-10A) when the cantilever is positioned several microns above the surface will drop to 5 nm (about 150 mV for an SNL-10A) when the cantilever has found the surface. Therefore, a free amplitude of 10 nm and a set point (indicating the surface position to the AFM) of 5 nm is a reasonable place to start. In general, a 50% reduction in free amplitude over a few microns is a good indicator that a surface has been found.

The surface height topographs obtained via AFM require calibration for physically meaningful

measurements. Once the surface has been reached, the inverse optical lever arm sensitivity (invOLS) should be measured by pressing into the surface a few tens of nanometers (typically several hundred millivolts of deflection). Care should be taken to avoid pressing into the surface too hard (and therefore damaging or blunting the tip) or too soft (and therefore corrupting the invOLS calibration, which requires a hard-contact measurement). When the invOLS is combined with the thermal PSD measurement, the spring constant of the cantilever can be calibrated [65].

After obtaining the first thermal resonance, drive frequency, and invOLS, a cantilever poised a few microns above a surface can be considered 'calibrated' and ready for data acquisition for the purposes of biomolecular imaging. Data acquisition improves over time, especially after the first hour or two, due to settling of the system. Therefore, for high-quality images, the cantilever should be left alone and allowed to 'settle' before image acquisition. Without this initial settling period, images may appear noisy, and cantilever-induced motion of surface-bound molecules may be more pronounced. Before allowing the cantilever to settle for a lengthy period, an image with a 'large' scan size (compared to the expected feature size) should be taken in order to verify the surface is well-populated with the expected sample.

Table 2.2: Imaging suggestions for common systems of interest. Common parameter suggestions for AFM. Note that the mica lattice is imaged in contact mode, so it only has a set point.

Sample	**Scan Size (nm)**	**Scan speed (Hz)**	**Set point (nm)**	**Free amplitude (nm)**	**Integral Gain (au)**
DNA (2000 bp)	2000	2	2	4	60
DNA (800 bp)	1000	2	2	4	60
Bacteriorhodopsin	10000	1	4	7	100
Mica lattice	10	15-30	1-2	N/A	40

After settling, the cantilever set point (the amplitude it will have above the surface once imaging is engaged) should be set to roughly the feature height of interest (Table 2.2). To reduce the risk of destroying a cantilever, the free amplitude should be adjusted to be equal to the set

point prior to imaging. When imaging is started with the free amplitude equal to the set point, the feedback loop controlling the stage position will not lower the stage. Therefore, the drive voltage should be slowly increased, causing the feedback loop to lower the stage and the cantilever to gently engage with the surface. Confidence that the surface has been reached is established by the reproducible appearance of well-defined structures on the surface. Once the surface has been found by slowly increasing the drive amplitude, a new frame should be started to avoid an image partially corrupted by the gentle approach to the surface. This method slowly increases drive voltage (*i.e.* decreases the tip-sample distance for a fixed set point) to avoid damaging the cantilever or sample by abruptly colliding the cantilever with the surface and introducing forces on the scale of nanonewtons.

Different imaging cantilevers and samples necessitate continuous adjustment of imaging parameters. Worse still, from an ease-of-use perspective, the properties of the *same* cantilever or sample may change over time for a variety of reasons. Table 2.2 lists common parameters for an initial image of a few different samples. I emphasize again that these parameters are strongly cantilever-dependent, and typically have to be optimized on a per-cantilever, per-sample, and per-image basis. Table 2.3 lists common tuning decisions for imaging.

2.1.4 Data analysis and processing

Tapping-mode AFM reliably measures the phase and height of a surface and its features, assuming they are well-bound and do not appreciably move on the time scale of image acquisition (Section 1.2). Since both the height and phase are relative metrics, data analysis must choose a zero point. For sparsely populated surfaces, the median value of the height (or phase) provides a reasonable initial estimation of the background height or surface location.

Thorough subtraction of the image background necessitates removing an approximately polynomial instrumental artifact along each scanning line (Figure 2.5 *A*). For many images, particularly

Figure 2.5: Background correction of AFM images. (A) AFM image of a 4000 bp-long DNA molecule. (B) The same molecule, with a dotted line over an image row with instrument-induced 'shadowing'. (C) The height profile along the line shown in panel *B*, where the dark purple heights are thresholded to less than two standard deviations of the entire image from the mean, and the brown line is a third-order polynomial fit to the thresholded data. (D) The same image as panel *B*, except each line has been fit as shown in panel *C* and the fitting polynomial has been subtracted on a per-line basis.

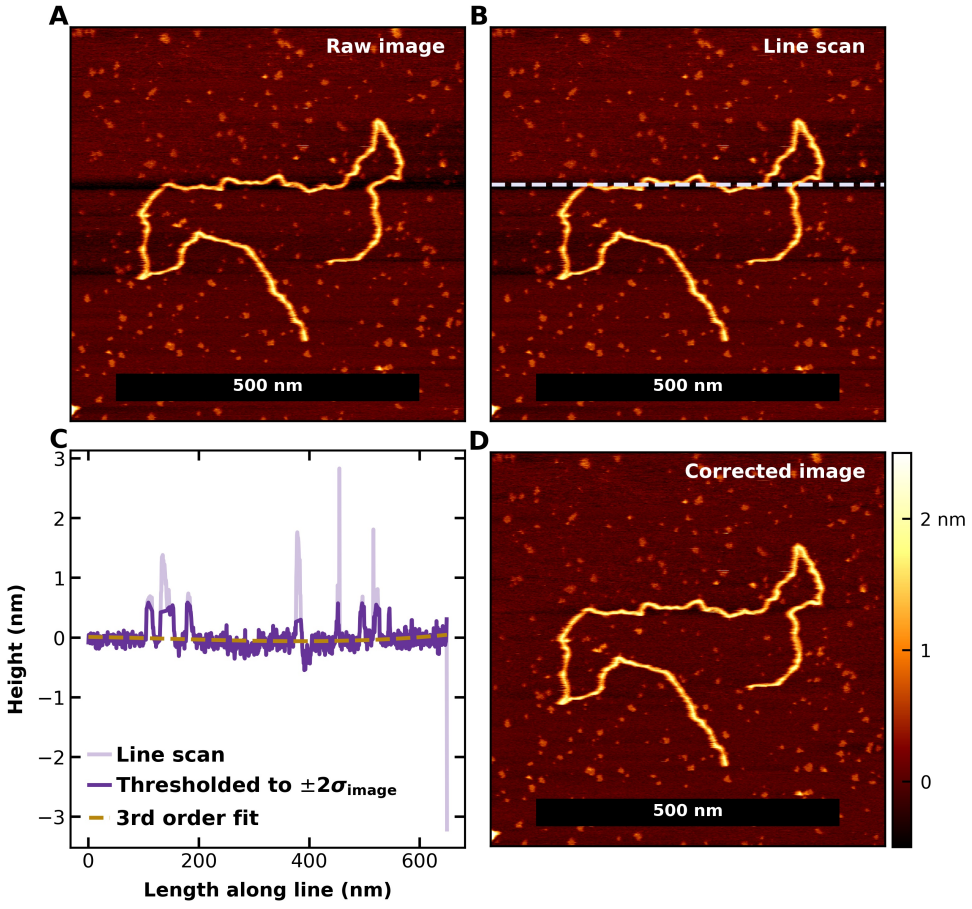

those with large scan sizes or fast scan speeds, the AFM superimposes an approximately parabolic function on the height of each horizontal scan line. In other words, for a given row r, the measured height $h_{r,\mathrm{meas}}(p)$ as a function of pixel number p is approximately equal to $h_{r,\mathrm{true}}(p)+(a+px+cp^2)$, where $h_{r,true}$ is the true height, and the coefficients $\{a, b, c\}$ are related to the interference artifact height superimposed by the AFM (Figure 2.5 *B*).

Once an image is properly zeroed and background corrected (Figure 2.5 *C*), physical parameters are extracted from the height as a function of position on the image (see Section 1.2 and Figure 1.4). For polymeric structures (*e.g.* dsDNA, actin) which have most of their contour along the surface, the contour along the polymer can be measured. This yields the contour length, bend angle, and height of the molecule as a function of distance along the polymer (see Section 1.2). Some algorithms exist for automatically tracing molecular contours [66], but they have difficulties tracing flexible molecules with persistence lengths much less than contour lengths or molecules with significant variation in height (*e.g.* a protein-DNA complex).

In addition to contour-dependent statistics, molecular volumes are approximated by fitting models to the height near a feature of interest. For example, a two-dimensional elliptical Gaussian function with six parameters (height, center in x, center in y, variance in x, variance in y, elliptical angle) is a reasonable model for local fits to DNA or protein-DNA complexes which are well-adhered to a surface. Since the radius of a cantilever influences observed widths of objects on a surface [67], volumes obtained in this manner should be deconvolved [68] in order to estimate absolute volumes or compare between different cantilevers with generally different tip radii. For samples with DNA, one method of decovolution measures the cross-sectional area of the DNA and sets it equal to its expected value (since the radius of DNA is about 1 nm).

Table 2.3: Imaging troubleshooting . Advice and suggestions for imaging via AFM

Problem	**Possible cause**	**Action to take**
Features appear larger or blurrier than expected	Cantilever not in good contact with sample	Increase integral gain or drive amplitude
Features appear thinner than expected	Cantilever applying excessive pressure to sample	Decrease integral gain or drive amplitude
Surface has unexpected, small-scale periodic features	Feedback loop is causing ringing	Decrease integral gain
Surface is sticky or samples attach to cantilever	Cantilever is engaged too hard to the surface	Decrease drive amplitude or raise set point
Image appears unexpectedly featureless	Drive frequency is exciting cantilever noise	Choose a different tune peak close to first thermal resonance
High apparent movement of sample	Cantilever applying excessive pressure on sample	Sweep set point and drive amplitude while keeping their ratio approximately constant
Accumulating < 1 nm tall by ≈ 10 nm wide features	Impure water used in buffers	Replace water filter or use bottled water for rinsing
	Evaporation of imaging buffer	Check AFM holder seal; increase vapor pressure.
Unexpected > 1 nm tall by ≈ 10 nm wide features	Mica cleaved poorly or locally imperfect	Deposit new sample on new mica surface
Sample appears discontinuous	Tip is too sharp	Allow sample to settle, use duller tip
Extreme drift or interference	failure of epoxy between metal and mica	re-make sample
Abrupt loss of surface tracking	Non-specific adhesion of molecule to cantilever	De-wet/Wet cantilever a few times

2.2 Force spectroscopy and landscape reconstruction via AFM

2.2.1 Sample storage and handling

The storage of DNA and protein samples for SMFS is as described in Section 2.1.1.3. In brief, DNA samples should be stored at -20 °C and protein samples should be stored at -80 °C. Liquid samples should always be flash frozen from room temperature, and frozen samples should be quickly thawed on a room temperature block. After thawing, samples should generally be kept at 4 °C prior to use. All experiments are performed at room temperature, which is a chilly 19 °C for the room housing the AFMs.

2.2.2 Sample deposition

The technique for covalently attaching protein or DNA to a poly-ethylene glycol (PEG) coated surface is described elsewhere [69] and in Chapter 4. Here, I provide additional advice for improving data throughput and quality. Briefly, the covalent attachment strategy is:

- Glass is first cleaned and functionalized with a treatment in potassium hydroxide (KOH)
- Cleaned glass is activated by exposure to ultraviolet light
- Activated glass is incubated with a heterobifunctional PEG linker
    - One end of the linker is a silane (for covalent attachment to the glass)
    - One end of the linker is the binding partner for the intended sample (*e.g.* silane-PEG-maleimide for a thiol-labeled protein)
- Solvent-rinsed, PEG-coated glass is incubated with the desired sample

- Excess sample is rinsed away

The functionalization procedure for cantilevers is similar to the surface protocol listed above, except sometimes the cantilevers use a different chemistry (*e.g.* maleimide for the cantilever, azide for the surface).

The most commonly confounding phenotype of problems in a single-molecule force spectroscopy (SMFS) experiment is a lack of attachments. When this happens, there are three possible causes: the sample, the cantilever, or the surface. Combinations of failures are also possible (*e.g.* the surface and tip both fail). Below, I lay out strategies for discriminating between these sources of failure.

Surface functionalization is tested by using a previously-validated cantilever on a new surface, or by incubating test surfaces for an hour in a fluorescent dye labeled with the appropriate chemistry. Figure 2.6 shows that incubating about 600 nM of DBCO-labeled AlexaFluor647 on a surface functionalized with Silane-PEG-Azide gives a strong fluorescence signal relative to a negative control. Good negative controls are an unlabeled glass surface or (better still) a PEG-coated surface with a 'fluorophore-orthogonal' labeling chemistry. For example, a silane-PEG-maleimide surface would be an excellent negative control for a DBCO fluorophore, since there is no expected site-specific binding between the maleimide and the DBCO.

Cantilever functionalization is validated by testing the cantilever on a previously working surface. Typically, DNA surfaces are active for months after successful deposition, assuming they are kept from drying. Hence, DNA positive controls provide a way of considerably reducing the debugging search space, and maintaining DNA controls is critical for reducing time determining the root cause of experimental failure (*i.e.* determining the culprit among the sample, surface, and cantilever). A positive control is *always* a good use of time prior to the day's 'proper' experiments, whether the control validates a 'new' cantilever's activity on last week's surface or tests a 'new' surface using last week's cantilever. Consistently taking time to verify the controls are working *will*

Figure 2.6: Verifying surface functionalization via fluorescence imaging. Fluorescence intensity (red circles, mean ± std. dev.) of silane-PEG-Azide surface as a function of concentration of DBCO-PEG-AlexaFluor647, with representative images above their indicated concentrations. Fluorophores were incubated for 1 hour in PBS on the surfaces before rinsing with PBS. Imaging was carried out with a 652 nm emission filter and 631 nm excitation LED. Green line is a fit of the data yielding a dissociation constant of 620 ± 20 nM (mean ± fitting error), assuming 10 µM was close to the surface saturation point.

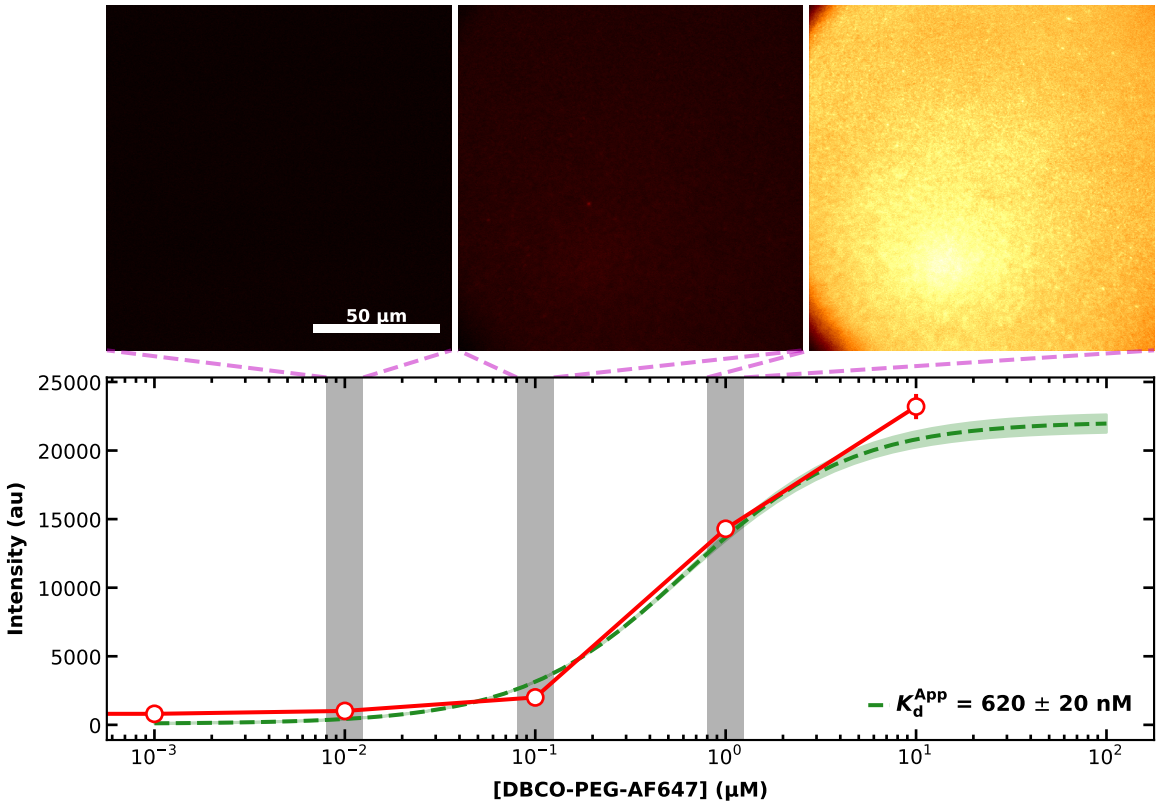

save time, on average.

Bulk methods should be regularly employed to assay sample activity and general 'health'. In particular, since single-molecule experiments are slow, bulk controls should be performed, and a positive result should be obtained before performing single-molecule experiments. For example, an electrophoretic mobility shift assay (EMSA) can easily yield sizes of the largest populations of nucleic or amino acids present in a sample. Unfortunately, EMSA results do not generally give information about the structure of a sample. In other words, the sample may be the correct size but be misfolded or (for enzymes) be inactive. However, including a binding partner in an EMSA may give useful information on the activity or labeling efficiency of the sample. For example, an EMSA of a sample with the appropriate control lanes can yield the fraction of biotin- or DBCO-labeled sample as assayed by a shift when incubated with streptavidin or bovine serum albumin labeled with azide, respectively. Activity assays are generally enzyme-specific, but verifying bulk activity should be a pre-requisite for any single-molecule study.

2.2.3 Data acquisition

Functionalized cantilevers should always be gently moved into and out of the appropriate buffer (*i.e.* never into or out of air or an non-physiological buffer). Other than ensuring the surface and tip are never exposed to an inappropriate buffer, the process for loading surfaces and calibrating cantilevers for force spectroscopy is the same as in Section 2.1.3. For example, cantilevers functionalized with streptavidin are stored in plastic wafers with a small amount of PBS, and before securing the cantilever to the cantilever holder, a small amount of PBS should be placed on the region of the holder where the cantilever will be fixed. In general, cantilevers and surfaces with functionalized biomolecules (as opposed to commercially available, 'off-the-shelf' imaging cantilevers) should never be exposed to pure water or organic solvents, to avoid damaging the biomolecule of interest on the surface or cantilever.

Figure 2.7: Flowchart for AFM SMFS operation. Conventions are as in Figure 2.3.

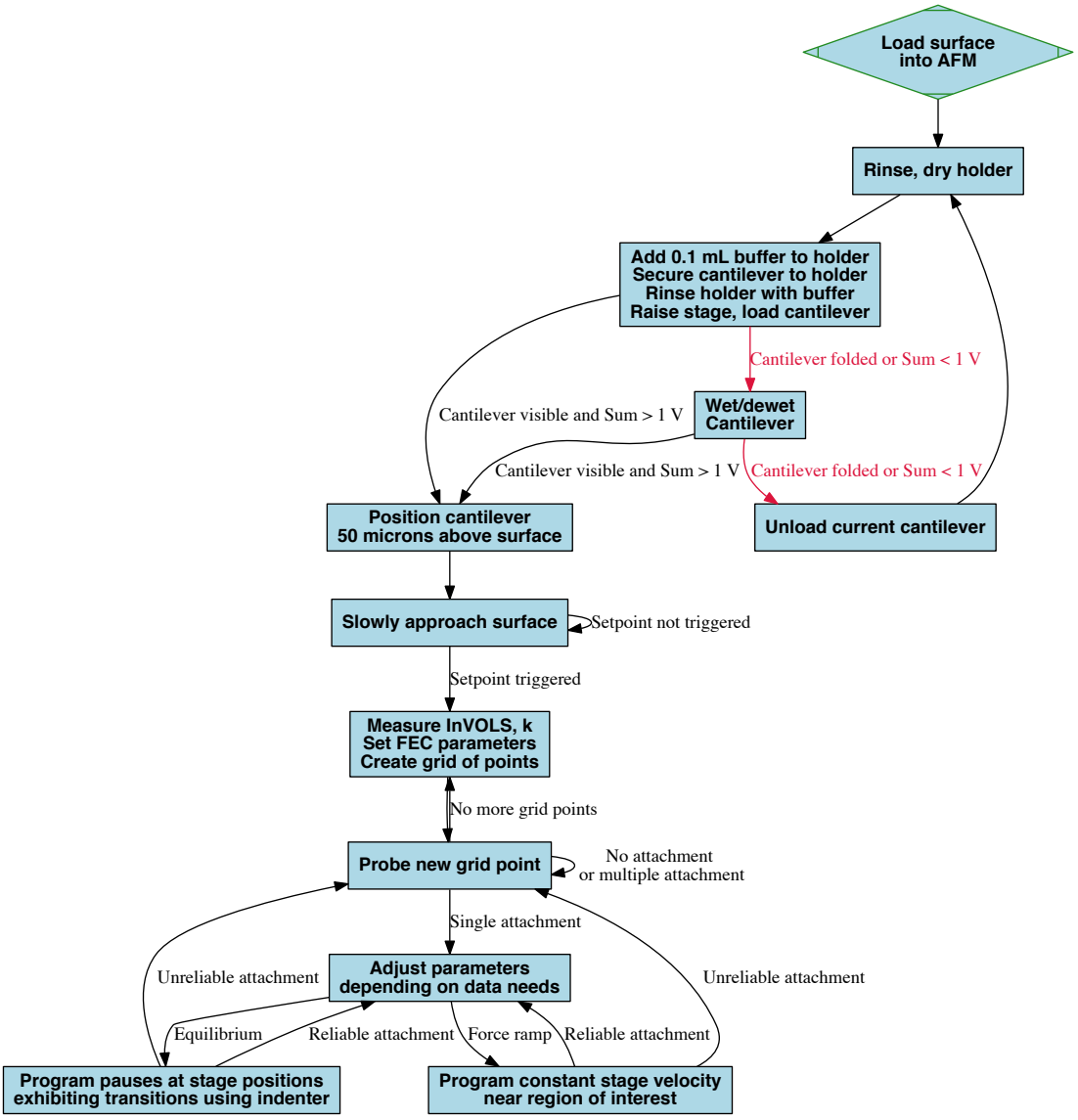

Loading and calibrating a cantilever for a force-spectroscopy experiment is as described for imaging methods in Section 2.1.3, but acquiring SMFS data has different steps (see Figure 2.7). Once at the surface, molecules are found by searching a two-dimensional grid (*e.g.* 30 µm by 30 µm) with between 100 and 1000 points, and a force extension curve is acquired at each point on the grid. Brief pauses or an event detection algorithm facilitate re-visiting a grid point which shows an attachment signature (Figure 2.8 *A*). For BioLever Long cantilevers, drag forces become appreciable (one pN or more) for approach velocities greater than several hundred nanometers per second. Therefore, unless the assay of interest is qualitative (*e.g.* determining surface activity), approach velocities using BioLever Longs should be limited to 500 nm/s or less (or a loading rate of about 3 nN/s or less) to avoid introducing errors on the order of 1 pN or higher.

If a surface-bound molecule has appreciable extension at zero force (*e.g.* a polyprotein), the nudger panel or a sweep of the x and y positions should be employed to find the attachment point of the molecule and move the cantilever to that position [70]. A centered molecule which easily refolds can be repeatedly un- and re-folded for minutes or hours. For the Cypher AFM, a simple way to refold a centered molecule or to take equilibrium data (long dwells at forces near $F_{1/2}$, see [36]) is to program the desired stage positions into the function editor provided by the Asylum software for the Cypher in the indenter panel.

2.2.4 Data analysis and processing

Analysis of force spectroscopy data necessitates several stages of processing, as shown in Figure 2.8. In brief, each curve is filtered, zeroed, and aligned to one or more regions in the force extension curve. These processed curves are used as an input to one or more energy landscape analysis schemes, as described in Chapter 1.

The first step in processing SMFS data necessitates filtering force-extension curves (FECs) in order to reduce data size and processing time. Typically, a second-order Savitsky-Golay filter

[71] is used, since it excels at preserving edges (Figure 2.8 *A*).

After filtering the data, the separation and force of the FEC must be zeroed. Zeroing the data obtained from modified cantilevers is often complicated by an optical interference artifact which corrupts the measured deflection voltage (and hence the measured force) [72]. Fortunately, for relatively drift-free data, the artifact is a simple function of the stage position (Figure 2.8 *B*). Therefore, a smooth spline fit to the approach portion of the force-extension curve (hereafter 'approach') provides an excellent approximation to the optical interference which can then be subtracted from the retract curve (Figure 2.8 *C–D*). After subtracting out any interference artifact (and assuming minimal drift and drag force), the zero force is estimated as the mean force after the final molecular detachment in the retract, and the zero separation is approximated by the value of the separation at the first time when the force is equal to the zero force in the rupture curve.

Even after zeroing, overlaying multiple FECs necessitates alignment, since the curves exhibit high apparent variation due to tip attachment location or heterogeneity in linker length. Aligning to a well-characterized and obligate rupture event typically yields higher-quality results (Figure 2.8 *E*). If a particular transition is of interest, the closest obligate rupture event to that transition should be used to improve the local alignment at that event. Rupture events can be detected using the algorithm discussed in Chapter 4.

Figure 2.8 *(following page)*: Processing AFM force-extension curves (FECs). (A) A plot of the force applied during the approach (red) and retract (blue) portion of the cantilever movement. Raw data is 50 kHz, smoothed data is 400 kHz. (*Inset*) A detailed plot of the low-force interference artifact present in both the approach and retraction. (B) The raw force during the approach curve (light red) is plotted alongside a fit of a spline to the force as a function of the stage position. The spline is only fit above the surface as defined by the trigger force and loading rate. Therefore, for small stage positions the spline is set to its boundary value. (C) The interference artifact and zero force offset are greatly reduced by subtracting the approach spline of panel B from the filtered data from panel A. (Inset) A detailed plot of the low-force behavior demonstrates the subtraction was successful. (D) As panel C, but the data are now plotted at force-versus extension. (E) A detailed plot of the region in panel D where a molecule is present. A freely-jointed chain model (black dotted line) is fit to the region preceding the final rupture.

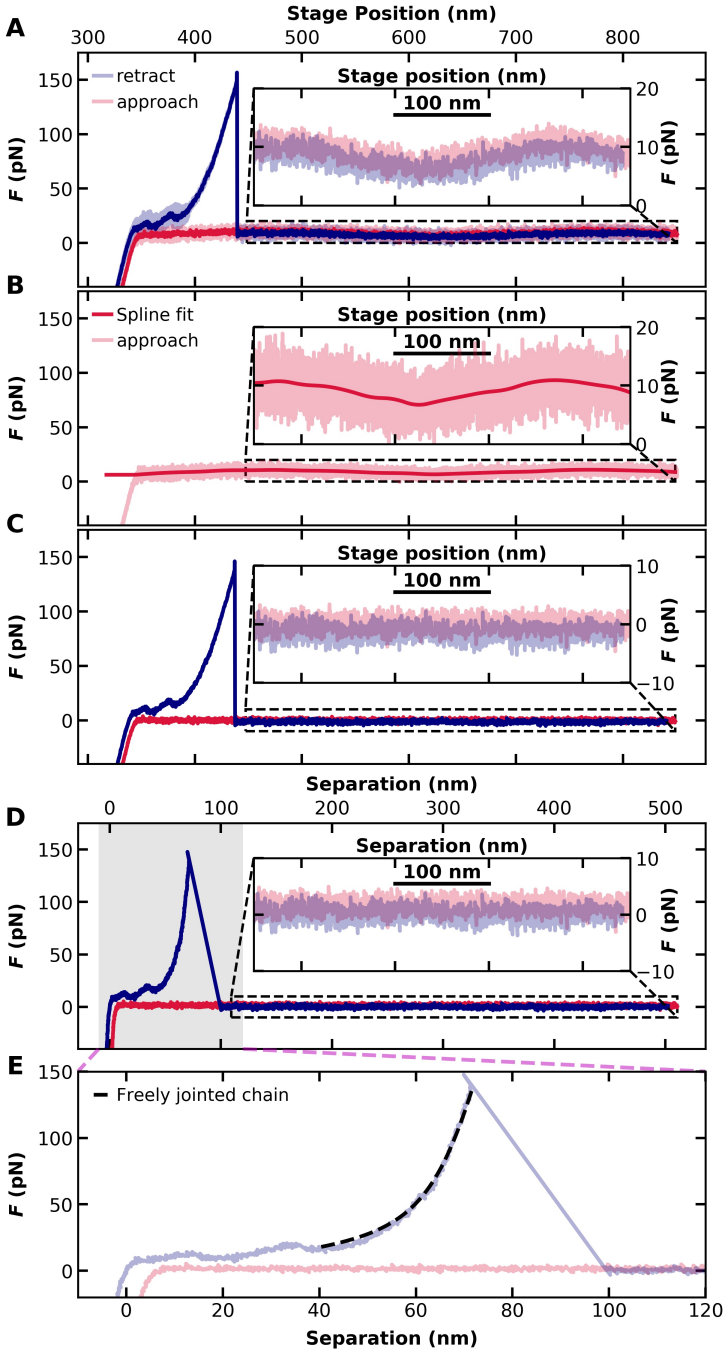
A
Stage Position (nm)
300
400
500
600
700
800
retract
approach
Stage position (nm)
100 nm
F (pN)
150
100
50
0
20
10
0
B
Spline fit
approach
Stage position (nm)
100 nm
F (pN)
C
Stage position (nm)
100 nm
F (pN)
10
0
−10
Separation (nm)
0
100
200
300
400
500
D
Separation (nm)
100 nm
F (pN)
E
Freely jointed chain
F (pN)
0
20
40
60
80
100
120
Separation (nm)

Once the curves are aligned, energy landscapes are reconstructed using non-equilibrium methods like the Inverse Weierstrass Transform (Chapter 5), reconstructed using equilibrium methods such as the Inverse Boltzmann (Section 1.3.1), or energy landscape parameters are calculated via other methods (*e.g.* Equation 1.4).

Chapter 3

Imaging DNA Equilibrated onto Mica in Liquid using Biochemically Relevant Deposition Conditions

Reprinted (adapted) with permission from:

Patrick R. Heenan and Thomas T. Perkins. Imaging DNA Equilibrated onto Mica in Liquid Using Biochemically Relevant Deposition Conditions. **ACS Nano**, 13(4):4220–4229, April 2019.

3.1 Abstract

For over 25 years, imaging of DNA by atomic force microscopy (AFM) has been intensely pursued. Ideally, such images are then used to probe the physical properties of DNA and characterize protein-DNA interactions. The atomic flatness of mica makes it the preferred substrate for high signal-to-noise ratio (SNR) imaging, but the negative charge of mica and DNA hinders deposition. Traditional methods for imaging DNA and protein-DNA complexes in liquid have drawbacks: DNA conformations with an anomalous persistence length (p), low SNR, and/or ionic deposition conditions detrimental to preserving protein-DNA interactions. Here, we developed a process to bind DNA to mica in a buffer containing both $MgCl_2$ and KCl that resulted in high SNR images of equilibrated DNA in liquid. Achieving an equilibrated 2D configuration (*i.e.*, $p = 50$ nm) not

only implied a minimally perturbative binding process, it also improved data quality and quantity because the DNA's configuration was more extended. In comparison to a purely $NiCl_2$-based protocol, we showed that an eight-fold larger fraction (90%) of 680-nm-long DNA molecules could be quantified. High-resolution images of select equilibrated molecules revealed the right-handed structure of DNA with a helical pitch of 3.5 nm. Deposition and imaging of DNA was achieved over a wide range of monovalent and divalent ionic conditions, including a buffer containing 50 mM KCl and 3 mM $MgCl_2$. Finally, we imaged two protein-DNA complexes using this protocol: a restriction enzyme bound to DNA and a small three-nucleosome array. We expect such deposition of protein-DNA complexes at biochemically relevant ionic conditions will facilitate biophysical insights derived from imaging diverse protein-DNA complexes.

3.2 Introduction

Atomic force microscopy (AFM) is widely used to image and thereby characterize the properties of DNA and diverse proteins bound to DNA, including RNA polymerase, restriction enzymes, and nucleosomes [9–24]. Biophysical insights arise by acquiring images with a high signal-to-noise ratio (SNR) and rely upon preserving the native properties of protein–nucleic-acid complexes that can vary strongly with ionic conditions. Tapping-mode imaging in liquid rapidly emerged as the imaging modality of choice as it minimizes the lateral forces that can damage or disrupt fragile biological samples [42]. Unfortunately, a complementary and consensus method for preparing DNA and protein-DNA samples has yet to emerge. For instance, current protocols for imaging DNA in liquid capture DNA in compact, mechanically unequilibrated conformations that hinder analysis and interpretation. An ideal protocol would be rapid, preserve the native properties of the DNA and protein-DNA interaction in liquid, and yield high SNR images. Because of the lack of such an accessible protocol, protein-DNA complexes are still often imaged in air after rinsing them in ultrapure water [74–76], a distinctly non-physiological protocol.

Mica is the preferred substrate for high SNR images due to the simplicity of generating clean, atomically flat substrates. For imaging in liquid, two main strategies have emerged to bind negatively charged DNA to negatively charged mica: mica derivatized with a positively charged silane [11] and Ni^{2+}-treated mica [47, 77], where Ni^{2+} ions have been preferred over Mg^{2+} due to stronger binding of the DNA to mica that facilitates imaging [47]. However, each technique presents important drawbacks. For instance, condensation and/or clumping of DNA can occur on silanized mica in the presence of divalent cations [78]. For Ni^{2+}-treated mica, it has been difficult to deposit and image DNA when monovalent cations are present [79–81]. Yet, numerous ensemble protein-DNA assays contain both $MgCl_2$ and a monovalent salt (*e.g.*, KCl or NaCl). Hence, to minimally perturb protein-DNA complexes, one should deposit them in a buffer containing both $MgCl_2$ and KCl and image in liquid, a difficult regime for AFM studies.

The benefits of silanized mica, including those prepared with silatranes [82], are that they bind DNA under a relatively broad range of buffer conditions [23, 48]. Two drawbacks of silanized mica are (**i**) the time needed to prepare silanized surfaces, and (**ii**) the reduced SNR of the images due to higher surface roughness, a drawback that is partially mitigated when using a more time-intensive sample preparation process [11, 23, 83]. A notable recent application of silanized mica in liquid [23] was successfully deducing the correct persistence of DNA ($p \approx 50$ nm) [84], indicating such images can yield the native backbone stiffness of DNA. To do so, however, the authors needed to apply a 3D worm-like chain (WLC) model to analyze select 2D conformations of DNA. This analysis indicates the DNA was rapidly absorbed and thereby adopted a "kinetically trapped" polymer configuration [17, 23, 48]. If a 2D WLC model is used to analyze the fraction of interpretable conformations, then the derived p is ≈ 25 nm, well below the consensus value of p. As expected for such a low apparent p, kinetically trapped DNA molecules have a more compact configuration and thereby an increased number of multiple strand crossings that hinder analysis (Figure 3.1 *A*, red). In contrast, if the deposition process achieves an "equilibrated" 2D WLC configuration, the conformations are more extended (Figure 3.1 *A*, green) and thus a higher percentage of conformations that contain

Figure 3.1: Configuration of DNA on mica depends on the details of the deposition process. (A) A cartoon illustrating AFM imaging of DNA in two different configurations: an extended, equilibrated one (green) and a compact, kinetically trapped one (red). Yield is defined as the ratio of DNA configurations containing one or zero strand crossings divided by the number of total molecules fully contained in a set of images. The persistence length (p), a measure of polymer backbone stiffness, is determined by the angle between tangent vectors (θ) along the path length s using a 2D WLC model. Credit: S. Burrows/JILA. (B) An AFM image of DNA in liquid when deposited under biophysically relevant ionic conditions (10 mM $MgCl_2$ + 25 mM KCl) and subsequently imaged in 10 mM $NiCl_2$ + 25 mM KCl after pre-treating the mica with 100 mM $NiCl_2$. The yield was high (90%) and analysis of the resulting DNA configurations yielded the correct persistence length ($\approx$ 50 nm). (C) An image of DNA deposited on mica at 10 mM $NiCl_2$ + 25 mM KCl and imaged in the same buffer after gentle rinsing. (D) An image of DNA deposited at 25 mM KCl on mica coated with APTES. All solutions were buffered with 10 mM HEPES (pH 7.5). We note that these conditions were not optimized for the $NiCl_2$ deposition buffer and APTES-derivatized mica protocol used in panels, C–D respectively. All images are 2×2 μm^2 and are colored using the same vertical scaling. Acronym: APTES, (3-Aminopropyl)triethoxysilane.

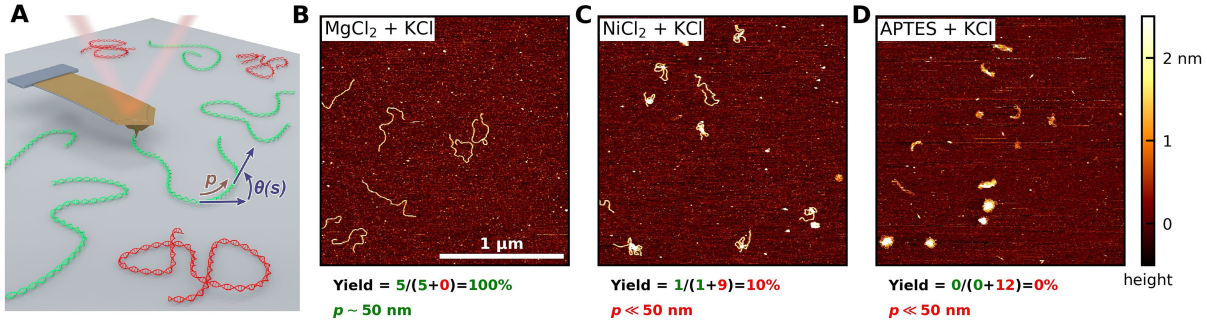

zero or one strand crossings. Quantitatively, a DNA molecule is defined as equilibrated if analysis of its 2D conformation with a 2D WLC model yields the correct of value of p, a definition consistent with prior DNA imaging studies [23, 40]. Such equilibration is distinct from other studies that have observed real-time adsorption and desorption of local segments of DNA from bare mica in liquid [85].

In Ni^{2+}-treated mica, the interstitial K^+ ions at the surface of the mica lattice are ion exchanged with Ni^{2+}, yielding a positively charged surface [79, 86]. The DNA is typically deposited in the presence of ~1–20 mM $NiCl_2$ [47, 86, 87]. The benefits of Ni^{2+}-treated mica are that it yields a higher SNR and requires less preparation time than silanized mica. There are, however, drawbacks: [23] (**i**) the resulting DNA configurations are kinetically trapped, when imaging in liquid [40]; (**ii**) non-physiological ionic conditions ($NiCl_2$ with little or no monovalent cations) are required to achieve sufficiently tightly bound DNA that in turn yields interpretable images [23, 47, 79]; and (**iii**) extensive tuning of buffer conditions [47, 79, 88]. For completeness, as noted above, a popular protocol deposits protein-DNA complexes onto Ni^{2+}-treated mica followed by rinsing with ultrapure water and then imaging in air [41, 87, 89]. While such a protocol has achieved equilibrated DNA when imaging in air, [40] we avoided this class of protocols to preserve native protein-DNA interactions. Moreover, a recent study shows partial conversion of DNA's structure from the traditional B-form to A-form when bound to Ni^{2+} treated mica in air [78]. Summarizing, the consensus in the field is that stable DNA imaging on Ni^{2+}-treated mica requires a narrow window of ionic conditions (*e.g.*, Ni^{2+} cations in the absence of monovalent cations) [23, 79, 83].

Here, our goal was to develop a simple and reproducible protocol for acquiring high SNR images of equilibrated DNA in liquid when deposited at biochemically relevant ionic conditions (*e.g.*, 10 mM $MgCl_2$ + 25 mM KCl). Our protocol was not based on a single modification to an established deposition scheme, but instead on a set of changes including pre-incubating the mica with 100 mM $NiCl_2$, gentle rinsing, and never dewetting the sample. For increased robustness during imaging, we subsequently exchanged an equimolar concentration of $NiCl_2$ for $MgCl_2$. Analysis of the resulting

DNA configurations yielded the correct persistence length (≈ 50 nm) when using a 2D WLC model and did so over a wide variety of monovalent salt concentrations. These equilibrated configurations were more extended (Figure 3.1 *B*) than when 10 mM $NiCl_2$ replaced the 10 mM $MgCl_2$ in the deposition buffer (Figure 3.1 *C*) or the DNA was deposited onto silanized mica (Figure 3.1 *D*). Importantly, our protocol used only standard, commercially available reagents, took ~5 min, and worked over a range of DNA substrate lengths (300–2,000 bp) and in a standard commercial AFM. Unexpectedly, divalent cations in the imaging buffer were not required; we successfully imaged DNA on mica pre-incubated with 100 mM $NiCl_2$ when using an imaging buffer containing only monovalent ions albeit at some loss in data throughput and a reduction in p (35 nm). Biophysical applicability was demonstrated by imaging two protein-DNA complexes, a restriction enzyme bound to DNA and a small nucleosome array.

3.3 Results and Discussion

We first present the final protocol, then discuss the process of achieving this protocol and how it generalizes to an unexpectedly broad range of ionic conditions for deposition and imaging, and finish by imaging a pair of protein-DNA complexes. In developing our protocol, we used two primary metrics: yield and persistence length. Yield was defined as the ratio of DNA configurations containing zero or one strand crossing divided by the number of total molecules fully contained within a set of images; such configurations facilitate analysis and the effect of proteins on the DNA conformation. Persistence length was determined from the 2D WLC model by analyzing the average tangent angle as a function of arc length along the DNA for molecules displaying zero or one crossing (Figure 3.7) [40, 90]. Achieving a persistence length of ≈ 50 nm—in agreement with ensemble [84] and single-molecule force-spectroscopy [23, 91, 92] studies—would therefore reflect DNA bound to the mica in an equilibrated state (see Methods).

3.3.1 Rapid and biochemically relevant DNA deposition protocol

Our final protocol consisted of three main steps (Figure 3.2). In the first step, we placed a 20-µl drop of unbuffered 100 mM $NiCl_2$ onto freshly cleaved mica for 1 min followed by rinsing with ultrapure water and drying by touching the mica surface with filter paper. Importantly, this step— before depositing any DNA or protein-DNA complexes—was the only time the surface was dried and indeed the method of drying affected the final outcome (Figure 3.8). In the second step, we deposited a 20-µl drop of dilute DNA in Deposition Buffer [10 mM $MgCl_2$, 25 mM KCl, 10 mM HEPES (pH7.5)] onto the mica for 2 s before gently rinsing with 9 ml of Deposition Buffer (see Methods for details). Successful imaging of the DNA after such extensive rinsing demonstrated that DNA stayed attached to the Ni^{2+}-treated mica in the presence of 10 mM $MgCl_2$. Finally, in the third step, we rinsed the mica with Imaging Buffer [10 mM $NiCl_2$, 25 mM KCl, 10 mM HEPES (pH7.5)] where the $NiCl_2$-containing buffer trapped the equilibrated state of the DNA bound to the mica by increasing the DNA-mica interaction strength. This entire process starting from cleaving the mica to loading the sample into the AFM typically took ~5 min.

3.3.2 Improved protocol relies upon a series of refinements

Our final protocol evolved *via* a series of modifications that collectively were critical to achieving high yield while minimizing the influence of the substrate on the nanomechanics of the DNA, as evidenced by the deposited DNA adopting extended conformations with the correct persistence length. For conciseness, a subset of the deposition conditions tested are shown in Figure 3.3 to illustrate sequential improvement. Figure 3.3 *A* shows representative images of the DNA configurations at select steps along this evolution accompanied by a summary of the deposition conditions at each step. The change in the conditions between the steps is highlighted in blue. Figure 3.3 *B–C* reports the yield and average persistence length of analyzed molecules. We note that these data (images, yield, and persistence length) were representative of our results at each step, not

Figure 3.2: Rapid three-step protocol for preparing DNA for imaging on mica in liquid. This protocol consisted of three main steps. First, freshly cleaved mica was incubated with $NiCl_2$ at a ~10-fold higher concentration than traditionally used, rinsed with ultrapure water, and then gently dried. Second, dilute DNA was deposited onto the Ni^{2+}-treated mica at biochemically relevant ionic conditions and then the mica was extensively rinsed with deposition buffer. In the final step, the equilibrated configuration of the DNA was fixed for more robust imaging by increasing the interaction between the DNA and the mica by using an imaging buffer that contained 10 mM $NiCl_2$. As discussed in the text, imaging in $NiCl_2$ was not required.

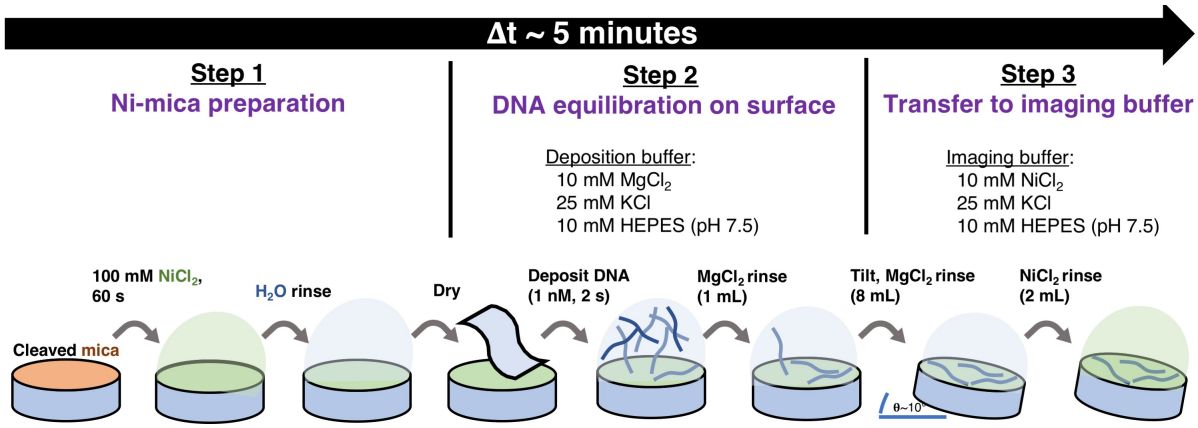

necessarily the best achieved. We did not optimize intermediate steps along the process but rather looked for a set of conditions that led to a simple and robust deposition protocol at biochemically relevant conditions. In total, over 2,500 molecules were analyzed in this work when including the Supporting Information.

The starting point for our modifications featured ionic conditions typical of Ni^{2+}-treated mica protocol (10 mM $NiCl_2$ in the pre-treatment, deposition, and imaging buffers with a 2 mL rinse). As expected, these conditions resulted in a high proportion of kinetically trapped molecules that led to a low yield and persistence length (Figure 3.3 *A*, Step 1). By increasing the concentration of $NiCl_2$ used to pre-treat the mica, we marginally increased the yield (Figure 3.3 *A*, Step 2). Perhaps more importantly, we observed that the uniformity of the DNA on the surface dramatically increased (Figure 3.9), presumably because the higher $NiCl_2$ concentration overcame the previously described patchiness of Ni^{2+} on mica when incubating at 15 mM $NiCl_2$ [86]. [Note, uniformly charged Ni^{2+}-treated mica may be broadly useful in a variety of AFM applications. As a proof of principle, we imaged the 2D lattice of bacteriorhodopsin (Figure 3.10)].

Next, we replaced the $NiCl_2$ in the deposition and imaging buffers with $MgCl_2$, which led to a fraction of the DNA molecules exhibiting the correct persistence length (Figure 3.3 *A*, Step 3). However, the fraction of molecules exhibiting that equilibrated confirmation was low due, in part, to the weak DNA-mica interaction. In other words, these initial imaging experiments with only $MgCl_2$ in solution featured well-equilibrated DNA, but the DNA was too weakly bound for reliable tapping-mode imaging. We note that this intermediate finding is consistent with previous studies in air [40] and liquid [47], though our final protocol does allow us to deposit and image in buffer containing $MgCl_2$ and KCl but, notably, no $NiCl_2$. In other words, $NiCl_2$ in the final buffer is not necessary but improves data quality by binding the DNA more strongly to the surface (Figure 3.11); successful imaging in $NiCl_2$ is therefore less stringent in its requirement of gentle imaging conditions (*e.g.*, low-amplitude tapping, see Methods for details).

Figure 3.3: Improved DNA deposition required a sequence of refinements. (A) A set of tapping-mode images of DNA in liquid deposited under different deposition protocols as summarized in each box. The change between each deposition process is highlighted with blue text, and protocols associated with images are denoted with magenta boxes. (B–C) The percentage yield of interpretable DNA molecules and their corresponding persistence length (p) is depicted below each protocol. These values were computed from ~90 DNA molecules per condition with necessarily more images acquired at deposition protocols with a poor yield. Error bars represent the standard deviation for the yield and the fitting error for the persistence length. Persistence length was deduced using a 2D worm-like chain model. Solid symbols are associated with the images shown in panel A.

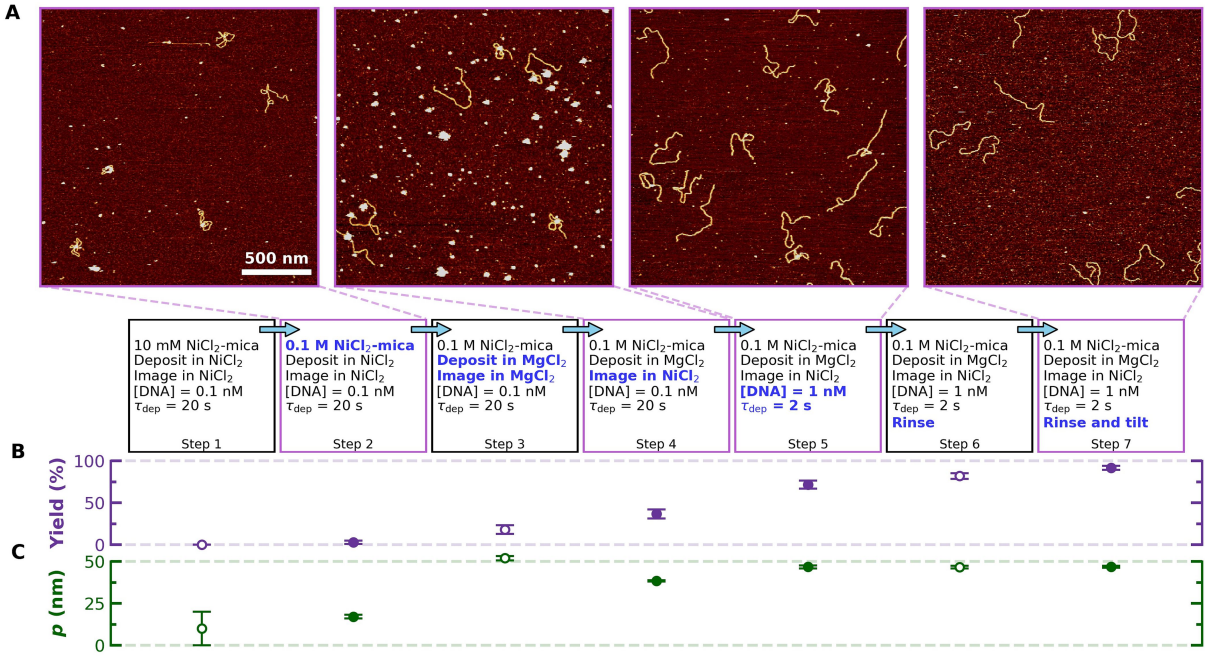

We next combined the merits of depositing in $MgCl_2$ (to facilitate DNA equilibration) with imaging in $NiCl_2$ (for more robust imaging)(Figure 3.3 *A*, Step 4). A useful analogy may be found in film photography, where an image is first developed before it is fixed or stabilized. In this analogy, the surface-bound DNA is the image, $MgCl_2$-based equilibration is the development process, and the $NiCl_2$-based imaging buffer is the fixing procedure. We continued to refine our deposition process to enhance the yield of molecules showing only one or zero strand crossings by reducing the deposition time and increasing the DNA deposition concentration (Figure 3.3 *A*, Step 5). Although the underlying mechanism for this improvement is unclear, it was experimentally reproducible across multiple samples on multiple days. Finally, we found that extensive (9 mL), but gentle, rinsing improved the equilibration of the DNA onto the mica (Figure 3.3 *A*, Steps 6–7; see also Figure 3.2, Step 3). Introducing a small tilt during the extensive rinsing further improved yield, presumably because it helped avoid accidental dewetting (Figure 3.12) and the resulting high forces generated by a receding meniscus on a surface-bound DNA [*i.e.*, molecular combing ($F > 65$ pN)] [93, 94].

3.3.3 High yield of equilibrated DNA on mica in liquid

By analyzing images acquired with our final protocol, we quantified the yield and the persistence length. The yield was 90% when imaging 680-nm-long DNA molecules [$N = 142$], an 8-fold improvement over depositing the DNA under identical DNA concentration and total ionic strength but substituting 10 mM $NiCl_2$ for the 10 mM $MgCl_2$ and rinsing with 2 mL of buffer ($N = 116$). Analysis of the DNA images yielded an average persistence length of 46.8 ± 0.6 nm (mean $\pm$ fitting error; $N = 126$)]. (Figure 3.3 *C*; Figure 3.7), demonstrating the analyzed molecules had adopted a 2D equilibrated configuration on the mica. Indeed, of those molecules that contributed to the 90% yield, about 20% contained a looped configuration, consistent with expectations from a simple simulation that did not account for excluded volume effects (Figure 3.13). As a cross check, we deduced p from the distribution of end-to-end distances as a function of arc length, yielding $p = 45$

± 4 nm [mean ± fitting error (Figure 3.14)] in quantitative agreement with p derived from the tangent vectors analysis. Finally, we note that the values for persistence and contour lengths obtained from human-annotation (see Supporting Information) were consistent with the values obtain using an automated analysis routine (Figure 3.15) [66].

3.3.4 High-precision measurements of DNA conformation

To quantify the SNR of the resulting images, we first measured the height of the DNA bound to mica using a metric based on the maximum height of each pixel along the spline defined along the full contour length of each molecule, rather than a single line or set of line scans per molecule (Figure 3.16 *A*–*B*). The results yielded 2.0 ± 0.3 nm [mean ± Std. Dev.; $N_{\text{molecules}} = 100$ (Figure 3.16 *C*)] in quantitative agreement with the DNA's width (2.0 nm) [95]. Such agreement reflects the gentle imaging conditions, akin to earlier results that measured a height of 1.9 ± 0.2 nm when using peak-force tapping set to 40 pN [81], with the advantage that the tapping-mode imaging used here leads to higher image acquisition rates. To quantify the noise, we measured the average surface roughness of bare mica, Ni^{2+}-treated mica, and APTES-coated mica (Figure 3.17), yielding 1.14 ± 0.07 Å, 1.95 ± 0.06 Å and 4.3 ± 0.2 Å (mean ± Std. Dev.), respectively. Hence, we have measured the correct height for DNA and at a SNR of 10, a high SNR compared to traditional AFM imaging of DNA [81].

To illustrate the quality of the resulting images, we show a gallery of representative DNA configurations (Figure 3.4 *A*). The average persistence length for the six molecules shown is 50.8 ± 0.9 nm (mean ± SEM), similar to the persistence length determined for all molecules analyzed using the deposition protocol depicted in Figure 3.2. High-resolution scans of select segments of individual molecules revealed the right-handed helical structure of DNA (Figure 3.4 *B*). The helical pitch of DNA has been previously resolved in liquid [81, 96] with clearer images recently achieved when using frequency-modulated AFM [97, 98]. Here, using tapping-mode imaging, we quantified

Figure 3.4: Images of individual DNA molecules highlight the resulting high signal-to-noise ratio. (A) A set of representative raw tapping-mode images of DNA in liquid selected from a larger scan area (2×2 μm^2) with traditional flattening. (B) An exemplary image of the double helix of DNA acquired using a tip featuring a sharper tip radius ($r_{nom} \approx 2$ nm) and smaller pixel size (0.5 Å) than those used in the remainder of the paper (see Methods). This image was fit with a third order, two-dimensional spline to subtract the background, then smoothed with a Gaussian with a width of two pixels (1 Å).

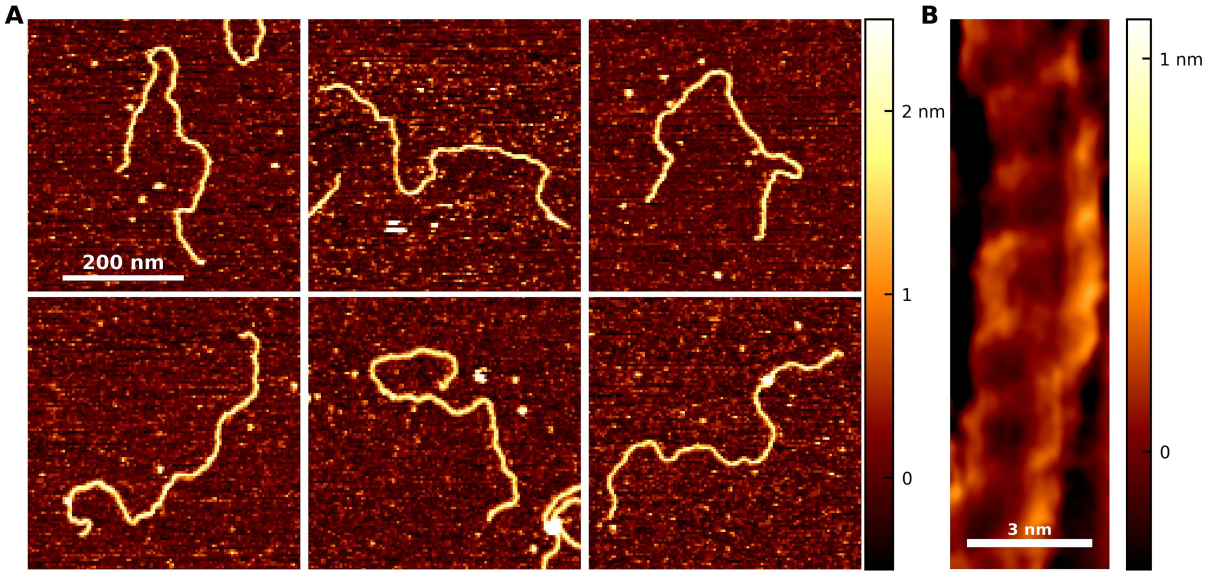

the helical pitch of equilibrated DNA to be 3.51 ± 0.04 nm (mean ± SEM) (Figure 3.18) based on 15 images from 4 different molecules and 3 different cantilevers. Our result agrees with ensemble enzyme digestion studies that report a helical pitch of 3.6 nm [99]. This high-resolution study was facilitated by using a cantilever featuring a sharper tip radius [$r_{\mathrm{nom}} \approx 2$ nm (Bruker SNL-10A)] than used in the rest of the paper [$r_{\mathrm{nom}} \approx 8$ nm (Olympus BioLever Mini)] and by having the fast-scan axis parallel to the DNA axis. Approximately, one out of every three of these sharper cantilevers resolved the helical pitch of select DNA segments.

Quantification of the DNA's contour length agreed within 1% of the expected length (Figure 3.19), when using the standard rise per base pair for B-form DNA (0.34 nm/bp). [Note, as a counter example, DNA imaged in air on mica had a 20% reduction in contour length after depositing in $MgCl_2$ consistent with the DNA adopting a partial A-form structure, as confirmed by spectroscopic studies.] [78] Successful application of our protocol was not restricted to relatively long DNA, but also worked well for 300-bp long DNA (Figure 3.20). Summarizing, we measured the correct physical properties of DNA (persistence length, rise per base pair, width, and helical pitch) when imaging in liquid.

3.3.5 Depositing and imaging DNA under biochemically relevant ionic conditions

Our deposition protocol performed well across a wide range of monovalent and divalent combinations. For example, as the concentration of KCl in the deposition buffer was varied from 0 to 75 mM at fixed $MgCl_2$ concentration (10 mM), the yield and the persistence length remained essentially unchanged (Figure 3.5 *A*–*B*), indicating the DNA continued to adopt an equilibrated conformation. A global fit to the dependence of p as a function of monovalent ionic strength [100] yielded 49.6 ± 0.4 nm (mean ± fitting error) (Figure 3.21), again consistent with an equilibrated 2D conformation. Equally important, the quality of the resulting images remained high (Figure 3.5 *C*). At the highest KCl concentration tested (225 mM), the yield remained high but the persistence

Figure 3.5: Equilibrated DNA deposited across a broad range of monovalent ionic conditions. (A–B) The percentage yield of interpretable DNA molecules and their corresponding persistence length (p) plotted as a function of monovalent ionic concentration at fixed $MgCl_2$ (10 mM). Closed symbols are associated with images shown in panel C. For comparison, yield and persistence length acquired under typical published conditions [10 mM $NiCl_2$ or APTES-functionalized mica] are shown. The $NiCl_2$ + KCl and APTES + KCl data points were determined from DNA deposited as in Figure 3.1 *C* and Figure 3.1 *D*, respectively. Error bars represent the standard deviation. (C) Sets of three representative images plotted vertically acquired at 0, 2.8, 8.3, 25 and 75 mM KCl. Nanoscale precipitates became prevalent ≥75 mM KCl but the configuration of individual DNA molecules could still be traced and hence persistence length determined.

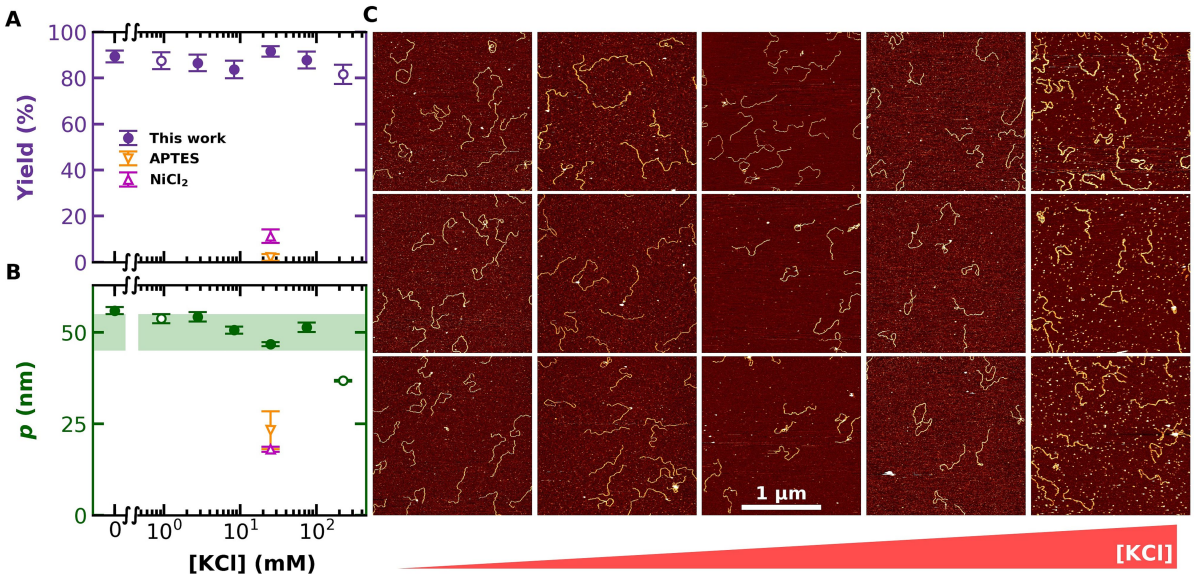

length decreased to ~35 nm (Figure 3.5 *A*–*B*). At the higher KCl concentrations ($\geq$ 75 mM), there were also some small surface artifacts (several nm wide by 1 nm tall), presumably salt crystals.

Unexpectedly, we could deposit and image in 3 mM $MgCl_2$ and 50 mM KCl (Figure 3.11), ionic conditions typical of many protein-DNA assays. As expected the persistence length remained approximately unchanged (~ 55 nm), but there was a reduction in yield to ~60% and successful imaging required gentle imaging conditions. We could also reduce or eliminate the divalent salt in the deposition and imaging buffers ($MgCl_2$ and $NiCl_2$, respectively) after pre-treating the mica with 100 mM $NiCl_2$. In the absence of any divalent cations, the yield was reduced from ~90% to ~50% and p decreased to ~35 nm, but the configuration of individual molecules remained well resolved (Figure 3.22). Overall, the robustness of our protocol to variations in KCl and divalent ion concentrations show that our methodology produced high-quality images of DNA deposited on Ni^{2+}-treated mica over a wide range of monovalent and divalent salt concentrations, a regime that was previously thought inaccessible. That said, it remains critical to deposit with $MgCl_2$ [or $CaCl_2$ (see below)] in lieu of $NiCl_2$ to equilibrate the DNA on the mica. Replacing $MgCl_2$ with $NiCl_2$ in our deposition buffer while keeping the rest of the final protocol the same led to kinetically trapped molecular configurations ($p \approx 25$ nm) (Figure 3.23), recapitulating earlier results [40].

3.3.6 Imaging protein-DNA complexes in liquid

To demonstrate the broader applicability of our protocol, we next imaged two protein-DNA complexes: a restriction enzyme bound to DNA and a three-nucleosome array (Figure 3.6). Restriction enzymes, which cleave DNA at specific sequences, have been repeatedly studied by AFM [16, 18, 19, 101, 102]. BspMI is a type IIs restriction enzyme that binds to the sequence 5'-ACCTGC-3' and cleaves down stream of this recognition site. Cleavage occurs efficiently when BspMI binds to and bridges two recognition sites[103]. Like many restriction enzymes, BspMI can bind its recognition site without cleaving if Mg^{2+} is replaced by Ca^{2+}. Hence, to image BspMI

Figure 3.6: High signal-to-noise ratio images of protein-nucleic acid complexes deposited at biochemically relevant conditions. (A–B) Images of the type IIs restriction enzyme BspMI bound to a 650-nm-long DNA *via* the single recognition site located at the center of the DNA. $CaCl_2$ was substituted for $MgCl_2$ in the deposition buffer to suppress cleavage. (C) An image showing two separate DNA molecules bridged *via* a BspMI complex bound to two recognition sites. Such bridging is a key step to efficient cleavage by BspMI [101]. (D) An image of three nucleosomes on a 621-bp-long DNA substrate containing three high affinity binding sites for nucleosomes (*i.e.*, the 601 Widom sequence) deposited using our standard protocol containing $MgCl_2$ (Figure 3.2).

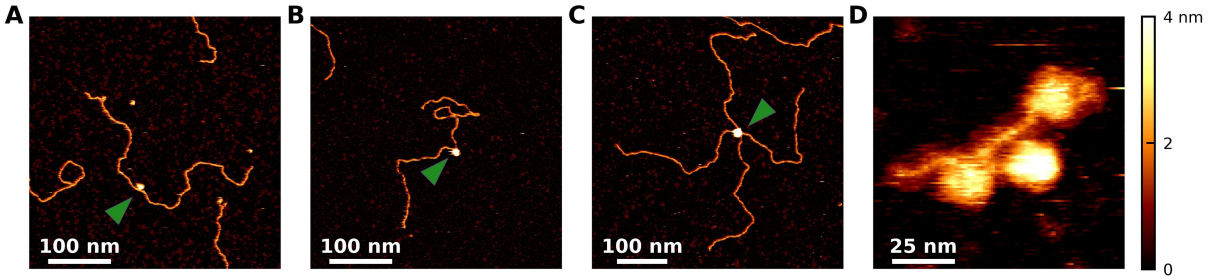

bound to uncleaved DNA, we developed a 650-nm-long DNA with a single recognition site at its center and replaced $MgCl_2$ with $CaCl_2$ in our deposition buffer (see Methods for details). With these modifications, we acquired high-SNR images of BspMI bound to DNA in liquid (Figure 3.6 *A–B*). As expected, BspMI bound to the center of individual DNA molecules. In addition, we observed DNA dimers formed by BspMI complexes bridging two separate DNA molecules (Figure 3.6 *C*). This behavior is well established in ensemble studies [103]. More recently, AFM studies in air showed BspMI complexes bridging two separate binding sites after rinsing with ultrapure water [74]. Here, we can now visualize DNA bridging by BspMI imaged in liquid and do so with significantly higher SNR than the prior results in air. In addition, this result validates Ca^{2+} as an alternative divalent cation, as it also produced equilibrated DNA ($p \approx 52$ nm). Finally, building upon earlier AFM studies characterizing un-crosslinked nucleosomes in liquid [104, 105], we imaged nucleosomes bound to three high-affinity binding sites embedded in a 621-bp long DNA (Figure 3.6 *D*) [106]. Hence, the robustness and flexibility of our method permitted high-SNR imaging in liquid of a variety protein-nucleic acid complexes.

3.4 Conclusions

In summary, we deposited and imaged DNA in an equilibrated conformation on mica in liquid, implying a gentle deposition process. Equilibrated conformations were more extended and therefore easier to analyze when determining the DNA's configuration and the effect of proteins on that configuration. Importantly, we used a deposition buffer that contained both $MgCl_2$ and KCl, ionic conditions conducive to preserving native protein-DNA interactions. This success was not based on a single modification to an established protocol, but a set of changes including pre-incubating the mica with 100 mM $NiCl_2$, drying with a filter paper, gentle rinsing, and never dewetting the sample. Imaging using such Ni^{2+}-treated mica yielded images with high SNR. To demonstrate the utility of this protocol, we imaged two protein-DNA complexes: a restriction enzyme bound to DNA and a nucleosome array. Looking forward, we speculate that the unexpectedly wide range of

ionic conditions that yielded such images enables tuning the binding strength of the DNA to the surface, akin to earlier studies [88], but in buffers containing both $MgCl_2$ and KCl. Such tuning, in turn, should facilitate studying the dynamics of protein-DNA complexes by AFM, in general, and by high-speed AFM, in particular, [88, 107] at higher SNR coupled with conditions that preserve native protein-DNA interactions. Finally, our success in imaging protein-DNA complexes should immediately translate to the AFM studies of DNA origami and their applications.

3.5 Methods

3.5.1 DNA samples

We purchased 300 and 2,000 base pairs (bp) DNA constructs that were HPLC purified (Fisher SM1621, SM1701). These DNAs were diluted to 50 ng/µL in TE Buffer [10 mM Tris-HCl (pH 8.0), 1 mM EDTA] and 20-µL aliquots were flash frozen and stored at -20 °C. Individual aliquots were thawed to room temperature and then stored at 4 °C for at most one week. For the BspMI assay, we developed a DNA construct from λ bacteriophage (NEB N3011S) by amplifying from position 9,887 to 11,785. This PCR-amplified 1,899 bp (≈ 650 nm) segment was chosen to position the BspMI recognition sequence (5'-ACCTGC-3') at the center of the resulting PCR product. After the DNA was purified *via* an agarose gel, the agarose was removed (Bio-Rad 7326165), the DNA was concentrated (Millipore UFC501024), and purified a final time (Qiaquick 28106) before elution into TE Buffer. The final DNA was diluted down to 180 nM in TE Buffer, aliquoted, and flash frozen.

3.5.2 DNA deposition protocol

We deposited the DNA as outlined in the text and illustrated in Figure 3.2. More specifically, we diluted the aliquoted DNA to 20 nM (for 2,000-bp DNA) or 80 nM (for 300-bp DNA) in our Base

Buffer [10 mM HEPES (pH 7.5), 25 mM KCl] using KOH to adjust the pH. A higher concentration of smaller DNA was used to increase the number of molecules per image. We then cleaved 10-mm diameter mica (Ted Pella, 50) affixed to a metal puck (Ted Pella, 16218). We next placed a 20-µl drop of unbuffered 100 mM $NiCl_2$ (Sigma 654507) onto the freshly cleaved mica for 1 min followed by rinsing with 50 mL of ultra-pure water (18.2 MΩ, Barnstead GenPure Pro). The mica was then quickly dried by touching filter paper (Whatman 1002-042) to the center of the water droplet on the mica, and completely drying the surface. This step was the only time where the surface was allowed to partially or completely dewet. Immediately after drying, we deposited 20 µL of DNA in Deposition Buffer [10 mM HEPES (pH 7.5), 10 mM $MgCl_2$ + 25 mM KCl] where the concentration of the DNA was 1 nM for the 2,000-bp construct or 4 nM for the 300-bp construct. After 2 s, we gently rinsed the surface with ~1 mL of Deposition Buffer, tilted the surface to about 10°, and then gently rinsed with an additional 8 mL of Deposition Buffer. Care was taken during rinsing to avoid exposing any part of the surface to air or forces from a water droplet overcoming meniscus forces and/or rapidly flowing off of the side of the mica, which could perturb the sample and may cause salt to precipitate out of solution onto the surface. Finally, the surface was gently rinsed with 2 mL of Imaging Buffer [10 mM HEPES (pH 7.5), 10 mM $NiCl_2$ + 25 mM KCl]. Note, during deposition and rinsing, solutions were kept at room temperature (19 °C for the room containing our AFM). At all other times, the reagents were kept at 4 °C. Buffers were re-made each day from concentrated, 0.2-µm filtered stocks. For completeness, we note that we unexpectedly found that $NiCl_2$ solution made from seven-month-old $NiCl_2$ powder yielded poor results in comparison to a freshly purchased stock of $NiCl_2$ or a seven-month-old 1 M stock solution $NiCl_2$ (Figure 3.24).

The '$NiCl_2$ + KCl' protocol shown in Figure 3.1 and Figure 3.3 was prepared as above, except using a 10 mM $NiCl_2$ pre-treatment, and Imaging Buffer during deposition, rinsing, and imaging. Moreover, we only rinsed with 2 mL of Imaging Buffer, and omitted additional tilting and rinsing to better match more traditional $NiCl_2$ deposition conditions. The sample was dried using a filter paper as described above. To study DNA deposition on APTES-modified mica, we used

our standard protocol, except substituting 0.1% APTES dissolved in water for 100 mM $NiCl_2$, and rinsing and imaging in the absence of divalent salt (*i.e.*, Base Buffer), as is typical with APTES-coated mica [83]. Before DNA deposition, the APTES-treated sample was also dried using a filter paper.

3.5.3 Depositing protein-DNA complexes

Importantly, we did not need to alter our deposition protocol for imaging protein-DNA complexes. The tri-nucleosome array was a gift of Anne Gooding and Tom Cech and based on published work from the Cech lab [106]. For depositing the tri-nucleosomes, we diluted them in Deposition Buffer to the same concentration used with the 300-bp DNA. The rest of the process, including deposition time, remained unchanged.

For the restriction-enzyme assay, we incubated 650-nm-long DNA at 20 nM with 40-fold diluted BspMI (New England BioLabs, R0502s, 50 units/mL incubation concentration) and 10 mM HEPES (pH 7.5), 10 mM $CaCl_2$ + 25 mM KCl as the buffer. After letting the enzyme and DNA incubate for 30 min at 30 °C, the deposition proceeded as described above, except with the $MgCl_2$ replaced by $CaCl_2$**.** Replacement of $MgCl_2$ with $CaCl_2$ allowed for site-specific binding but without cleavage (Figure 3.6 *A*–C). When the same process was repeated in our standard Deposition Buffer, the DNA was cleaved due to the expected activity of BSP-MI in the presence of $MgCl_2$ (data not shown).

3.5.4 AFM imaging

We imaged all samples on a commercial AFM (Cypher ES, Asylum Research) featuring a temperature-controlled, closed-fluidic sample holder. Sample temperature was held at 19 °C. All images, except high-resolution images of the double helix, were obtained using an Olympus BioLever

Mini ($r_{\mathrm{nom}} = 8$ nm; $k_{\mathrm{typ}} = 90$ pN/nm) with a 25-kHz resonance in liquid. For imaging the double helix, we used a Bruker SNL-10A ($r_{\mathrm{nom}} \approx 2$ nm; $k_{\mathrm{typ}} = 350$ pN/nm), which had a 16-kHz resonance in liquid.

Prior to imaging, we let the sample and cantilever settle for at least 30 min. All images were obtained in tapping mode with a typical set point amplitude of about 2 nm and a free amplitude of 150% of the set point. We chose the drive frequency as the closest peak of the drive transfer function to the thermal resonance when measured ~ 1 μm above the surface. All data presented in this paper used 2×2 μm^2 images with 512 pixels acquired at a 2-Hz scanning rate, except those of the double helix (Figure 3.4 *B* and Figure 3.18), images with protein-DNA complexes (Figure 3.6), and bacteriorhodopsin (Figure 3.10). The images of the double helix were taken with the same parameters, except the following changes: set point amplitude (~ 0.5–1 nm), free amplitude (~ 0.7–1.5 nm), and image size (20–100 nm). The images of bacteriorhodopsin or protein bound to DNA used similar imaging parameters to the double helix, except the image size varied as follows: ~ 25 nm for bacteriorhodopsin, ~ 200 nm for the trinucleosomes, and ~ 600 nm for BspMI. The double helix images were taken with the fast-scan axis along the axis of the DNA to improve resolution by reducing low-frequency noise between line scans and tip-convolution artifacts.

3.5.5 Surface roughness of bare and treated mica

To quantify the difference in surface roughness between Ni^{2+}-treated mica and our APTES-coated mica, we created mica surfaces without adsorbed DNA and thereby measured the noise floor of our AFM measurement system in liquid as a function of surface treatment. The $NiCl_2$ and APTES test surfaces were prepared as described above, except omitting DNA in any of the buffers. As a control, we used unmodified mica that was rinsed and imaged in Base Buffer. All measurements that quantified the noise were obtained in the appropriate imaging buffers with the same individual cantilever on the same day. Other imaging parameters were consistent with the

DNA experiments as discussed above, and we analyzed 3 images at each condition. As shown in Figure 3.17, bare mica showed the lowest surface roughness as measured by the standard deviation of the height [0.74 ± 0.03 Å (mean ± Std. Dev.)], with a measurable increase due to Ni^{2+}-treatment (1.18 ± 0.03 Å). As expected, the noise floor on APTES-coated mica was significantly higher (2.5 ± 0.1 Å).

3.5.6 Imaging bacteriorhodopsin

To see if Ni^{2+}-treated mica might be useful in other AFM applications, we imaged bacteriorhodopsin embedded in its native lipid bilayer, the prototypical protein for AFM studies of membrane proteins [108]. In initial experiments using standard bacteriorhodopsin imaging conditions (10 mM TrisHCl (pH 7.8), 150 mM KCl) [109], we resolved voids in the trimer lattice. Note, this proof-of-principle experiment was not optimized for image quality (Figure 3.10). Rather, we just wanted to demonstrate that the benefits of Ni^{2+}-treated mica were not limited to protein-DNA complexes.

3.5.7 Image analysis

We analyzed all AFM images of DNA using a semi-automated algorithm to determine the yield and persistence length. First, all DNA molecules fully contained within a single 2×2 μm^2 image were manually classified as either an interpretable individual DNA configuration that contained zero or one strand crossings (Figure 3.1, green), uninterpretable configurations that contained 2 or more strand crossings (Figure 3.1, red) or multiple overlapping individual DNA molecules. We classified molecules with two or more loops as kinetically trapped due to their low apparent persistence length. Surface artifacts (*e.g.* a salt crystal) that could be reliably identified as not a DNA molecule were ignored. The yield, Y, was defined as:

$$Y = 100 * N_{\text{interpretable}}/(N_{\text{interpretable}} + N_{\text{uninterpretable}} + N_{\text{overlapping}}) \text{ Eqn. 1}$$

where a yield of 0 indicates completely uninterpretable data, and a yield of 100 indicates completely interpretable data.

We quantified the angle θ between two tangent vectors separated by arc length s to measure the persistence length (p) of a molecule *via* AFM imaging (Figure 3.1 *A*). The tangent vector was determined by fitting a third-order, least-squared polynomial spline through user-defined points spaced about every 10 nm along interpretable DNA molecules, excluding the looped sections of interpretable molecules that contained a loop (20%). The persistence length at a given condition was then obtained by a least-squares fit of the following equation for all interpretable molecules at that condition:

$$\ln(\langle\cos(\theta(s))\rangle) = -s/2p \text{ Eqn. 2.}$$

The helical pitch was quantified by marking the position where the periodic structure of one DNA strand repeated. The position where a repeat crossed the axis of the DNA was manually bounded by two points, and the region in between these human-annotated points was fit with a parabola. The maximum of the parabola was considered the location of the repeat, where the fit was localized to a line of length 10 Å or less along the DNA axis. In other words, the human-annotated helical pitch location was refined by determining the local maximum in the DNA height from a parabolic fit. From two adjacent helical pitch locations on the same DNA strand, major pitch values were recorded as the total change in contour length. Both strands were measured separately in our estimation of the helical pitch.

3.5.8 Automated annotation

To verify that the human-annotated DNA contours were unbiased, we adapted a previously published method [66] for automated contour tracing. Briefly, the start and end of the each DNA

were manually annotated. A second point near the start of the DNA molecule was needed to define an initial tangent. After determining an initial tangent vector, the algorithm then iteratively update its estimation of the tangent vector until it reaches the opposite end of the DNA. The algorithm did not converge in roughly 20% of cases (*i.e.* took over 1000 steps of length 2 nm on a 680 nm piece of DNA), due to the presence of loops in DNA causing recursion. The analysis for the automatically generated contours was the same as described for the manually annotated data, except the computationally generated contour was used directly (**i.e.,** there was no spline interpolation for the automatically traced data).

3.6 Author contributions

P.R.H. and T.T.P. designed the experiment. P.R.H optimized the assay conditions and acquired all of the data. P.R.H. developed the analysis techniques and algorithms. P.R.H. and T.T.P. wrote the manuscript.

3.7 Acknowledgments

We thank Anne Gooding and Tom Cech for their gift of the trinucleosome array.

3.8 Supporting Information

3.8.1 Figures

Figure 3.7: Determining persistence length from AFM images. (A) AFM images of DNA deposited under biophysically relevant ionic conditions per our protocol as outlined in Figure 3.2. (B) A human-annotated spline denoting the DNA configurations shown in panel A. The path length along the configuration is s and θ is the angle between the tangent vectors separated by s. (C–D) Plots of angular correlation as a function of s. When plotted as –ln $<\cos(\theta)>$ vs s, the data yields a linear relationship. A fit to the equation $\ln(<\cos(\theta(s))>) = -s/2p$ yields the persistence length (p). A single trajectory is shown in panel C while the average value of 130 molecules is shown in panel D. The solid green line represents the mean value and the green shading denotes the standard error of the mean across all 130 molecules (though the error is so small as to look like a line). Fit shown as a dashed line.

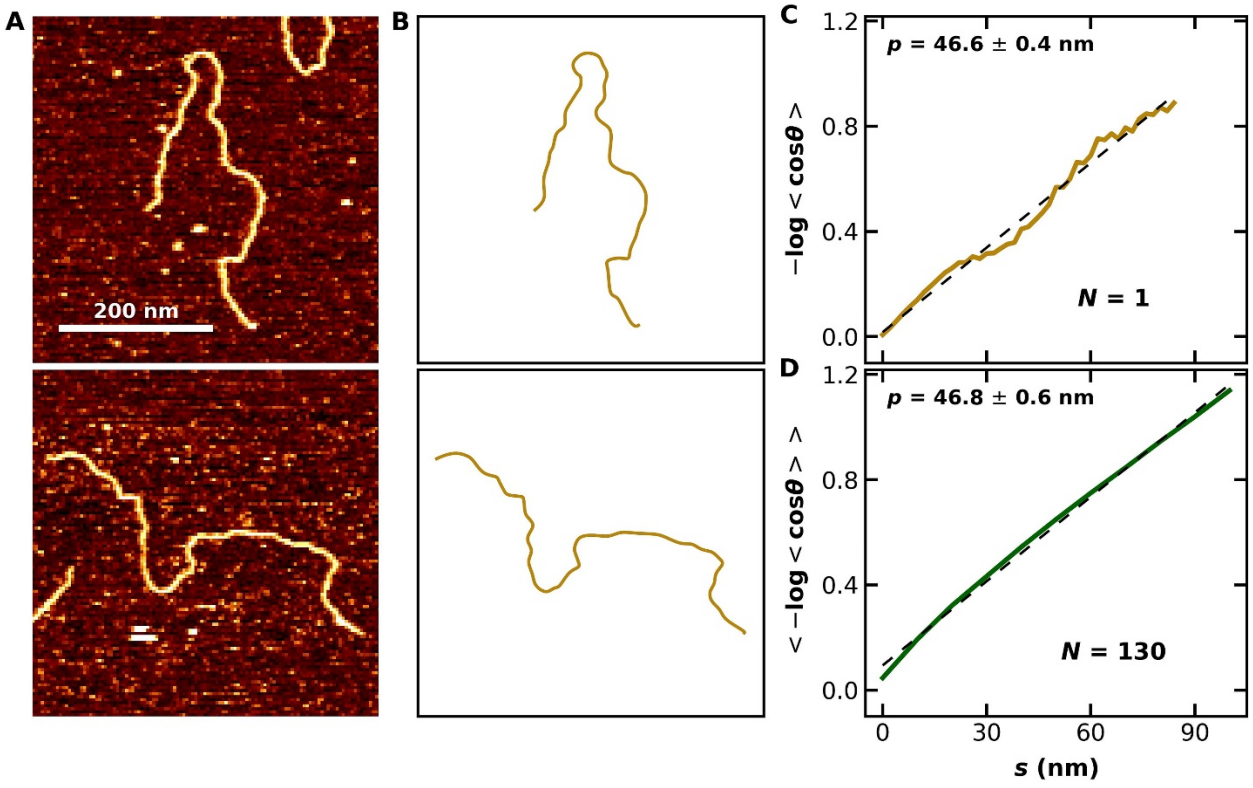

Figure 3.8: Drying method after $NiCl_2$ treatment influences data quality. For the two conditions tested, the yield (purple) and the persistence length p (green) are plotted using the left and right vertical axis, respectively. The surfaces were prepared using (left) our final protocol, including drying by a filter paper, and (right) the final protocol, except drying by a gentle stream of N_2 gas for one minute. Note, that in both conditions tested, the drying occurs before DNA deposition.

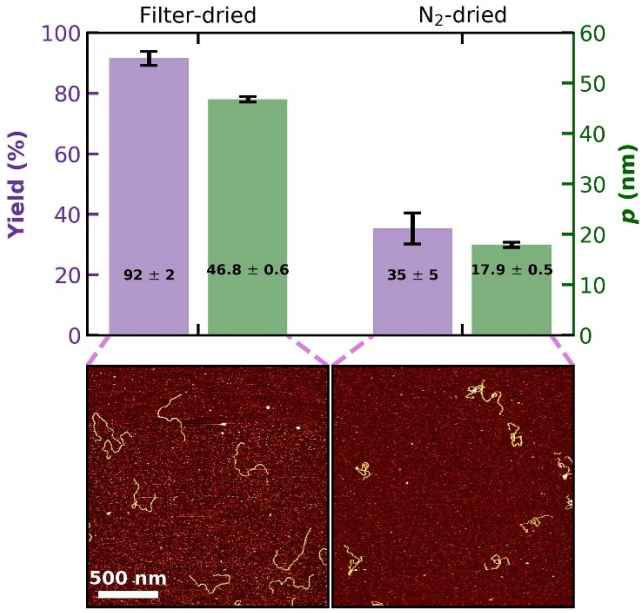

Figure 3.9: Higher concentration of $NiCl_2$ during pre-treatment improves subsequent imaging. (A–B) The percentage yield of interpretable DNA molecules and their corresponding persistence length (p) plotted as a function of the concentration of the $NiCl_2$ used in the pre-incubation step. The deposition condition, rinsing, and imaging conditions were per the standard final protocol, which is 10 mM $MgCl_2$ + 25 mM KCl for deposition and rinsing, and 10 mM $NiCl_2$ + 25 mM KCl for imaging as detailed in Figure 3.2. Approximately 140 molecules were analyzed per condition tested. (C) Sets of three representative images plotted vertically when 1, 10, 33, and 100 mM $NiCl_2$ was used for the pretreatment.

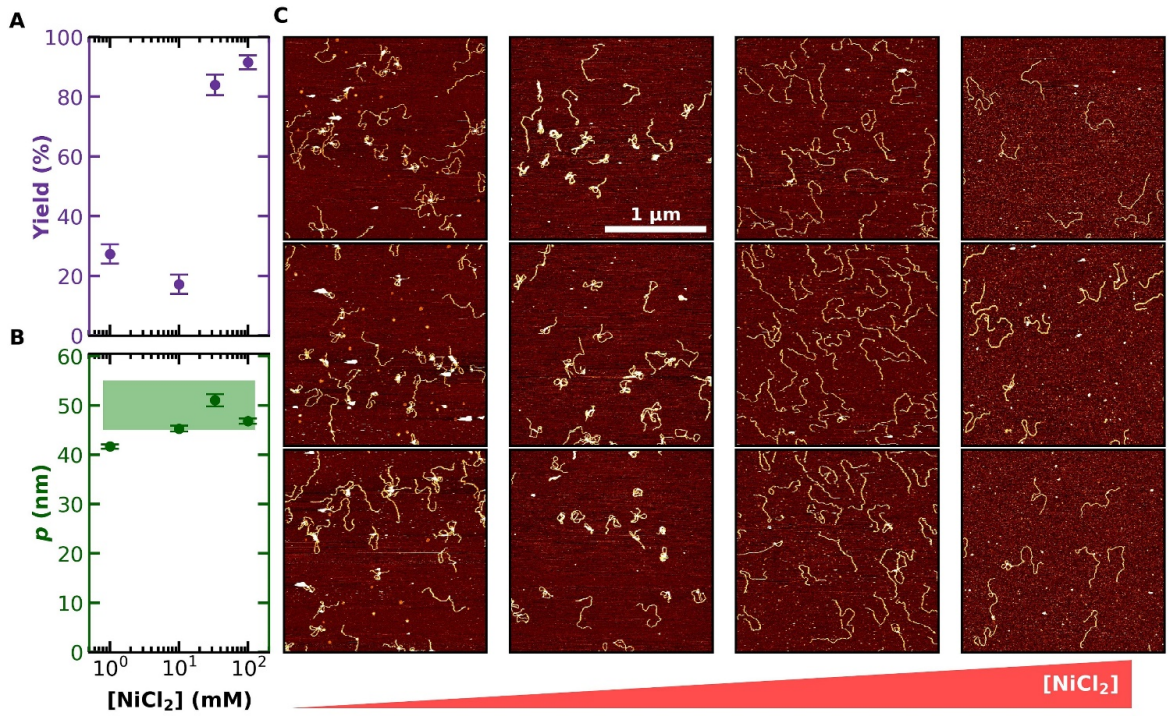

Figure 3.10: Proof-of-principle image resolves a void in the 2D-trimer lattice of bacteriorhodopsin. This image was taken using Ni^{2+}-treated mica, illustrating that such Ni^{2+}-treated mica can be used for other biophysical systems. We note this image was not optimized by typical techniques used high-resolution imaging of bacteriorhodopsin, such as selecting for a particularly sharp tip (1 in 20).

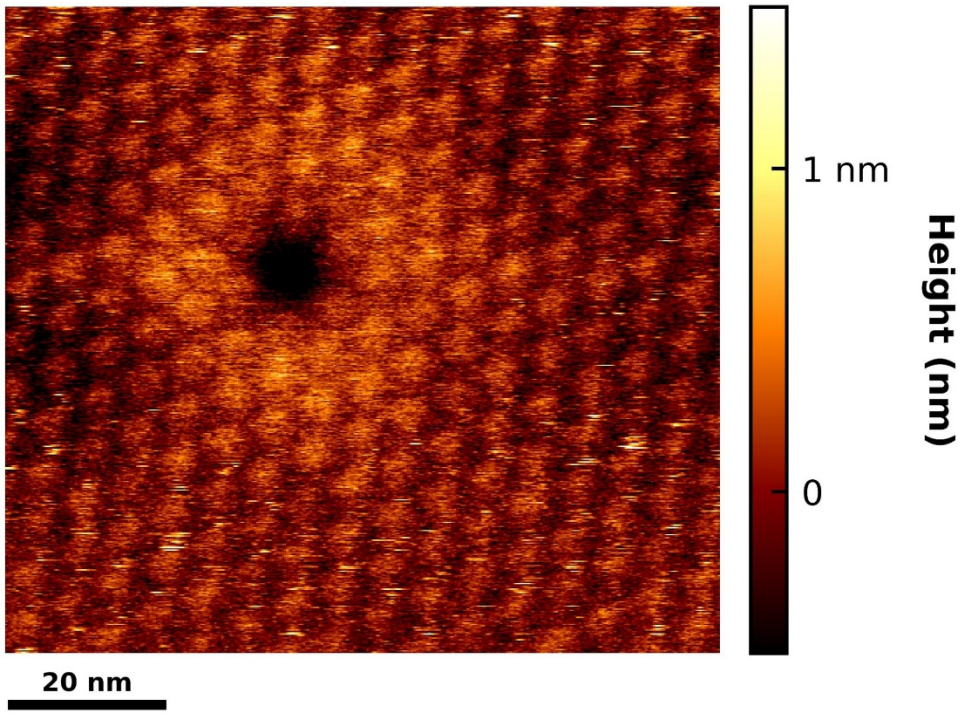

Figure 3.11: Depositing and imaging DNA at biologically relevant ionic conditions. Comparison of our standard protocol that deposits in 10 $MgCl_2$ + 25 mM KCl and images in $NiCl_2$ + 25 mM KCl to depositing and imaging in 3 mM $MgCl_2$ + 50 mM KCl, ionic conditions typically of many protein-nucleic acids. Quantification of 40 molecules showed that persistence length (p) remained high, indicating an equilibrated conformation on the DNA (as expected for a buffer containing $MgCl_2$). The yield was reduced due, in part, to the technical difficulties associated with imaging DNA weakly bound to the mica. That said, the yield was still relatively high (58%), which is excellent given the historical difficulties of imaging DNA on Ni^{2+}-treated mica in the presence of $MgCl_2$, [47] let alone $MgCl_2$ + KCl. Imaging under these conditions required lower set points during tapping mode imaging. In addition, since the DNA was less well bound, the risk of tip fouling and motion of the DNA is increased relative to our standard protocol (potentially a feature for high-speed AFM studies). Note, the successful demonstration of imaging in $MgCl_2$ + KCl by tapping mode leveraged the other incremental improvements of the deposition protocol illustrated in Figure 3.3 (*e.g.*, pre-treating with 100 mM $NiCl_2$, drying with filter paper, gentle but extensive rinsing).

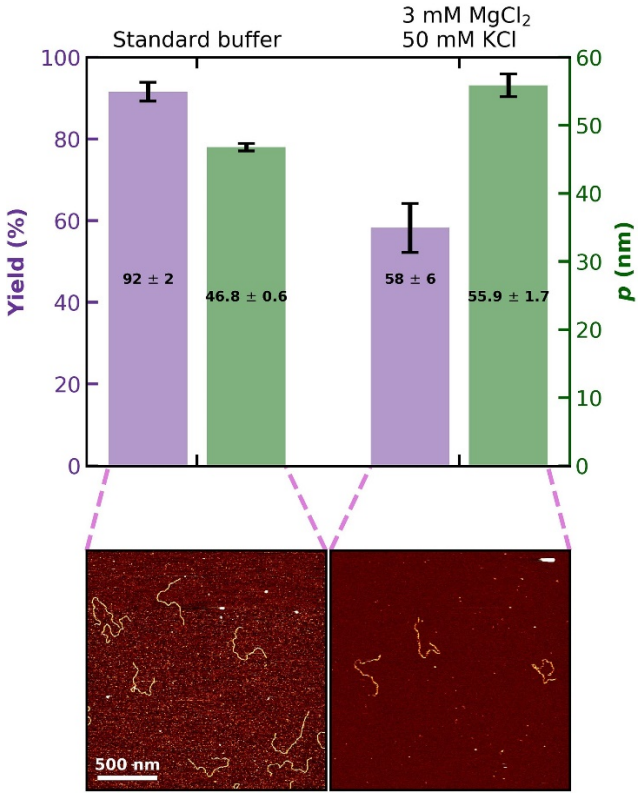

Figure 3.12: Partial dewetting of the sample decreases data quality. The "Solvated" surfaces were prepared using the standard protocol whereas partial dewetting of the sample occurred in the "Dewet" sample. More explicitly, results shown in the right column were disrupted by a meniscus force generated by adding too much liquid to the mica surface. In contrast, the data shown in the left column was rinsed using a gentle fluid flow through the sequential addition and removal of liquid using a micropipette. For both the left and right datasets, the total volume of liquid exchanged remained constant at about 10 mL, as detailed in Figure 3.2. The yield (purple) and the persistence length p (green) are plotted using the left and right vertical axis, respectively. Representative images for each condition are shown below.

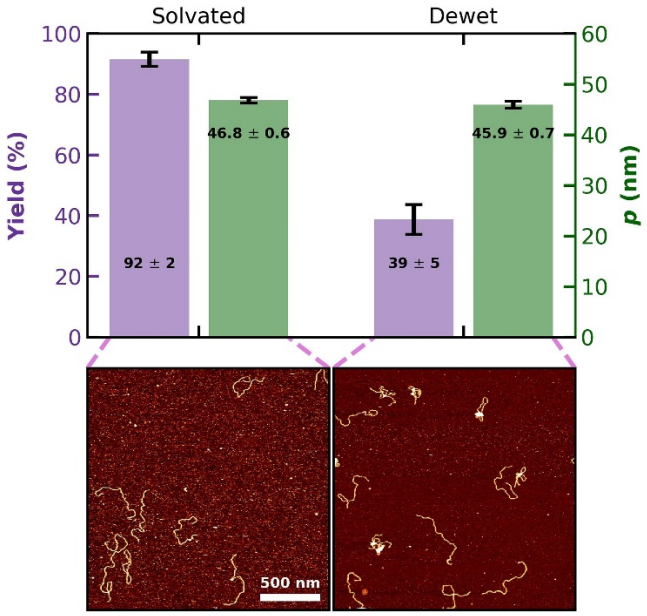

Figure 3.13: Concurrence between the number of experimentally observed looped configurations and a simulation of a 2D WLC equilibrated on a surface. (A) A gallery of simulated configurations where configurations containing no loop are colored green while those containing a loop are colored purple. (B) Histogram of the fraction of looped DNA molecules based upon 100 simulations of 100 configurations. The simulated fraction of looped structures was 22 ± 4 % (mean ± std. dev.) agrees with the measured value 20% derived from 142 individual molecules. We note that in the presence of excluded volume effects, we would expect the fraction of looped DNA in the simulation to be lower.

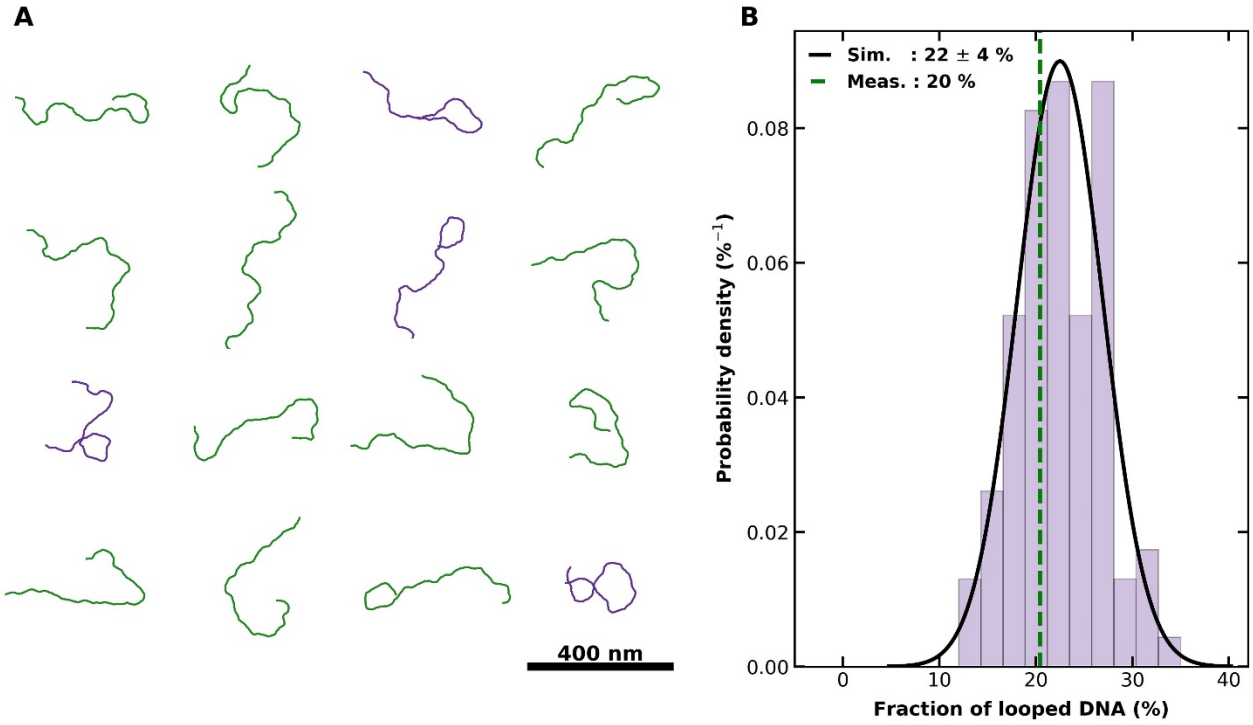

Figure 3.14: End-to-end distance of DNA is consistent with 2D WLC equilibrated on a surface. (A) Cartoon of an example DNA image showing the end-to-end distance ($R_{\text{end-to-end}}$, purple arrow) as a function of arc length along the molecule (s, green line). (B) Mean $R_{\text{end-to-end}}$ as a function of s for all 101 unlooped molecules at the standard salt conditions [10 mM divalent salt, 25 mM KCl]. Green dotted line and shaded area give mean and standard error of the mean at each L, and the purple line is a least-squared fit weighted by the error at each L yielding a persistence length of 45 ± 4 nm (mean ± standard deviation).

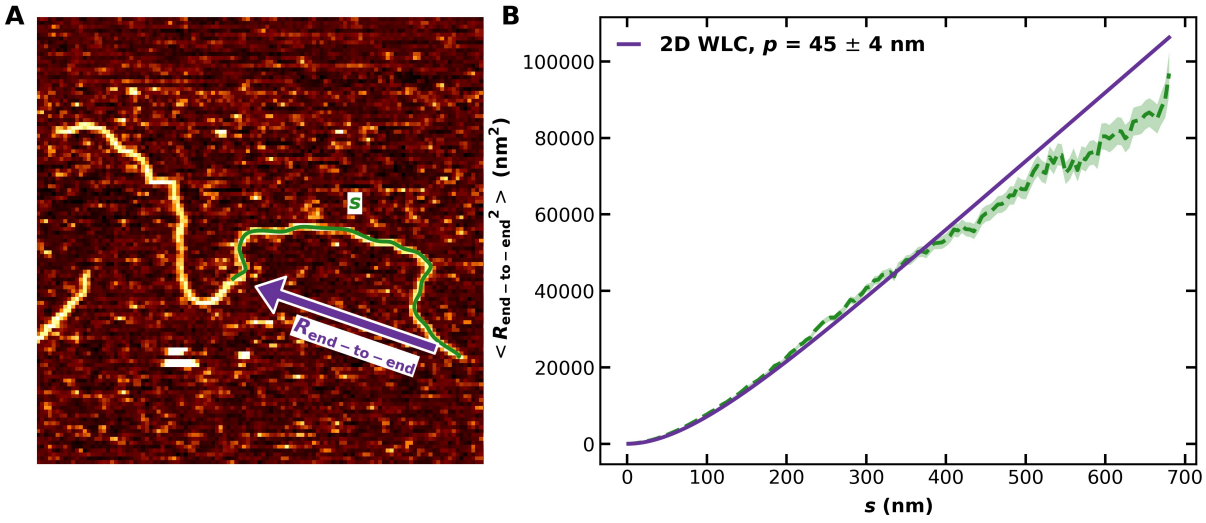

Figure 3.15: Contour and persistence lengths obtained from human and computationally annotated data are consistent. (A) An example DNA molecule shows a high signal to noise. (B) The same image as panel (A), with a manually annotated spline overlayed as a green line. (C) The same image as panel (A), with an automatically annotated contour overlayed. The automatic annotation is detailed in the methods section. (D and E) Comparing the automated and manual determinations of persistence lengths and contour length yields good agreement between human- and machine- annotated data. The values obtained by the automated contour tracing for p and L_0 were 44.9 ± 0.4 nm and 680 ± 70 nm (mean ± std. dev.), respectively. The values obtained by the human-annotated data as 44.6. ± 0.6 nm and 683 ± 13 nm (mean ± std. dev.), respectively.

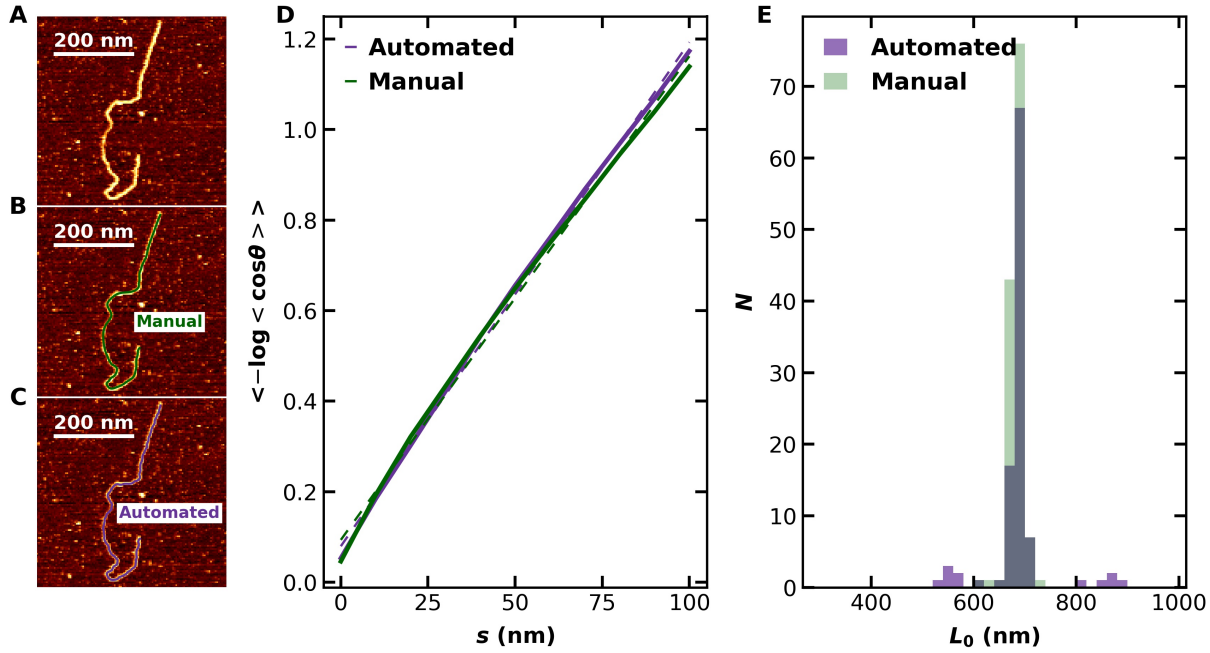

Figure 3.16: Measured height of the DNA. (A) Images of the DNA taken under our typical conditions (see AFM imaging). Line scans (green) and traces (purple) are overlaid. (B) The height from the line scan (green) and trace along the DNA (purple) from panel A are plotted versus the distance along the line scan and the path along the DNA backbone, respectively. Notably, the data concurs with the expected width of the DNA helix (2.0 nm). (C) Histograms of the height along the contour length skeletonized DNA configurations derived from the raw images. Note, the top 0.5% of heights, representing rare line noise or surface defects, were ignored.

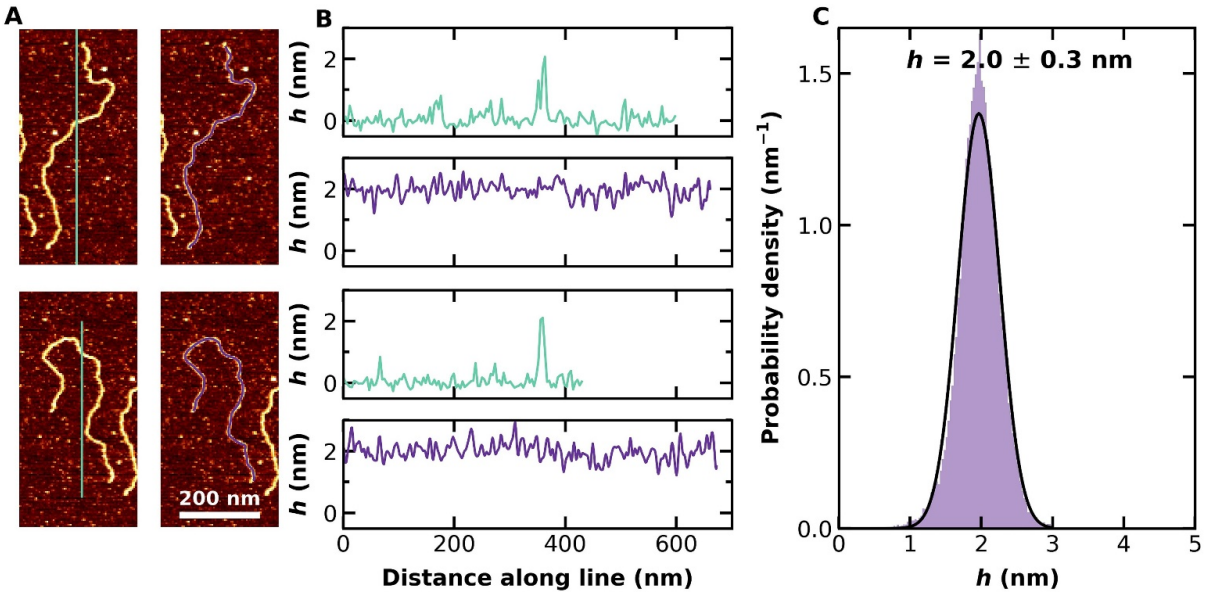

Figure 3.17: Characterizing the surface roughness of mica in liquid for different mica treatment protocols. The top plot lists the standard deviation (σ) of the height for untreated mica, mica treated with the protocol described in this work, and mica treated with APTES 0.1% as described in Materials and Methods. Note, no DNA was deposited on these surfaces. Below each measurement of σ are representative images and the distribution from which the σ was deduced. Error bars in the top panel are standard deviations of σ from 3 separate images, each with about 250 thousand points.

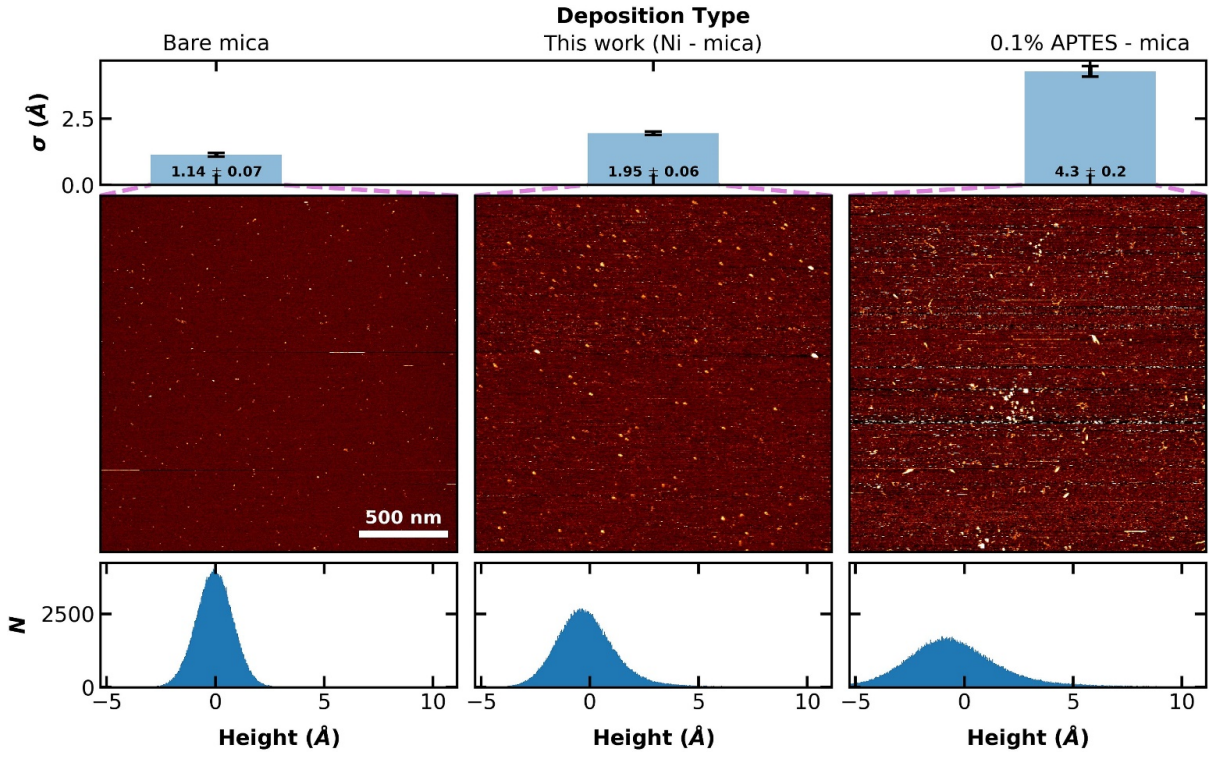

Figure 3.18: High-resolution imaging reveals the right-handed helical structure of DNA. (A). Successive images of the same DNA molecule. These images were fit with a third order, two-dimensional spline to subtract the background, then smoothed with a Gaussian with a width of two pixels (1 pixel = 0.5 Å). (B) Histogram of the helical pitch measured from 15 images of 4 molecules using 3 different tips, where N is 89 and represents the number of individual helical turns measured. A Gaussian fit to the measured distribution yields 3.51 ± 0.40 nm (mean ± std. dev.). The uncertainty in the mean helical pitch is 0.04 nm as defined by the standard error in the mean.

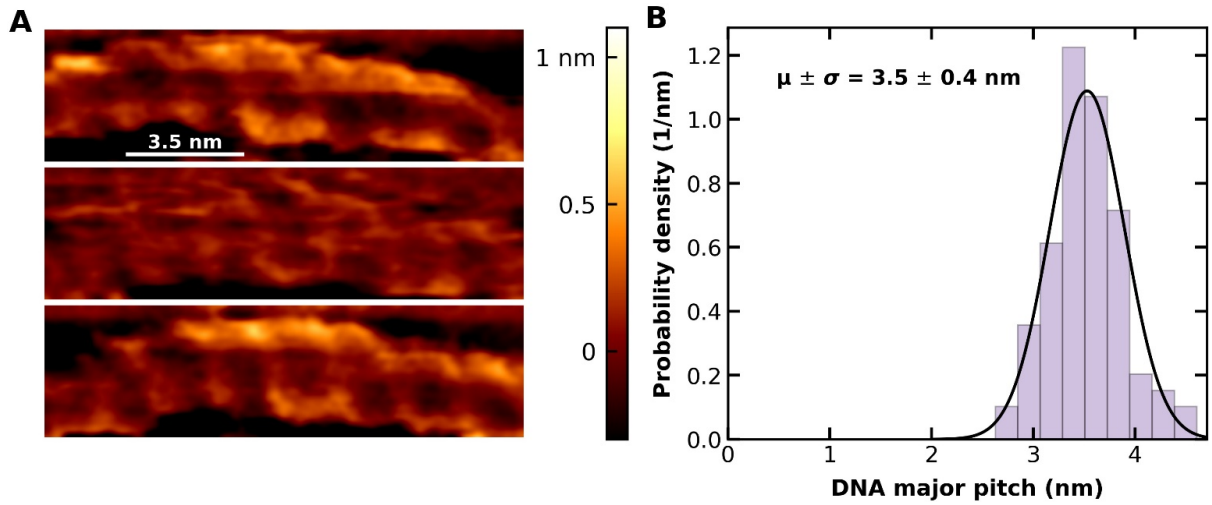

Figure 3.19: Measured contour length agrees within 1% of the expected contour length for B-form DNA. (A) Raw DNA image with a diagram illustrating the contour length L_0 used to measure distance along the configuration. We note the actual contour length is calculated by manually tracing the entire DNA molecule, as illustrated in Figure 3.7 B is 680 nm based upon the number of base pairs times the rise per base pair for B-form DNA (2,000 bp × 0.34 nm/bp). (B) Histogram of from 130 molecules. A fit to the measured distribution (black line) yields 683 ± 13 nm showing that was within 1% of 680 mn.

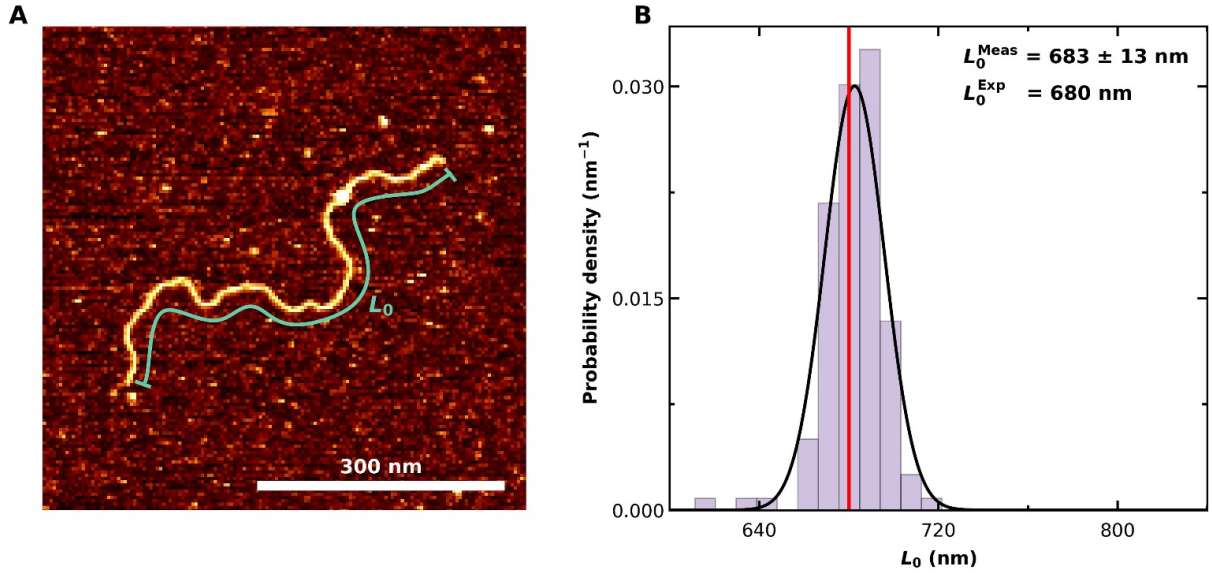

Figure 3.20: Images of short (300-bp) DNA deposited using our protocol. A slightly higher deposition concentration (4 nM) was used given the reduced likelihood of 100-nm DNA forming internal loops or overlapping with adjacent molecules.

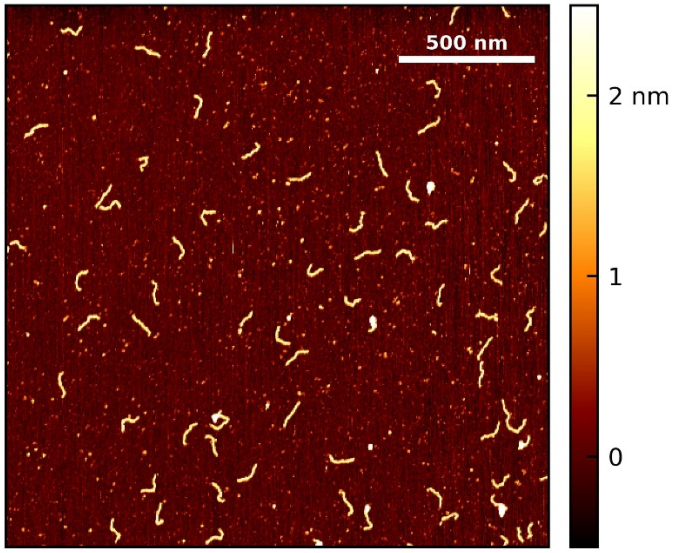

Figure 3.21: Dependence of persistence length on ionic strength is consistent with 2D equilibrated DNA. The total persistence length (p, red markers give mean ± standard deviation) from Figure 3.5 is plotted versus ionic strength (I). A blue dotted line represents the following dependence of the total persistence length in nanometers on ionic strength in molar units: $p = p_{\text{non-electrostatic}} + 0.0324/\text{I}$. The non-electrostatic component of the persistence length ($p_{\text{non-electrostatic}}$) is consistent with an 2D equilibrated conformation (~50 nm). The point with the largest ionic strength (black marker) is omitted, since the high salt inhibits binding of DNA to the surface and artificially lowers the persistence length. Note the dependence of p on the ionic strength I is calculated using [100], assuming that 10 mM $MgCl_2$ has an effective ionic strength of 30 mM.

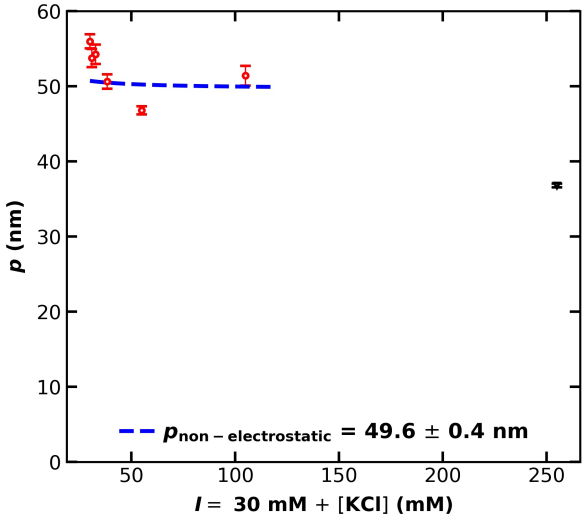

Figure 3.22: Efficient deposition and imaging is possible with little or no divalent cations in solution. (A–B) The percentage yield of interpretable DNA molecules and their corresponding persistence length (p) plotted as a function of divalent ionic concentration at fixed KCl (25 mM). Error bars represent the standard deviation for the yield and the fitting error for the persistence length, as in Figure 3.3. On average, 120 molecules were analyzed per condition. (C) Sets of three representative images plotted vertically acquired at 0, 1.25, 2.5, 5 and 10 mM divalent cations. We note both concentrations of $MgCl_2$ and $NiCl_2$ in the deposition and imaging buffers were varied at the same time to keep a consistent divalent ionic strength at each condition tested.

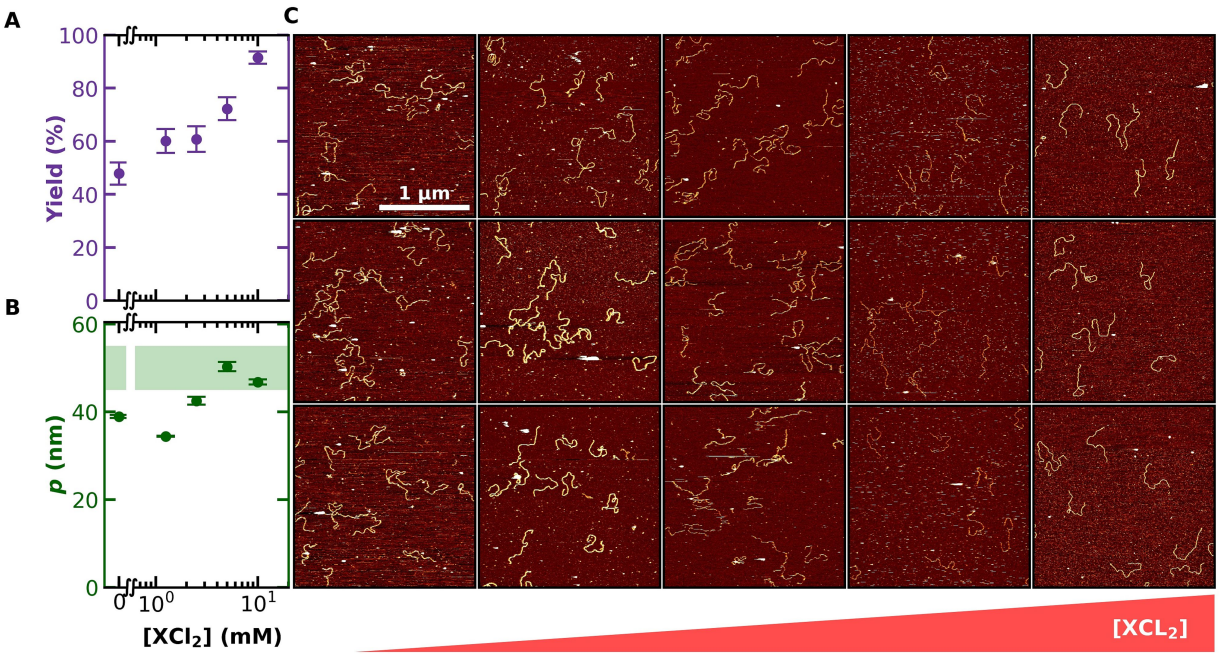

Figure 3.23: Replacing $NiCl_2$ for $MgCl_2$ during deposition leads to kinetically trapped configurations even when using our final protocol that includes extensive but gentle rinsing. (A) A set of tapping-mode images of DNA in liquid deposited under different deposition protocols as summarized in each box. The change between each deposition process is highlighted with blue text and protocols associated with images are denoted with magenta boxes. (B–C) The percentage yield of interpretable DNA molecules and their corresponding persistence length (p) is depicted below each protocol. These values were computed from ~95 DNA molecules per condition. Error bars represent the standard deviation for the yield and the fitting error for the persistence length (p). Persistence length was deduced using a 2D WLC model. Overall, DNA deposited in $NiCl_2$ showed more compact structures leading to reduced yield and a lower p for those conformations that were interpretable. These results are consistent with the long-standing conclusion that these conditions would lead to kinetically trapped configurations. Note that our series of improvements in the deposition process significantly improved the yield and interpretability of the images when comparing the left most and right most image in panel A.

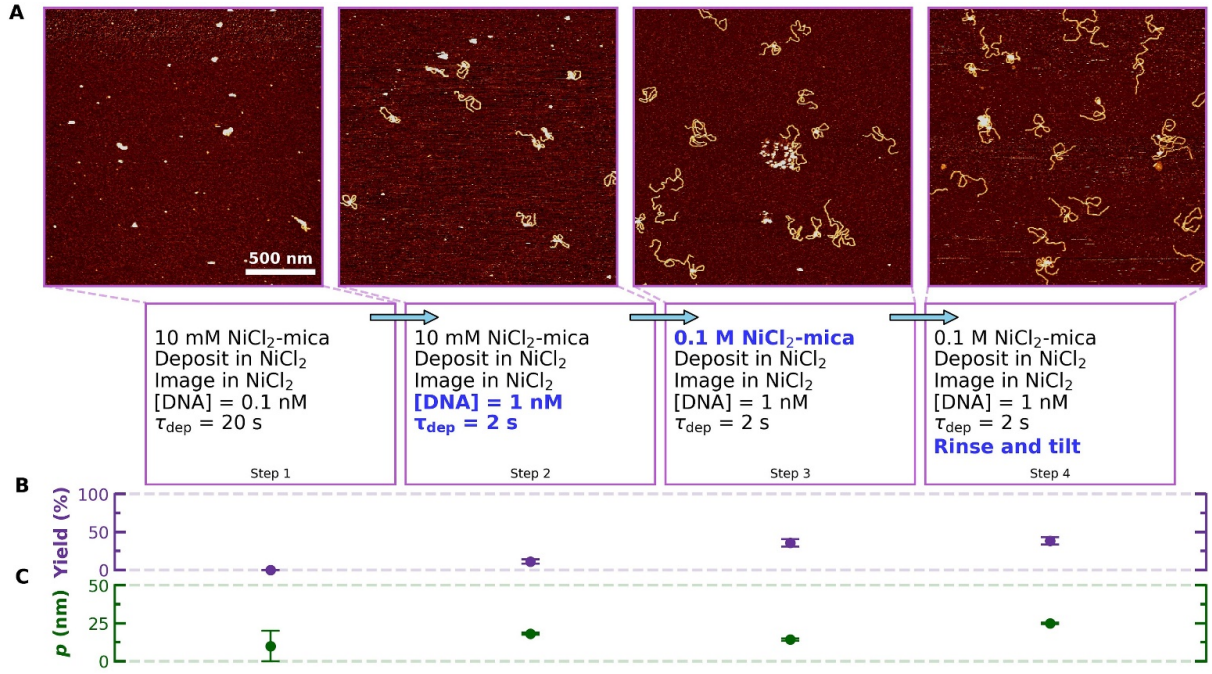

Figure 3.24: Age of $NiCl_2$ powder appeared to influence data quality. Age of $NiCl_2$ powder appeared to influence data quality. The yield (purple) and the persistence length p (green) are plotted using the left and right vertical axis when using $NiCl_2$ of different ages and stored under different conditions. (left) Images acquired using stock $NiCl_2$ solution made from freshly purchased $NiCl_2$ powder immediately after first opening. (middle) Images acquires using stock 1 M $NiCl_2$ solution stored at 4 °C for 7 months, and (right) Images acquires using stock $NiCl_2$ solution made after storing $NiCl_2$ powder for 7 months. Hence, if poor results are observed with $NiCl_2$ powder that is not recently purchased, we suggest purchasing fresh $NiCl_2$ powder and immediately suspending it in a concentrated stock solution that is stored at 4 °C.

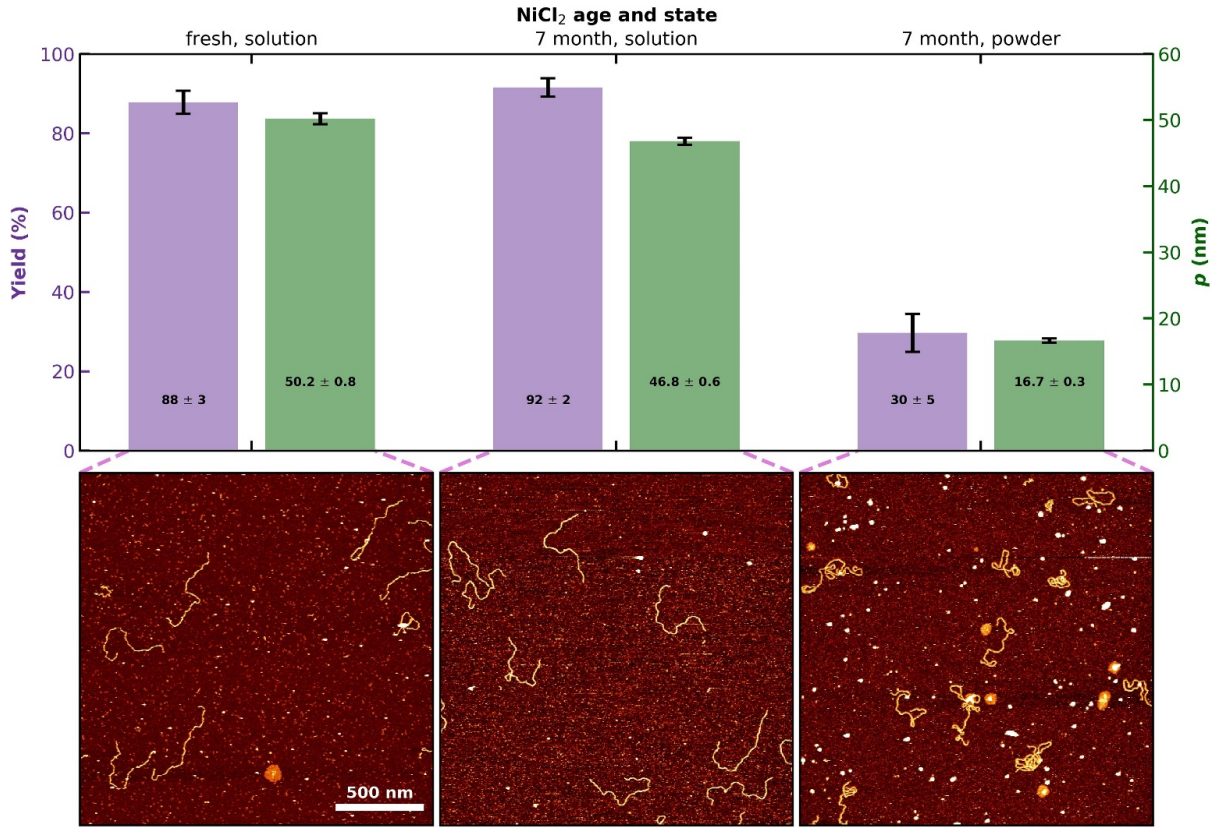

Chapter 4

FEATHER: Automated Analysis of Force Spectroscopy Unbinding/Unfolding Data via a Bayesian Algorithm

This chapter and its supporting information were adapted from [110]:

Patrick R. Heenan and Thomas T. Perkins. FEATHER: Automated Analysis of Force Spectroscopy Unbinding and Unfolding Data via a Bayesian Algorithm. **Biophysical Journal**, 115(5):757–762, September 2018.

4.1 Abstract

Single-molecule force spectroscopy (SMFS) provides a powerful tool to explore the dynamics and energetics of individual proteins, protein-ligand interactions, and nucleic-acid structures. In the canonical assay, a force probe is retracted at constant velocity to induce a mechanical unfolding/unbinding event. Next, two energy landscape parameters, the zero-force dissociation rate constant (k_{o}) and the distance to the transition state ($\Delta x^{\ddagger}$), are deduced by analyzing the most probable rupture force as a function of the loading rate, the rate of change in force. Analyzing the shape of the rupture force distribution reveals additional biophysical information, such as the height of the energy barrier ($\Delta G^{\ddagger}$). Accurately quantifying such distributions requires high-precision characterization of the unfolding events and significantly larger datasets. Yet, identifying events in SMFS data is often done in a manual or semi-automated manner and is obscured by

the presence of noise. Here, we introduce a new algorithm, FEATHER (**F**orce **E**xtension **A**nalysis using a **T**estable **H**ypothesis for **E**vent **R**ecognition), to automatically identify the locations of unfolding/unbinding events in SMFS records and thereby deduce the corresponding rupture force and loading rate. FEATHER requires no knowledge of the system under study, does not bias data interpretation towards the dominant behavior of the data, and has two easy-to-interpret, user-defined parameters. Moreover, it is a linear algorithm, so it scales well for large datasets. When analyzing a dataset from a polyprotein containing both mechanically labile and robust domains, FEATHER featured a 30-fold improvement in event location precision, an 8-fold improvement in a measure of the accuracy of the loading rate and rupture force distributions, and a 3-fold reduction of false positives in comparison to two representative reference algorithms. We anticipate FEATHER being leveraged in more complex analysis schemes, such as segmentation of complex force-extension curves for fitting to worm-like-chain models, and extended in future work to datasets containing both unfolding and refolding transitions.

4.2 Introduction

Over the last ~25 years, single-molecule force spectroscopy (SFMS) has emerged as a powerful tool to quantify diverse biological systems, including the strength of protein-ligand bonds [29, 30] and the unfolding and refolding of individual protein domains [25, 26]. In one widely used assay, an atomic force microscopy (AFM) cantilever or an optically trapped bead is attached to the biological system under study and retracted at constant velocity (Figure 4.1 *A*). Force is deduced as the displacement of the force probe away from its equilibrium position. Abrupt drops in force at the rupture force (F_{R}) arise from unfolding/unbinding events (Figure 4.1 *B*). Because these events are thermally activated, there is not a unique rupture force but rather a distribution (Figure 4.1 *C*). The Bell-Evans model rapidly emerged as a way to characterize a 1D projection of the underlying free-energy landscape along the stretching axis [30, 111, 112]. In this analysis, a fit to the most probable rupture force (F_R^{MP}) as a function of loading rate yields two parameters, the zero-force

dissociation rate constant (k_o) and the distance to the transition state ($\Delta x^{\ddagger}$) (Figure 4.1 *D*). More advanced models that analyze the shape of the F_R distribution provide additional information on the free-energy landscape, such as the height of the energy barrier ($\Delta G^{\ddagger}$) [52] but require higher precision event detection and larger numbers of events. Yet, event detection is obscured due to the presence of Brownian motion and instrumental noise and is often done manually or in a semi-automated manner, including in recent work from our lab [69]. Thus, accurately quantifying hundreds to thousands of rupture events in an automated, reliable, and reproducible way is critical for gaining insight into the diverse biomolecular systems studied by SMFS.

To address this need, multiple groups have developed algorithms to detect rupture events in AFM data and other SMFS modalities. For example, such techniques have applied worm-like-chain models to compute contour lengths at each extension [113, 114], used thresholding based on signal or noise characteristics [115, 116], and classified traces based on transformations of the data into frequency or derivative spaces by spatially localized Fourier series or wavelets [117–119]. These methods provide increased automation, but their use is limited by their lack of generalization. Ongoing efforts and interest in automated analysis continues [*e.g.*, recent work integrated several steps in SMFS analysis of unfolding data into a single package [120]]. Contour-length alignment algorithms bias results towards dominant features and necessarily require a model. Thresholding or transformation algorithms typically require many parameters. For example, previous techniques have 6 [118, 119] and even up to 14 or 17 parameters [120, 121]. Large numbers of parameters help tune an algorithm to a particular dataset, but they also increase the search space for parameter optimization and may be difficult to apply to datasets containing unfolding events occurring over a broad range of forces.

Here, we present a new algorithm for detecting unfolding/unbinding events and apply it to SMFS datasets representative of a variety of typical experimental conditions. The algorithm, named FEATHER (**F**orce **E**xtension **A**nalysis using a **T**estable **H**ypothesis for **E**vent **R**ecognition), requires no special knowledge of a specific system's polymer properties, detects both rare and dom-

Figure 4.1: An overview of force spectroscopy analysis. (A) A cartoon illustrating an AFM cantilever unfolding a polyprotein containing four mechanically robust domains (NuG2, red) and one mechanically labile one (α_3D, blue). (Inset). A sketch of a 1D free-energy landscape and associated parameters: k_o, the zero-force dissociation rate constant; $\Delta x^{\ddagger}$, the distance to the transition state; and $\Delta G^{\ddagger}$, the height of the energy barrier. (B–D) Typical analysis scheme for a polyprotein unfolding assay illustrated with a computationally generated dataset based on a model by Dudko and colleagues ([52]). (B) A force-vs.-time curve for the unfolding of the polyprotein with segments colored coded based on the domain prior to unfolding. (C) A distribution of rupture forces (F_{R}) for the α_3D domain fit to the Dudko model. (D) Most probably rupture force (F_{R}^{MP}) versus log of the loading rate ($\partial F/\partial t$) fit with a line per the Bell-Evans model ([30, 111, 112]). (E) An experimental force-vs.-time curve of the polyprotein shown in panel *A*, with unfolding events marked by green arrows. Colored coded data was smoothed to 500 Hz with higher-bandwidth data (50 kHz) plotted in grey. (F) A high-time resolution plot of a single rupture event used to define metrics for comparing automated algorithms: a true event is manually defined by an expert user as detailed in the Supporting Material; $\mathbf{d}_{\mathrm{t}\to\mathrm{p}}$ is the distance from a true event to the closest predicted event; and $\mathbf{d}_{\mathrm{p}\to\mathrm{t}}$ is the distance from an algorithmically predicted event to the closest true event. Predicted events are illustrative, not actual.

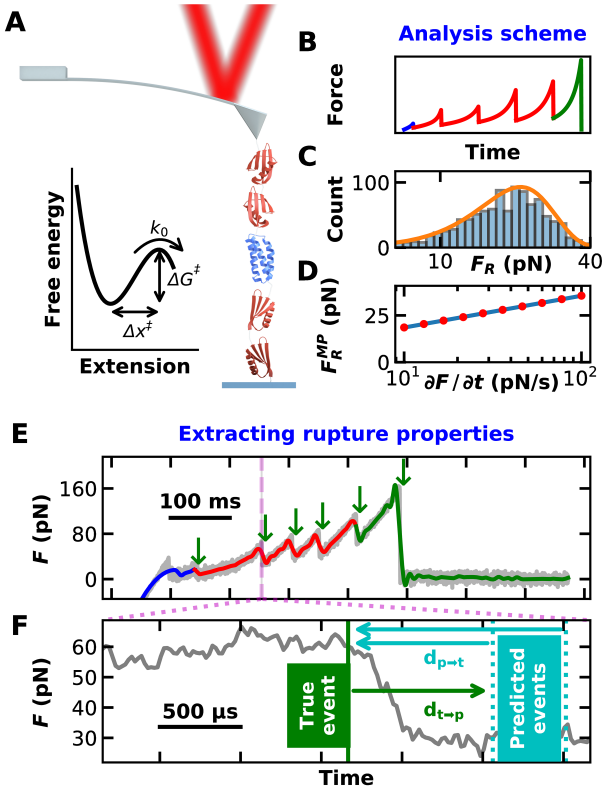

inant data behavior, and outperforms recently published algorithms over a wide range of pulling velocities and two common systems of interest (polyproteins and DNA) and a computationally generated dataset. FEATHER is a Bayesian algorithm because it calculates the probability of each point in the retraction curve given a model automatically calculated from the event-free approach curve. Because FEATHER's improved performance requires just two easy-to-interpret parameters, a smoothing factor and a significance threshold, we anticipate FEATHER being leveraged to improve the throughput, quality, and reproducibility in SMFS analysis schemes.

4.3 Materials and Methods

FEATHER is written in Python 2.7, with interfaces written for MATLAB and Igor Pro. The source code, working examples, and accompanying documentation is freely available (`https://doi.org/10.5281/zenodo.1306884`). Importantly for analyzing large datasets, FEATHER's execution time scaled linearly with the number of data points and offered an order of magnitude improvement in runtime relative to the faster of the two algorithms used for comparison (Figure 4.4). The basis for the statistical analysis used by FEATHER and performance metrics are presented in the Supporting Material. All timing and tuning results were obtained using a desktop PC with 32 GB of RAM, an AMD Ryzen 5 1500X Quad-Core CPU, and a 500 GB hard drive. To test FEATHER, we used two datasets: (i) 152 force-extension curves of a previously described polyprotein that contains one mechanically labile target protein (α_3D) with a measured change in contour length (ΔL_0) of 23 nm upon rupture (8) positioned between four mechanically robust marker domains of NuG2 [ΔL_0 = 18 nm per NuG2 monomer [122]] (Figure 4.1 *A* and Table 4.2), and (ii) 600 force-extension curves of DNA deposited at purposely high surface coverage to promote multiple tip-DNA attachments and therefore multiple rupture events per force-extension curve (Figure 4.5 and Tables 4.3–4.4). As described in detail in the Supporting Material, both datasets contained curves acquired over a range of retraction velocities (v). Finally, FEATHER's performance was tested using a simulated dataset containing purposely challenging-to-analyze force-

extension curves, as described in the Supporting Material.

4.4 Results and Discussion

4.4.1 Description of FEATHER

In SMFS, unfolding events occur when the force applied to a molecule exhibits an abrupt drop in a force-vs.-time curve as the molecular configuration passes over an energy barrier (Figure 4.1 *E*, green arrows). To determine the location of such events, FEATHER first fits a smoothing spline to the raw data (Figure 4.2 *A*) with nodes in the spline spaced at a user-defined fractional spacing (τ) of the full record length, so the temporal averaging time (5–50 ms) depends on v given a fixed data acquisition rate, as is typical in such assays. While the model defined by the spline has a continuous first derivative, unfolding events exhibit a discontinuity in the first derivative. Thus, unfolding events could be located by computing where the data were inconsistent with the model. To efficiently detect short-lived events, we recommend users choose the largest τ that preserves such events in the smoothed data (Figure 4.6).

To compute the statistical significance of an unfolding event at time t, we constructed a *no-event hypothesis* based on the noise characteristics of the data relative to a reference curve lacking any events. For AFM data, the approach curve taken with the same individual cantilever served as an excellent reference. Briefly, the process of computing the significance (P) of an event started by subtracting the smoothing spline from the high-bandwidth data to yield a force residual with a zero-centered mean and variance about that mean (which contained mostly the thermal noise of the system within a fractional size of the record defined by τ). The magnitude of this residual variance as a function of time is compared to the approach curve that contained no unfolding/refolding events. Alternatively stated, we determined how the variance of the force variance changes in time since this metric was found to be insensitive to local variation in curvature of the data but highly

Figure 4.2: FEATHER's analysis scheme. (A) A high-bandwidth force-vs.-time record of polyprotein unfolding (grey) with FEATHER's spline fit overlayed in blue, where $\tau = 15$ ms. (B) The probability (P) of a non-event was obtained by applying Chebyshev's inequality to the record in panel A. Unfolding events occur when this probability is near 0. (C) The probability from panel B transformed to de-emphasize regions near the surface and regions with positive force derivatives. (D) The probability from panel C was further modified to suppress regions where the force change was negligible, as determined from a reference curve with no-events (*e.g.*, the approach). (E–H) Force-vs.-time curves and magnified regions highlight event determination, indicated by green arrows using a significance threshold of $P_{\text{thresh}} = 0.001$.

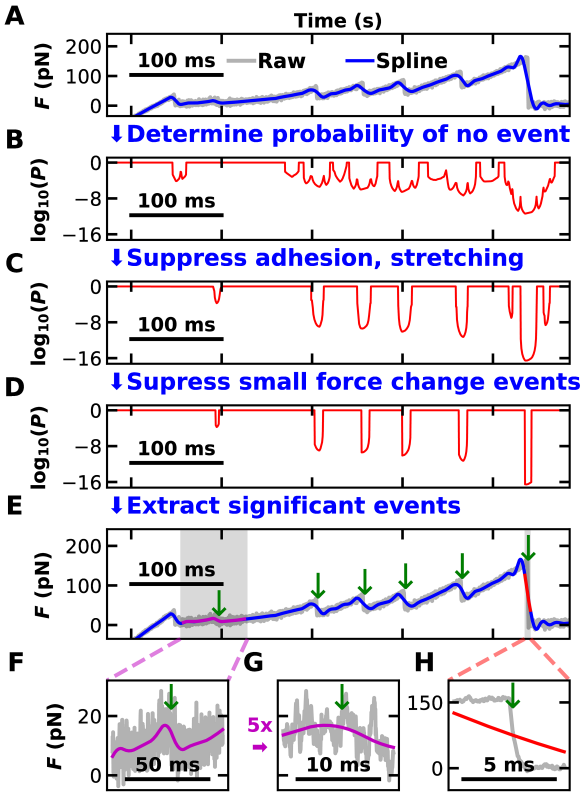

sensitive to unfolding events (Figure 4.7 *F*). Deviation from this mean magnitude of residual noise was transformed into a probability using Chebyshev's inequality (Equation 4.1), which importantly does not assume any form of the noise distribution [123]. We note that FEATHER requires that the noise distribution of the force residuals have zero mean and median, but otherwise does not impose constraints on the distribution.

Empirically, we observed the statistical significance of an event was enhanced by combining the no-event probability for the force in combination with the integral force, force derivative, and force differential, all conceptually based on the same implementation of Chebyshev's inequality as shown in Equation 4.2. For instance, the probability from Figure 4.2 *B* was transformed to de-emphasize stretching of the construct where the force derivative is positive or negligible, and surface adhesion was ignored by including only events that started after the tip was retracted off of the surface (Figure 4.2 *C*). We next suppressed events associated with small force changes consistent with the force noise in the reference (or approach) curve (Figure 4.2 *D*) as described in the Supporting Material (Figure 4.7; see pseudocode listed in Table 4.5). Events were identified from the probability shown in Figure 4.2 *D* based on a user-defined threshold (*e.g.*, $P_{\text{event}} = 0.001$) (Figure 4.2 *E*). Importantly, FEATHER correctly identified rupture events even though the rupture force varied by an order of magnitude within the same record (Figure 4.2 *F*–*H*). Moreover, this high-fidelity event detection was insensitive to a ~10-fold variation in τ and the thresholding parameter (P_{event}), in contrast to other event detection algorithms (see Supporting Material and Figures 4.6–4.8).

4.4.2 Evaluating FEATHER's performance

We evaluated the performance of FEATHER to accurately and precisely analyze the unfolding of our polyprotein, which exhibited both low- and high-force ruptures. Specifically, we compared how well FEATHER did relatively to manually annotated data from an expert user and

two automated analysis routines, the recently published OpenFovea [116] and the wavelet-scheme 'find_peaks_cwt' method from Scientific Python [124]. These algorithms were chosen to provide a representative sample of the viable techniques used in AFM data analysis, since they respectively utilized thresholding and wavelet transformations, two broad classes of event-detection techniques. In addition, neither of these reference algorithms requires specialized knowledge of the polymer under study, such as the worm-like chain model commonly used in contour length alignment algorithms. Three primary metrics were used: the relative location error, the loading rate, and the rupture force (Figure 4.3). We note that each algorithm outputs a list of predicted event locations; the loading rate and rupture force were then calculated in the same way for each algorithm, given the predicted events (see Supporting Material).

Overall, FEATHER did an excellent job, essentially matching the performance of human-annotated data. In comparison to the best performance of either reference algorithm, FEATHER's prediction yielded rupture force and loading rate distributions which were 8-fold closer to the human-annotated data and 30-fold better in an event location metric (ΔZ_{95}), as defined below. The top panel of Figure 4.3 **A** shows the distribution in the relative location error of the "true events," defined by an expert user, relative to predicted events ($\mathbf{d}_{t\to p}$; green shading) closely matched the distance distribution from predicted events to true events ($\mathbf{d}_{p\to t}$; blue line) (see Figure 4.1 *F* for definitions of $\mathbf{d}_{t\to p}$ and $\mathbf{d}_{p\to t}$ and the Supporting Material for details of manual annotation). The peak of this distribution at low relative error shows precision in determining event location. The overlap between the two distributions shows that number of true events closely matched the number of predicted events. However, such overlap was not present when the data were analyzed with OpenFovea, which showed a high number of false positives as indicated by the gap between the distributions of $\mathbf{d}_{p\to t}$ (black line) and $\mathbf{d}_{t\to p}$ (green shading). We speculate that OpenFovea's performance may be limited in this application by a dataset that contains both low- and high-force unfolding events, despite efforts to optimize OpenFovea's parameters for this dataset (see Supporting Material & Figure 4.8). The wavelet-based scheme, which was also had its parameters

optimized for this dataset, showed better performance on this metric than OpenFovea but still had a 30-fold higher relative location error and a 3-fold higher false positive rate than FEATHER (Figure 4.9). Relative to the better performing wavelet scheme, FEATHER improved event localization precision ~30 fold based on ΔZ_{95} (Table 4.1), where ΔZ_{95} is defined as the location of the 95th percentile of the combined distribution for $\mathbf{d}_{p\rightarrow t}$ and $\mathbf{d}_{t\rightarrow p}$ (see Table 4.6 and Figure 4.3 *A*, dashed line). As defined, ΔZ_{95} represents a good metric for the upper bound of the error in determining event location.

As accurate determination of rupture force and loading rate is critical to deriving biological insight from force spectroscopy data [30, 52, 111], we next compared all three algorithms to human-annotated results for these two metrics (Figure 4.3 *B,C*). As shown in the top panel of each column, FEATHER (blue line) essentially matched the human-annotated distributions (green shading) while OpenFovea showed a surplus of low-force unfolding events (black line) arising from its high false positive rate. Again, the wavelet scheme showed intermediate performance (red line). Despite these distributions being oddly shaped due to the presence of both low-force (α_3D) and high-force (NuG2) ruptures over a range of v, we quantitatively compared the degree of overlap between the human-annotated and algorithmic results using Bhattacharya coefficient's complement (BCC, see Table 4.6) [125]. By this metric, FEATHER outperforms the wavelet scheme by a factor of 8 (Table 4.1). We note that in additional tests on a DNA dataset purposely containing multiple tethers that led to multiple, closely spaced unfolding events at low forces (10–30 pN)(*e.g.*, Figure 4.5 *E–F*), we saw even larger performance improvements of FEATHER by these metrics (Figures 4.10–4.11). In addition, FEATHER successfully analyzed hundreds of simulated ruptures over a wide range of contour length changes, loading rates, and rupture forces (Figure 4.12, Table 4.7). Taken together, FEATHER's performance on experimental polyprotein data, an experimental DNA dataset, and a complex simulated dataset underscored the consistent strength of FEATHER's predictive power.

Figure 4.3: Evaluating FEATHER's performance. (A) Histograms of fractional errors between human-annotated and algorithmically predicted event locations for the polyprotein dataset when using FEATHER, OpenFovea ([116]), and the wavelet-based scheme from Scientific Python ([124]), where ΔZ is the combined fractional distance between the identified and predicted events divided by the full range of the record, and the dotted line denotes the location of ΔZ_{95}, where ΔZ_{95} is defined as the location of the 95th percentile of the combined distribution for the fractional error $\mathbf{d}_{\mathrm{p}\to\mathrm{t}}$ and $\mathbf{d}_{\mathrm{t}\to\mathrm{p}}$. As diagrammed in Figure 4.1 F, $\mathbf{d}_{\mathrm{t}\to\mathrm{p}}$ is the distance from a human-annotated "true" event to the closest predicted event; and $\mathbf{d}_{\mathrm{p}\to\mathrm{t}}$ is the distance from an algorithmically predicted event to the closest true event. (**B**) Histograms comparing the loading rates from manual-event annotation (green) to algorithmically predicted ones for FEATHER (blue), OpenFovea (black), and Scientific Python (red), respectively. Note, the green shaded distribution in all 3 panels represents the same dataset but appears slightly different due to variations in bin size. (**C**) Histogram of rupture force for human-annotated and algorithmically determined events using the same color scheme.

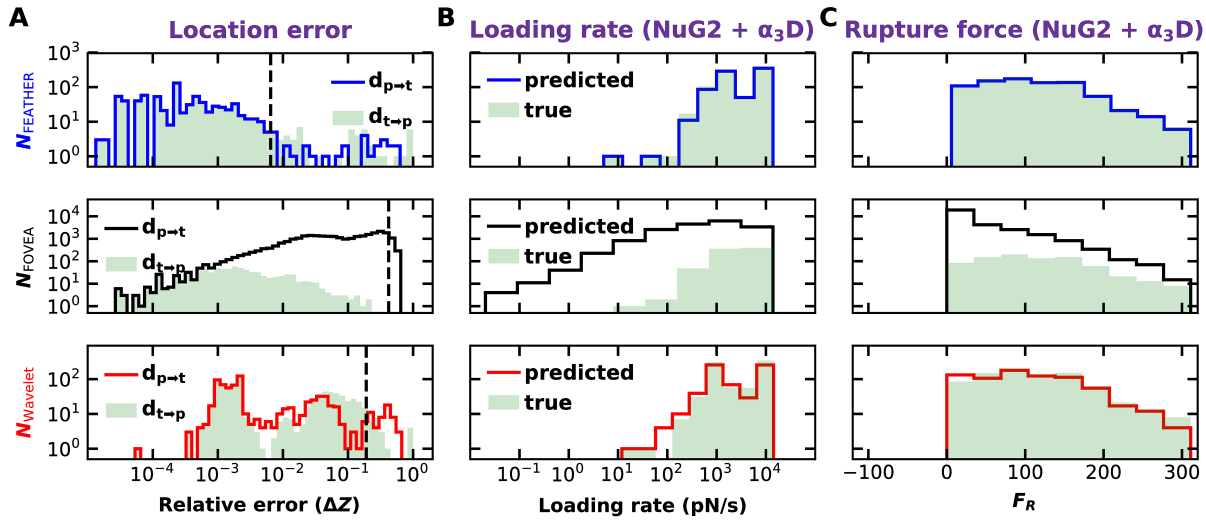

4.5 Conclusion

The canonical single-molecule force spectroscopy assay retracts a force probe at constant velocity to yield records containing unfolding and unbinding events. Here, we introduce FEATHER, which automatically determines event locations for such records and thereby determines the rupture force and loading rate. FEATHER requires only two simple-to-understand parameters to accurately and algorithmically recapitulate human-annotated data. Its fast execution and linear runtime with the number of data points allows for automated analysis of large datasets that, in turn, will allow for more sophisticated analysis that yield additional biophysical information, such as $\Delta G^{\ddagger}$ [52]. When analyzing a complex dataset containing both low- and high-force rupture events, FEATHER provided more than an order of magnitude improvement in event localization error (ΔZ_{95}) relative to other representative algorithms (Table 4.1) and did not bias the data towards high-force events. We note that the datasets used here were acquired with a relatively long, soft cantilever. Recent efforts in improving the precision and time resolution of AFM cantilevers will immediately aid FEATHER's ability to detect smaller and more closely spaced unfolding intermediates [126, 127]. By predicting where events occur without relying upon any *a priori* domain-specific model of the event, FEATHER provides a powerful tool within a longer SMFS analysis pipeline [116, 120]. For instance, it can be used to segment complex force spectra to then determine the change in contour length between ruptures, a value which in turn can be used to screen large datasets for the unfolding of particular structures. Finally, we anticipate that FEATHER's underlying event detection algorithm can be extended to search for both unfolding and refolding events, increasing its utility to a broader array of force spectroscopy assays.

4.6 Open data statement

All of the analyzed force-extension curves, along with their annotation, are available from the Dryad Digital Repository (doi:10.5061/dryad.1615c2p).

4.7 Author contributions

P.R.H. conceived of and developed the algorithm; P.R.H. and T.T.P designed the research; P.R.H. acquired the data. P.R.H. and T.T.P analyzed the data and wrote the manuscript.

4.8 Acknowledgments

We thank J. Boyd-Graber and R. Frongillo for discussions on algorithm development and M.-A. LeBlanc for sharing the polyprotein dataset.

Table 4.1: Performance metrics for each algorithm The Bhattacharya coefficient's complement (BCC) compares the degree of overlap between the human-annotated and algorithmically predicted 2D distribution of rupture force versus loading rate (e.g., Figure 4.10 *B*, Table 4.6). ΔZ_{95} is the metric for the upper bound of the fractional error in determining event location. The symbol (↓) indicates a lower value is better.

Name	BCC (↓)	ΔZ_{95} (↓)
FEATHER	**0.0037**	**0.0065**
OpenFovea	0.203	0.42
Scientific Python	0.030	0.19

4.9 Supporting Information

4.9.1 Algorithm Description

4.9.1.1 High-level description

FEATHER detects unbinding and unfolding events in single-molecule force spectroscopy (SMFS) records characterized by a sudden drop in force (F). FEATHER is based on a probabilistic model of a signal lacking any events, called the *no-event model*. FEATHER leverages information contained in a reference record containing no ruptures events, typically the approach curve

in atomic force microscopy (AFM) studies (Figure 4.7). The algorithm has the following 5 basic steps:

1. Estimate the no-event parameters from an approach curve (see Figure 4.7).

2. Fit the no-event model to a retraction curve.

3. Calculate the upper bound on the probability of each retract point using the Chebyshev's inequality [123] given the model.

4. Iteratively update the probability using additional characteristics of the data to remove false-positive events.

5. Report contiguous regions with probabilities lower than a user-specific threshold as events.

4.9.1.2 The no-event hypothesis

In SMFS, events occur when the force applied to a molecule exhibits a discontinuity as the molecular conformation passes over an energy barrier. FEATHER assumes that events take place on time scales much faster than the response time of the probe. If this is not true, the data are assumed smoothed until this condition is reached. The algorithm models the data assuming no event is occurring at a given time t and calculates the probability based on that assumption at each t. Contiguous regions of time with probabilities below a user-given threshold are grouped into a single event. Hereafter, the definition of an event and these assumptions will be referred to as the *no-event hypothesis*.

Importantly, FEATHER's model for experimental noise is independent of noise distribution, except for assuming a distribution with zero mean and median. By making such few assumptions about the data, FEATHER avoids the need for polymer-physics based models, such as the worm-like chain model [128], or other specialized knowledge of the system under study.

FEATHER applies this probabilistic model to the retraction portion of the force-extension curve. As the reference curve for no events, the algorithm uses an approach curve taken with the same individual cantilever to determine characteristics of the noise. FEATHER initially fits and subtracts a smoothing spline from the approach curve, yielding a reference mean and force variance of the residual's standard deviation within a window of 2τ, where τ is a user-specified fraction of the curve length. Applying this procedure to the retraction record yields a residual mean and standard deviation at each point in time. This residual is transformed into a probability using Chebyshev's inequality [123] and the reference mean and variance from the approach curve. This probability at each point in the retraction curve is iteratively updated to remove the effect of adhesion and other false positives, detailed below. As shown in Figure 4.2, the result is a probability at each time point which drops from one towards zero near events. A threshold probability is set by the user or optimized by a tuning routine (see Figure 4.7).

We define a single event as a contiguous region of time with probabilities below the threshold. The rupture force and loading rate are determined for each such region, as described in the "Data Acquisition and Annotation" section, below.

4.9.1.3 Calculating the no-event parameters:

FEATHER identifies events by focusing on short time scale events while not triggering on simple Brownian motion of the probe or variation in the compliance of the system. To suppress low-frequency fluctuations, we first fit the high-frequency data to a spline. The spline, denoted as S_t, was calculated by a least-squares fitting of a second-order basis spline [129] to the high-bandwidth force-vs.-time curve, F_t. The spline was second-order to ensure a continuous first derivative, a requirement of our no-event hypothesis. The spline knots were spaced uniformly at intervals of the user-specified τ. Figure 4.7 is a representative demonstration of the spline fitting. Determining S_t immediately yielded the force residual $r_t = F_t - S_t$. We note that r_t has essentially a zero mean and

median as required for FEATHER, but r_t was not necessarily Gaussian distributed. This flexibility to handle non-Gaussian distributed fluctuations motivated the use of Chebyshev's inequality [123].

Unfortunately, analysis based on the force residual r_t did not provide a conclusive signal for the presence of an event (see Figure 4.7). In order to improve event detection, we determined how variance of r_t changes in time since this metric was found to be highly sensitive to unfolding events but insensitive to local variation in the curvature of the data. To do so, we computed σ_r, which is defined as the standard deviation of r_t centered at t with a window of [—2τ,2τ]. As illustrated in Figure 4.7, using σ_r instead of r_t provided a much stronger signal of an event.

To be able to calculate the probability of an event in the retraction curve, we next calculated two additional metrics based on σ_r of the approach curve. Specifically, we calculated the median value and the standard deviation in σ_r, denoted as μ_σ and σ_σ, respectively. The median was used instead of the mean to remove the influence of possible false positive events in the approach that skew the mean but not the median. The removal of these pseudo-events was necessary to ensure accurate estimators for μ_σ and σ_σ, which were then used to calculate the probability of an event at time t using Chebyshev's inequality as follows:

$$P(\sigma_r) \leq \left(\frac{\sigma_\sigma}{\sigma_r - \mu_\sigma}\right)^2 \tag{4.1}$$

where this σ_r is from the retraction curve being analyzed. Although Equation 4.1 provides only an upper limit on the probability of no event, the integration of multiple aspects of the data—see Equation 4.2 below—leads to clear detection of events with high specificity (Figure 4.7 *G*).

In our application of FEATHER to AFM data, we used the approach curve immediately preceding the analyzed retraction curve. Both curves shared a common set of noise characteristics because they were taken at the same velocity. In principle, one could use a single common "reference" curve for a multitude of retraction records given that the reference curve had the noise

characteristics of the retraction curves. For instance, one could acquire a handful of approach curves at the retraction velocity for an individual cantilever and use those curves as the reference. In test cases, the velocity of the approach did not have to equal the velocity of the retraction but such applications should be tested on an individual basis, particularly if the ratio between the velocities is >5.

The quality of FEATHER's results were improved by multiplying the no-event probability, as defined in Equation 4.1, by the no-event probability of the integral force, force derivative, and force differential. The calculation of each of these probabilities was exactly the same as described above, with the variables changed appropriately. Specifically, the relevant operation (integration, differentiation, or force difference) was applied to the approach, estimates for the operation-specific μ_σ and σ_σ, were obtained, yielding the operation-specific probability. The local force derivative of the basis spline for the force was calculated in the standard, analytical manner, [129] and the local differential at each point was calculated centered about that point with a window size of $\tau/2$. More details for the calculation of each of these terms are given in the pseudocode listed in Table 4.5. In particular, the final probability is given in terms of these operation-specific probabilities as:

$$P_{noevent} = P_F \times F_{integral} \times P_{dF} \times P_{dF/dt} \tag{4.2}$$

where P_{F} is defined as Equation 4.1. Each term in the probability calculation improved the performance of $P_{\text{no event}}$. For example, incorporating P_{dF} made it less likely that cantilever oscillations after a rupture would trigger a spurious event. The force differential was used in addition to the force first derivative in order to incorporate higher-order derivative information. In addition, $P_{\text{no event}}$ is set to one if any of the individual distributions (P_{integral}, P_{dF}, or $P_{\mathrm{dF/dt}}$) are equal to one. This codifies the requirement that an unbinding or unfolding event is statistically distinguishable from the dynamics observed during an approach curve. In addition, AFM data has a region at the start of each retraction curve in which the cantilever is in contact with the surface.

To prevent this so-called 'touchoff' region from triggering spurious events, FEATHER ignores any event starting at the beginning of the retraction curve. Further, minor details are listed in the pseudocode of Table 4.5.

4.9.1.4 Algorithm runtime

All timing and tuning results were obtained using a desktop with 32 GB of RAM, an AMD Ryzen 5 1500X Quad-Core CPU, and a 500 GB hard drive. Figure 4.4 compares the runtime of FEATHER and the reference algorithms. The runtime of FEATHER, denoted $T(N)$ in the computer science literature, is linear with number of points but with an offset. As a result, a 1,000-fold increase in the number of data points in a curve leads to a 20-fold increase in runtime over the range tested (Figure 4.4). FEATHER has a roughly tenfold better runtime performance on larger datasets than the OpenFOVEA or Scientific Python algorithms, in addition to outperforming them in application-specific metrics (see Figure 4.3).

4.9.1.5 Algorithm tuning

All three algorithms were tuned using 5-fold cross validation. Cross validation is a common technique for quantifying performance of an algorithm [130]. In our case, the data were split with 80% of the data as a training set for parameter optimization and 20% of the data as a validation set for measuring algorithm performance. Cross validation was performed five times at fifteen different values over the useful range of each algorithms tuning parameter (Figure 4.8). The parameter value that minimized the Bhattacharya coefficient's complement for an algorithm was considered the algorithm's best parameter. Data shown in Figures 4.10–4.11 consist of the concatenation of the five validation folds for each algorithm's best parameter.

Since tuning the reference algorithms (Open Fovea and Scientific Python) on the full DNA

dataset would have required many cpu-months (compared to about one cpu-day for FEATHER, see Figure 4.4), a smaller subset of the DNA data was used for comparing the algorithms. In particular, the subset of the DNA data with the smallest number of points per curve—200 curves with v = 1,000 nm/s, $N_{\text{points}} \sim 10^5$ (see Table 4.3)—was used for results comparing FEATHER to the baselines for Figure 4.10. FEATHER was also tuned separately on the larger, more complex DNA dataset, with similar results to those reported in the rest of the paper (Figure 4.11). This demonstrates that FEATHER generalizes well to a wide range of data sets sizes and experimental parameters. We note that on the DNA data set, FEATHER showed even greater performance gains than for the polyprotein data set.

4.9.2 Sample Preparation

Site-specific coupling improves the rate and quality of the resulting single-molecule force spectroscopy (SMFS) data. We used a recently developed site-specific coupling chemistry for both the polyprotein and DNA studies [69]. Here, we briefly review this procedure for surface- and cantilever-functionalization.

4.9.2.1 Azide-Functionalized Surfaces

Glass coverslips [12-mm diameter (Ted Pella, 26023)] were cleaned by sonicating for 5 min in acetone, 5 min in 95% ethanol, and finally immersed for 3 min in a solution of potassium hydroxide [80 g of KOH (Fisher, P250-500) dissolved in 170 mL of 95% ethanol and 80 mL of ultrapure water (18.2 MΩ)]. We next serially washed the coverslips in two 1-L beakers of ultrapure water. The cleaned coverslips were dried with 99.8% pure dry nitrogen gas and stored at room temperature in

a dust-proof container.

Prior to azide-functionalization of the coverslips, we first exposed them to 30 min of UV-ozone (Novascan, PSDP Digital UV Ozone System). We next loaded the coverslips into a custom-made Teflon-holder and immersed them in 0.15 mg/mL of silane-PEG-azide (Silane-PEG-Azide Nanocs PG2-AZSL-600) dissolved in warm (60 °C) toluene (Sigma 179418-4L) for 3 h. To achieve uniform surface coverage, this solution was stirred at 600 RPM. After this incubation, we serially rinsed the coverslips in 250-mL beakers of toluene, isopropanol, and ultrapure water. The resulting azide-functionalized surfaces were dried with nitrogen gas and stored in a dust-proof container at 4 °C.

4.9.2.2 Streptavidin-Coated Cantilevers

We used a similar protocol to coat the cantilevers with streptavidin. We first removed the gold and underlying chromium layer off of long, soft cantilevers [L = 100 μm; k = 7 pN/nm (nominal) (Olympus)], which achieves sub-pN force stability over 100 s [131]. To remove the gold, we immersed the cantilever for 30 s in 10 mL of gold etchant (Transene TFA) followed a rinse in 250 mL of ultrapure water. The chrome was removed by immersing the cantilever in 10 mL of chromium etchant (Transene 1020) followed by a rinse in 250 mL of ultrapure water. The cantilevers were then serially rinsed for 30 s in 50 mL of deionized water, isopropanol, toluene, isopropanol, and ultrapure water. After drying with a Kimwipe, we then exposed the cantilevers to UV-ozone for 30 min. Akin to the coverslips, we then maleimide-functionalized the coverslips by immersing them for 3 h in a 0.15 mg/mL solution silane-PEG-maleimide (Nanocs PG2-MLSL-600) dissolved in warm toluene. The resulting functionalized cantilevers were serially rinsed in 250 mL of toluene, isopropanol, and ultrapure water. The cantilevers were immediately dried by touching the base of the cantilever to a Kimwipe. To coat the cantilevers with streptavidin, we next immersed them for 3 h at room temperature in a 0.2 mg/mL solution of thiol-derivatized streptavidin (Protein Mods, SAVT) dissolved in PBS buffer [10 mM phosphate buffer (pH 6.75), 140 mM NaCl, 3 mM KCl]

with 1 mM TCEP (Tris(2-carboxyethyl)phosphine, Thermo Scientific 77720)] in small wafer holders (Entegris, H22-100/101-0615). Subsequently, we transferred the cantilevers into these holders to 4 °C for an overnight incubation. After this incubation, we removed the free streptavidin by serially rinsing the cantilevers in two 10-mL beakers of PBS at pH 7.4 and then immersed them in a 20-mL petri dish filled with PBS for 10 min. The resulting streptavidin-coated cantilevers were stored in 50 µl of PBS at pH 7.4 and 4 °C in the wafer holders until loading into the atomic force microscope (AFM). Streptavidin-coated cantilevers were typically stable for 1–2 weeks of storage at 4 °C.

4.9.2.3 Polyprotein Labelling

As previously described [69], the polyprotein used was created by inserting the 73 amino acid protein α_3D [132] into a plasmid with four copies of the 57 amino acid protein NuG2 [133]. The plasmid is available via the Addgene nonprofit plasmid repository (Plamid ID 80163).

The protocol for labeling the polyprotein was recently published [69]. Briefly, after overexpression in *E. Coli* strain BL-21 (DE3), the protein was purified on a Ni-NTA (Qiagen) column equilibrated with TBS buffer [25 mM Tris (pH 8.0), 150 mM NaCl, 5 mM beta mercapoethanol (βME)]. To convert the cysteine in the aldehyde tags (LCTPSR) to formylglycine (an amino acid containing an aldehyde), purified formylglycine-generating enzyme (FGE) was added to purified polyprotein containing the aldehyde tag in 25 mM triethanolamine (pH 9.0), 50 mM NaCl, 1 mM βME in a 1:10 FGE:polyprotein molar ratio. The mixture was incubated overnight at 18 °C with shaking, resulting in ~95% conversion from cysteine to formylglycine. After aldehyde conversion, the sample was buffer exchanged into 50 mM sodium phosphate (pH 6.0), 150 mM NaCl, 1 mM TCEP (Tris(2-carboxyethyl)phosphine) and incubated for 3 days at 37 °C with 10x molar concentration of Hydrazino-Pictet Spengler (HIPS) reagents to functionalize the protein with dibenzocyclooctyne (DBCO) and biotin. Details of HIPS reagent synthesis were also previously published [69]. As both ends of the polyprotein contained the same aldehyde, at best 50% of the

protein would contain both biotin and DBCO. Despite this limitation, only proteins which were differentially labeled with both DBCO and biotin at each end were efficiently stretched between azide-functionalized surfaces and streptavidin-coated AFM tips.

4.9.2.4 DNA Sample Preparation

For the DNA pulling assays, we used 650-nm long DNA labeled at one end with four biotins and the other end with dibenzocyclooctyl (DBCO), a copper-free click chemistry reagent that reacts with azide moieties. To introduce these labels, we used PCR and a forward and reverse primers (IDT) labeled at their 5' ends (Table 4.3). The template DNA was the M13mp18 plasmid (New England BioLabs N4018S). After PCR, we purified the DNA to remove the primers using a QiaQuick PCR purification kit (Qiagen 28106) followed by gel electrophoresis. The desired band was excised with a razor blade and the DNA extracted using a Freeze 'N Squeeze DNA Gel spin column (Bio-Rad). We then concentrated the DNA using a 0.5-mL microconcentrator (Amicon 10K centrifugal filter) and removed residual agarose using a second Qiaquick PCR purification. The DNA was eluted using TE [10 mM Tris-HCl (pH 8.0), 1 mM EDTA] and stored at 4 °C. We prepared DNA samples for the AFM by depositing 100 μL of the 8 nM labeled DNA onto azide-functionalized coverslips and let the DNA incubate at 4 °C overnight in a wafer holder. The coverslips were then rinsed with 7 mL of TE at pH 8.0 and 7 mL of PBS at pH 7.4 and 1 mM EDTA and stored at 4 °C.

4.9.3 Data Acquisition and Annotation

4.9.3.1 AFM Experiments

The force spectroscopy data was acquired on a Cypher ES AFM (Asylum Research). The samples were in liquid [PBS (pH 7.4)] and held at a constant temperature (25 °C) using a temperature-

controlled, closed-fluidic liquid chamber. The stiffness of each cantilever was calibrated using the standard thermal method [134], as implemented on our commercial AFM. Sensitivity of the detector (V/nm) was determined by pushing the tip into the sample and fitting the resulting force-extension curve. After calibration, the sample was repeatedly probed at various locations and retraction velocities (v) using a standard constant-velocity data-acquisition scheme. For example, within one cycle, we lowered the tip towards the surface at constant velocity until a user-defined force was achieved, typically 100 pN. The tip was held in contact at constant F for ~1–2 s and then retracted at constant velocity while the cantilever deflection was digitized at 50 kHz. The experimental data sets used for this study consisted of 152 force-extension curves of the polyprotein construct acquired at four retraction velocities (200, 400, 1,800, and 3,800 nm/s) and 600 DNA force-extension curves in total acquired in equal number at three retraction velocities (100, 500, and 1,000 nm/s).

4.9.3.2 Polyprotein and DNA manual annotation

The start and end of each event in a curve were obtained through manual annotation as follows. We first smoothed the data with a 2^{nd}-order Savistky-Golay filter, where the filter length was set to 0.1% of the retraction curve length. The start and end of each event was manually identified in each smoothed force-extension curve. The loading rate was determined by a linear fit to the previous N points of force-vs.-time trace, where N was set to 2% of the curve length, The rupture force was determined as the last time the high-bandwidth data crossed the line defined by the linear fit. We note that this algorithm for determining loading rate and rupture force was also applied to the computationally defined events by all three algorithms (FEATHER, OpenFovea, Scientific Python). On average, each manual annotation of a curve took 1–2 min. More statistical information on the polyprotein data, including curve lengths and number of events per curve, is given in Table 4.2. The equivalent table for the DNA dataset is given in Table 4.4.

4.9.4 Simulation

Simulations were performed in order to test for a wider range of parameters (*e.g.* contour length changes), pathological examples such as high-force ruptures followed by lower-force 'shielded' ruptures, and to complement the manually annotated experimental data with an unambiguous 'ground truth'. Simulated data were generated and analyzed using an algorithm inspired by the recent work of Hummer and Szabo [39]. For a single simulated curve, the simulation consisted of the following distinct states:

1. State 1: Probe equilibration.

2. States 2-7: Pulling, including 6 different rupture events.

3. State 8: Probe retraction after final event.

In total, 100 simulated curves were used, with 6 events per curve. The probe position z was increased at a constant velocity v starting from 150 nm and moving to a curve-dependent final position, as described below. The molecular extension $q_{\mathrm{n+1}}$ and force $F_{\mathrm{n+1}}k$ $(z_{\mathrm{n+1}} - q_{\mathrm{n+1}})$ was determined from the previous extension, q_{n}, by the following relation:

$$q_{n+1} = q_n - D_q \delta t (\frac{\partial V}{\partial q_n})_i + g_n \sqrt{2 D_q \delta t} \tag{4.3}$$

where the parameters definitions and values for Equation 4.3 are given in Table 4.9. The initial extension before equilibration, q_0, was assumed to be 150 nm.

A wide range of contour length changes, loading rates, and pathologically complex force-extension curves were created by varying the worm-like chain force, $F_{\mathrm{WLC,i}}(q_{\mathrm{n}})$. Our simulations modelled the worm-like chain force as a modified Marko-Siggia worm-like chain (WLC) [135] determined by the particular state i. The last state after the final rupture (*i.e.*, state 8) has $F_{\mathrm{WLC},i} = 0$,

since no molecule is attached in that state. All other states share the following parameters: a persistence length p of 0.3 nm, a Boltzmann energy $k_{\mathrm{B}}T$ of 4.1 pN nm, and a stretching modulus of 100 pN. In order to achieve a wide range of rupture forces, loading rates, and changes in contour lengths, the contour length, $L_{0,\mathrm{i}}$, and the total distance spent in a state before rupture, Δz_{i}, were varied uniformly at random within the ranges in Table 4.8. The simulated data were analyzed in the same manner as the experimental data, with unambiguously identified events marked at transitions between adjacent, non-equilibration states. The last 10% of each simulated curve was used as an effective "approach" input to FEATHER, since no events were present after the final rupture. For the simulated data, FEATHER used a fractional τ of 0.001 (~10 ms) and a threshold of 10^{-5}.

FEATHER's performance on the simulated data exceeds its performance on experimental data. As shown in Figure 4.12 and Table 4.7, all performance metrics on simulated data are improved compared to the results presented in the rest of the paper (*e.g.* Figure 4.3, Table 4.1).

4.9.5 Figures

Figure 4.4: Runtime of each algorithm. (A) The runtime, denoted T(N), per curve versus number of points N in the analyzed record for each algorithm. (B) For each algorithm, the number of points analyzed per second was determine by fitting a line to the data in panel A.

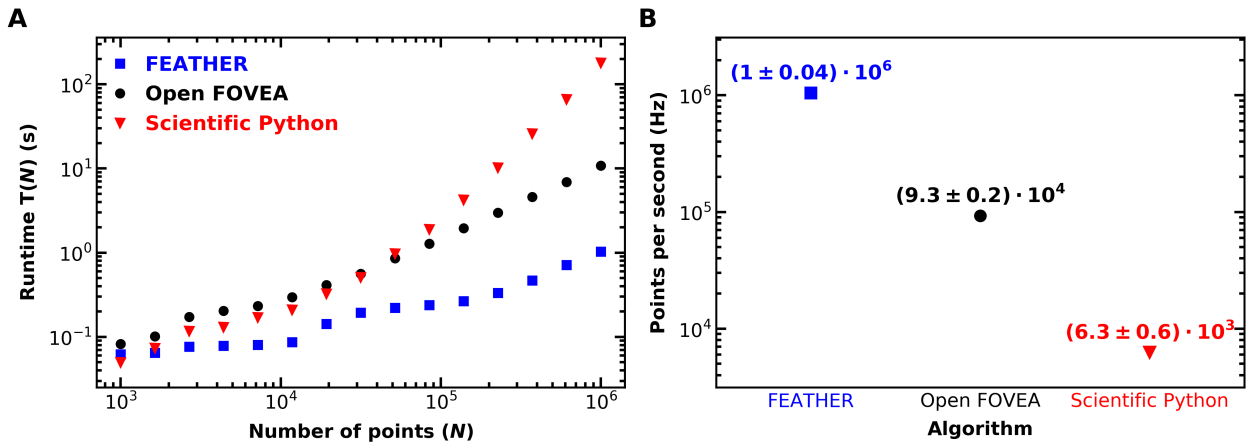

Figure 4.5: Representative examples of 650-nm DNA force-extension curves with one event (A–C), two events (D), and three events (E). Plotting conventions are as in Figure 4.1 and the scale from panel A is used in all 5 panels.

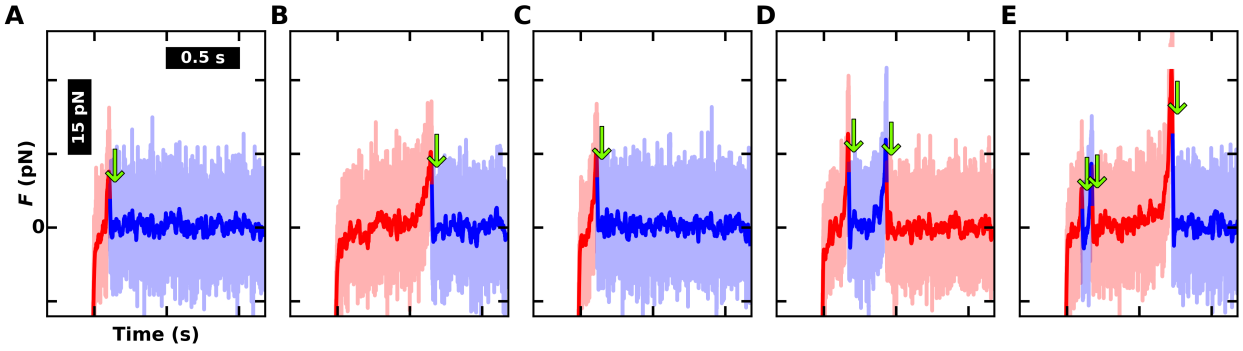

Figure 4.6: Effect of smoothing on BCC. (Left) Force-extension curves at three smoothing τ, formatted as in Fig 1. Note the low-force rupture in the middle panel is real. All curves are simulated data, as described in the Supporting Material. (Right) The BCC for all simulated data as a function of τ.

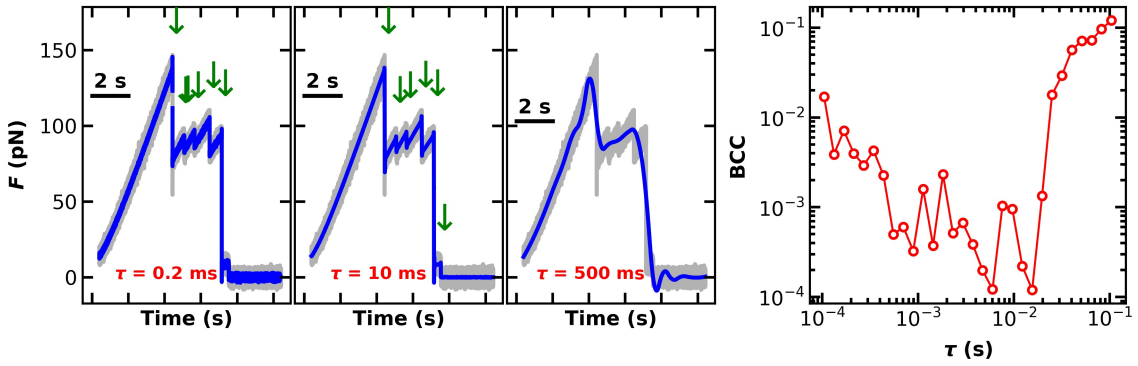

Figure 4.7: Overview of the FEATHER algorithm. (A, B) The approach and retract forces-vs-time at 25 kHz fit with a spline with knots spaced every 500 ms (τ), for a particularly low v (100 nm/s) and extended retraction distance (1.2 µm). (C,D) The force-residuals-vs-time of the approach and retract records after subtracting the spline from the high-bandwidth data. The subtraction yields a force residual r(t) with a zero-centered mean and variance about that mean (which contained mostly the thermal noise of the system within a window of 2τ). (E,F) The variance (σ_r) of the force residual as a function of time where σ_r is the standard deviation of the high-bandwidth data within a time window 2τ. The mean value of this variance (μ_σ) and the standard deviation (σ_σ) of it are also plotted. The cyan shaded region in each plot is derived from panel E. (G) The probability of no event at each time has a sharp minima near the expected event location based on the application of Chebyshev's inequality [123]. Changes in color of the retraction curved indicates an event, based on human-annotated data.

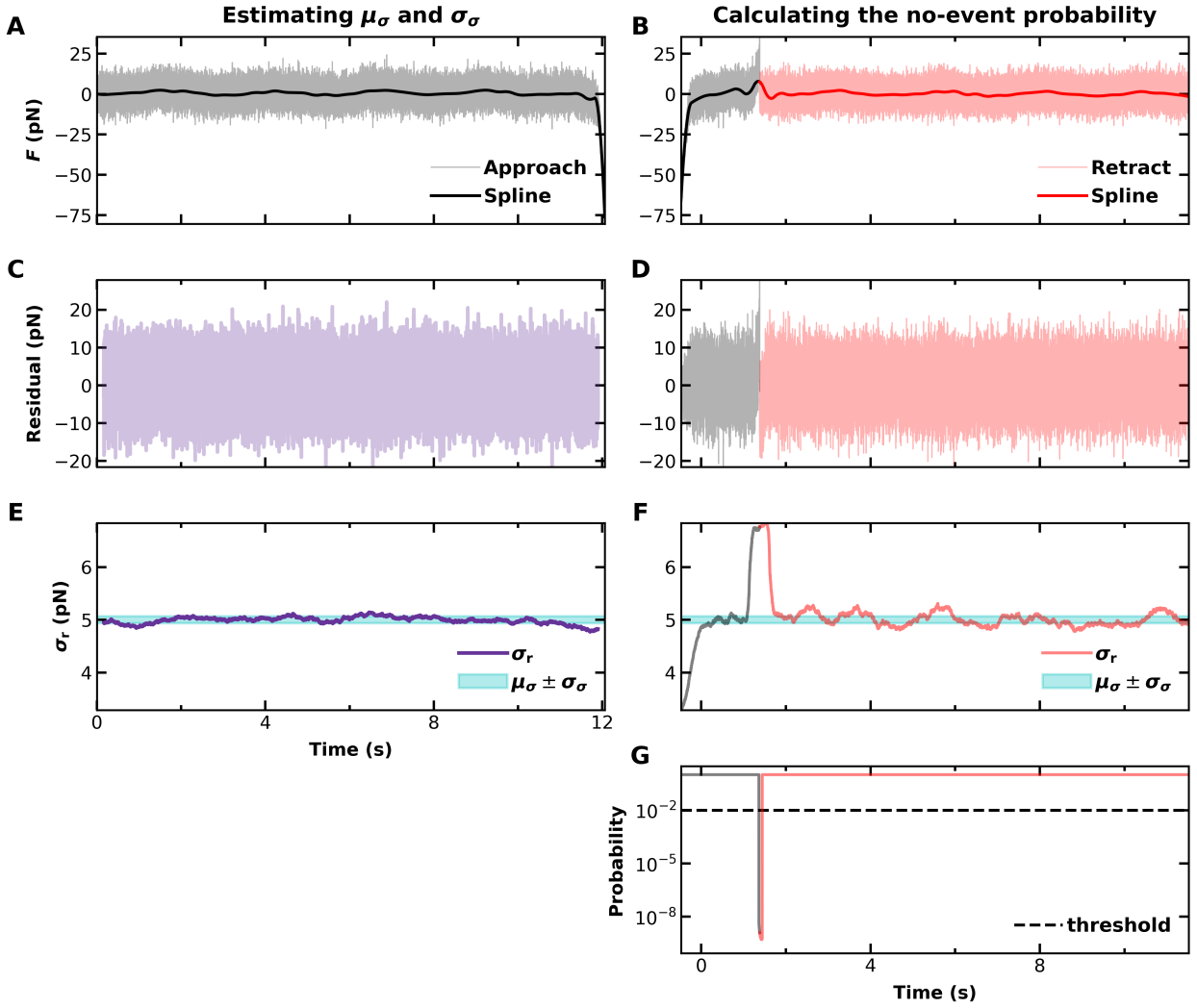

Figure 4.8: The sensitivity of the Bhattacharya coefficient's complement (BCC) The sensitivity of the Bhattacharya coefficient's complement (BCC), a measure of how well the algorithmically predicted events match human-annotated data, as a function of algorithm specific parameters for the three compared algorithms FEATHER (A), OpenFovea (B), and Scientific Python (C). Lower BCC is better. The BCC was computed from the polyprotein data set and the resulting distributions shown in Figure 4.3 *B–C*.

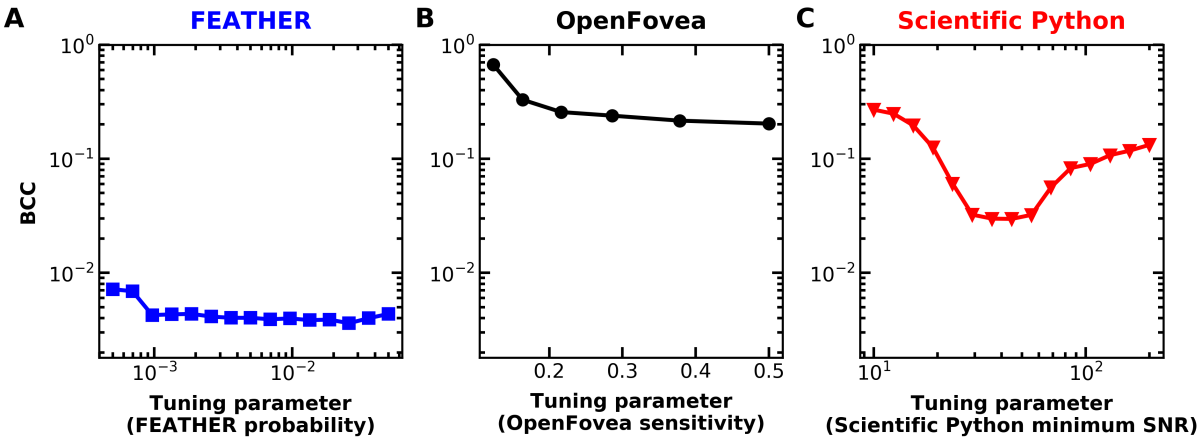

Figure 4.9: Additional metrics for comparing algorithm performance between FEATHER, OpenFovea, and Scientific Python. The metrics are precision (A), recall (B), and the false positive ratio (C). Precision is defined as the number of correctly predicted events (TP) in a data set divided by the total number of predicted events, TP/(TP+FP), where FP is the number of false positives. Recall is defined (TP/(TP+FN)) where FN is the number of missed events or false negatives. For both these metrics, better performance is indicated as closer to 1. The false positive ratio is defined as (FP/P) where FP is the number of false positives in a data set and P is the number of true events as defined by human annotation. Perfect recall would also yield a value of 1 because there were no missed events. In contrast the metric FP/P is better when closest to 0. It is important to note that these simple metrics ignore how close a predicted event is to a true event. Hence, while the wavelet transform has a similar Precision and Recall to FEATHER, FEATHER does much better for more experimentally relevant metrics (see Figure 4.3). The most common cause of false positives for FEATHER is false triggering on instrumental artifacts after tip detachment at high pulling velocities (Figure 4.13). FEATHER most often returns a false negative when attempting to detect a short-lived, transiently-occupied state. Applications of recently developed cantilevers [126] with improved temporal resolution and higher force precision as well as optimizing τ for different v should mitigate these issues. (D) A confusion matrix for FEATHER, where the rows are the human-annotated assignment of events and non-events, and the columns are predicted by FEATHER. (E–F) Formatted as panel (D), but applied to OpenFovea and Scientific Python, respectively.

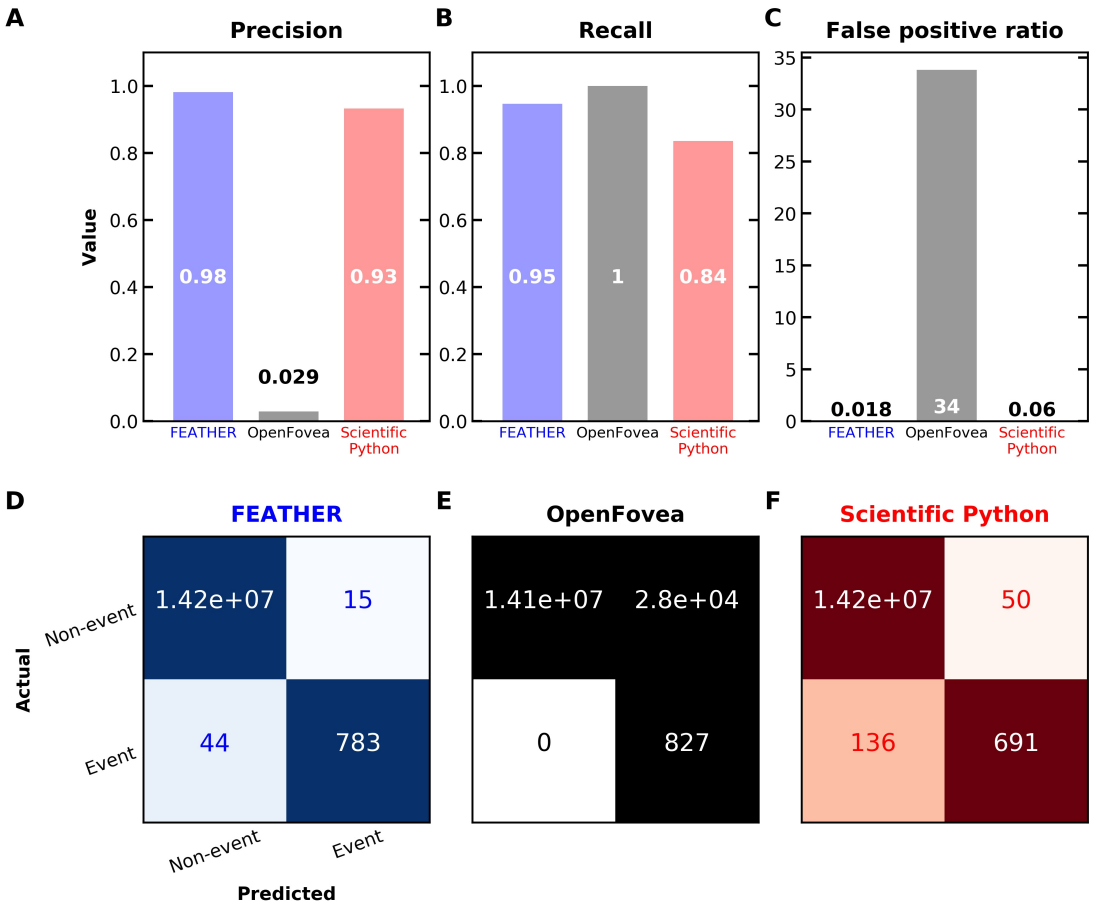

Figure 4.10: FEATHER outperforms the reference algorithms in analyzing a 650-nm DNA dataset acquired at a high-retraction velocity (1,000 nm/s). (A) Histograms of relative errors between human-annotated and FEATHER's algorithmically predicted event where ΔZ is the fractional distance between the identified events divided by the full range of the record, $\mathbf{d}_{t\to p}$ is the distance from a true event to the closest predicted event, and $\mathbf{d}_{p\to t}$ is the distance from an algorithmically predicted event to the closest true event. (B) FEATHER's 2D distribution of true and predicted rupture forces and loading rates. (C,D) The histograms of rupture forces and loading rates from the data in panel B. (E) FEATHER's performance metrics using Bhattacharya coefficient's complement (BCC), which measure the overlap between 2 distributions and ΔZ_{95}, location of the 95$^{\text{th}}$ percentile of the combined distribution for $\mathbf{d}_{p\to t}$ and $\mathbf{d}_{t\to p}$. Ideally, both metrics should 0. (F–J) OpenFovea's and (K–O) Scientific Pythons's performance using the same analysis as in panels A–E. In the scatter plots (B,G, L), the density of green true points obscures overlap with the predicted points.

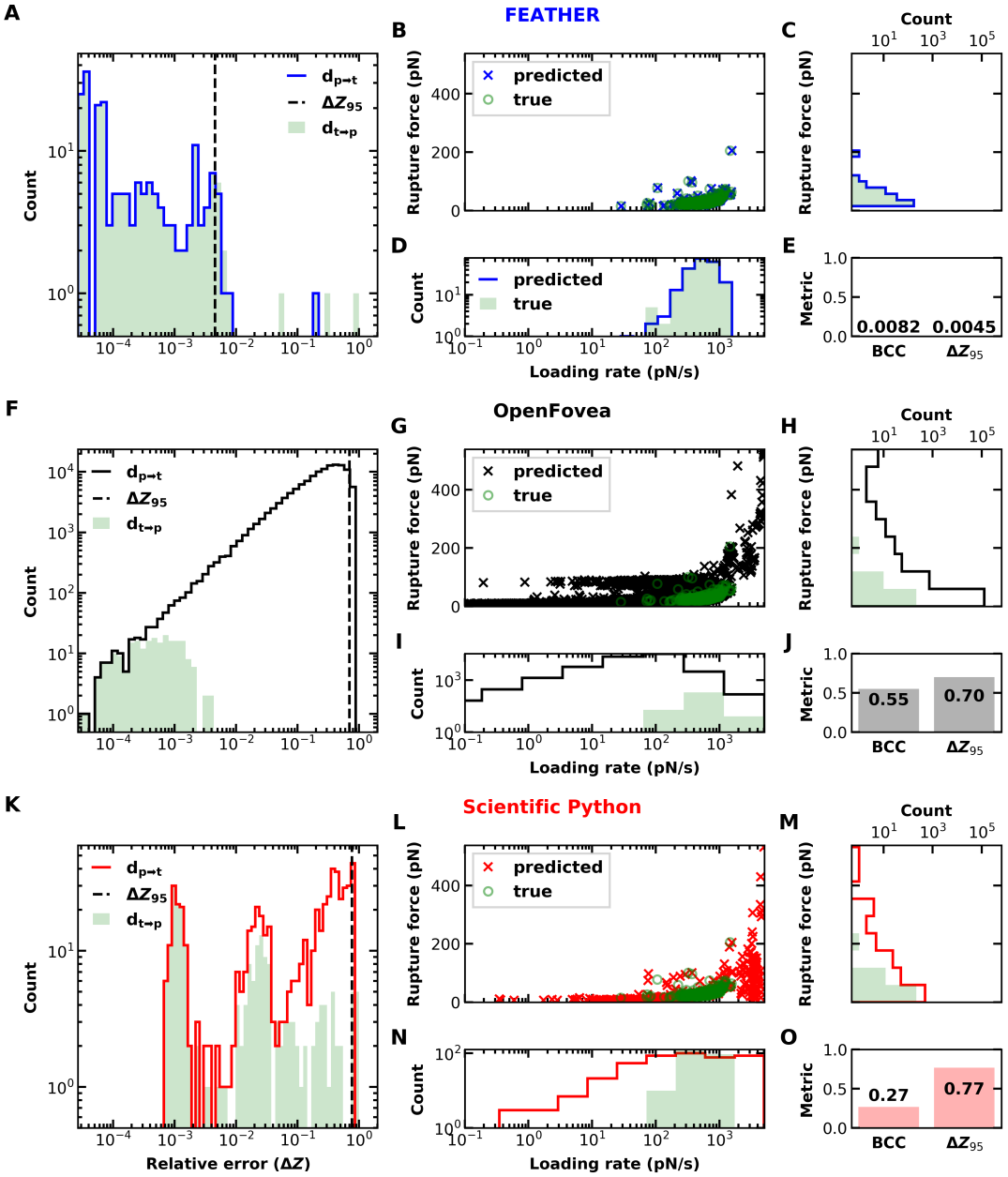

Figure 4.11: FEATHER generalizes well to force spectroscopy of 650-nm DNA data set containing multiple attachments over three different retraction velocities (100, 500, and 1,000 nm/s). The subplots in this Figure are formatted as in Figure 4.10 but with FEATHER applied to the full data set, spanning an order of magnitude in velocities and two orders of magnitude in loading rates.

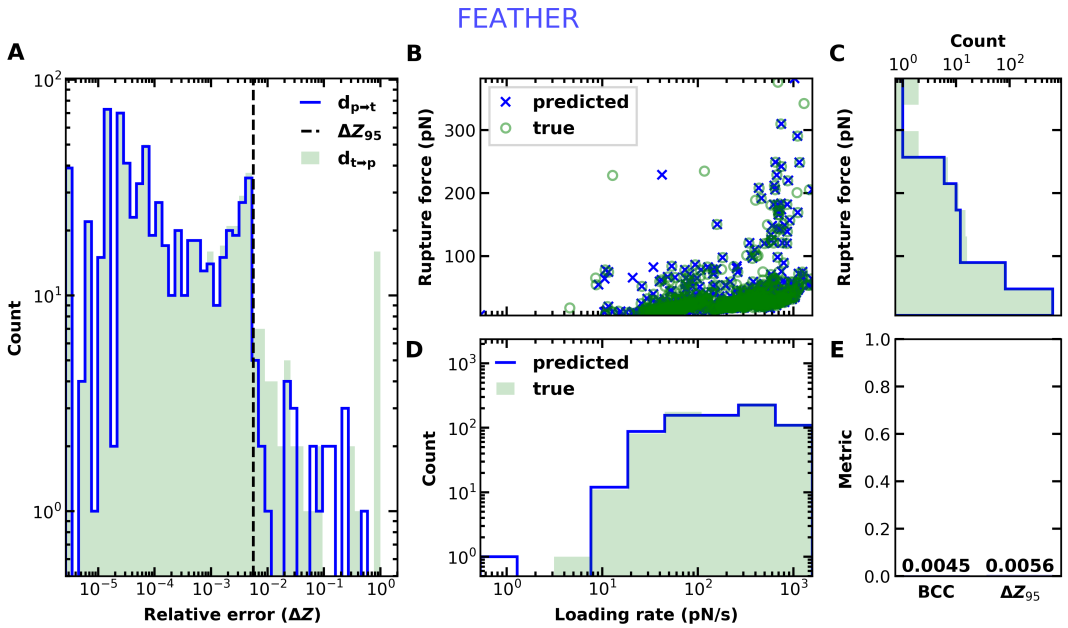

Figure 4.12: FEATHER generalizes well to a wide range of simulated data. (A) An example force-extension curve, generated as described in the Supporting Material. The color-coded regions denote a high-force rupture (blue), several ruptures with small changes in contour lengths (red), and a final lower-force rupture (green). (B) A histogram of contour lengths from all regions in all simulated force-extension curves. (C). As panel B, but for contour length changes between adjacent regions. (D–F) Formatted as Figure 4.3 in the main text, but showing FEATHER's performance on the simulated data.

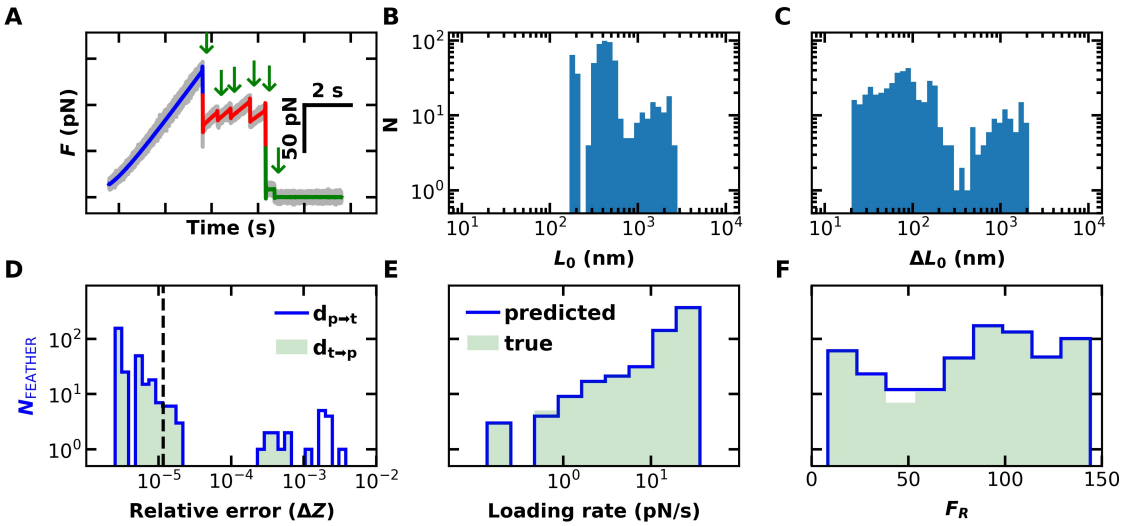

Figure 4.13: Typical failure mode for FEATHER. (A) A force-versus-time trace, formatted as Figure 4.1, where FEATHER's predictions are consistent with the human-annotated data. (B) A trace, formatted as in panel A, where two spurious events are detected in the last half of the data. Note that the data in panel B is at a 5-fold higher velocity (1.8 µm/s) than panel A (0.4 µm/s), introducing additional noise and less averaging of Brownian motion since the fractional number of spline points per record is fixed, not the degree of smoothing per unit time.

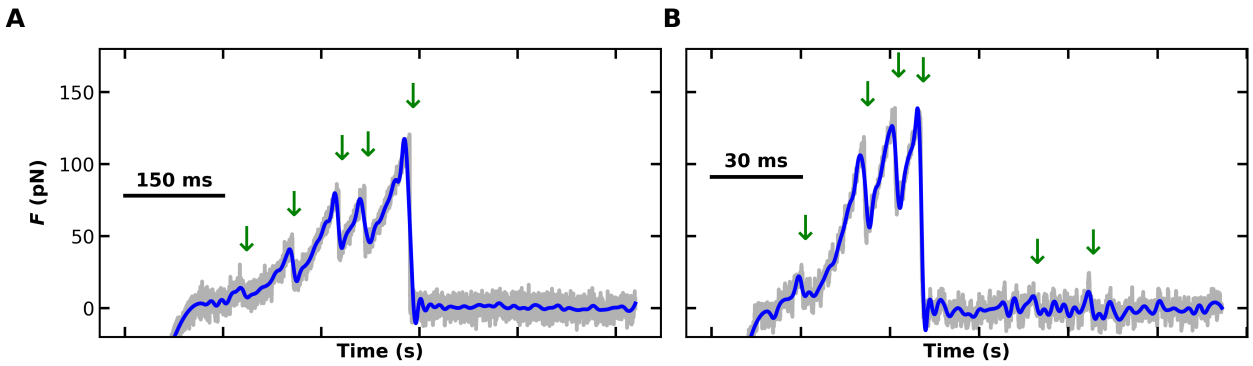

4.9.6 Tables

Table 4.2: Statistical information on the polyprotein data set. For each loading rate v in the data set, this table lists the number of curves N_{curves}; mean number of points in a curve, $\boldsymbol{N_{\text{points}}}$; the number of curves with 'x' events $\mathbf{N_{e=}}_x$ for x=[1,2,3]; and the number of curves with greater than 3 events, $N_{\text{e}>3}$.

$\boldsymbol{v}$ **(nm/s)**	$\boldsymbol{N_{\text{curves}}}$	$\boldsymbol{N_{\text{points}}}$ **(10^3)**	$\mathbf{N_{e=3}}$	$\mathbf{N_{e=4}}$	$\mathbf{N_{e=5}}$	$\mathbf{N_{e=6}}$	$\mathbf{N_{e>6}}$
3800	25	62	1	5	6	12	1
1800	54	77	2	8	9	31	4
400	71	113	0	9	28	27	7
200	2	200	0	1	0	1	0

Table 4.3: Primers sequences The forward and reverse primers amplify a 647-nm piece of DNA, from positions 1607 to 3520 on the M13mp18 plasmid, as discussed in the text. Unmodified DNA bases are lowercase. The uppercase letters 'T','B', and 'D' respectively represent biotinylated Thymidine residues, a terminal Biotin separated from the sequence by triethyleneglycol spacer, and a terminal dibenzocyclooctyl (DBCO) separated from the sequence by triethyleneglycol spacer.

Name	**Sequence**
Forward primer	Dagttgttcctttctattctcactccgc
Reverse primer	BtcaataaTcggctgtctTtccttatcaTtc

Table 4.4: Statistical information on the 650-nm DNA data set. Conventions are as in Table 4.2.

v **(nm/s)**	$N_{\mathbf{curves}}$	$N_{\mathbf{points}}$ (10^3)	$\mathbf{N_{e=1}}$	$\mathbf{N_{e=2}}$	$\mathbf{N_{e=3}}$	$\mathbf{N_{e>3}}$
1000	200	117	173	26	1	0
500	200	200	130	49	9	12
100	200	671	155	35	6	4

Table 4.5: Pseudocode for FEATHER Psuedocode for FEATHER. Comments given by #.

def **predict_events** (approach, retraction,threshold, τ):
$\mathbf{g}^*$ = second-order spline fit to retraction using τ for knots
$\mathbf{g}_a$ = second order spline fit to approach using τ for knots
dt = spacing between adjacent time points
r = retraction – $\mathbf{g}^*$
ra = approach – $\mathbf{g}_a$
s[**i**] = standard deviation of r[**i**- 2τ:**i**+ 2τ]
s_a[**i**] = standard deviation of ra[**i**- 2τ:**i**+ 2τ]
 # Determine the no-event probability
ϵ = median of s_a
σ = standard deviation of s_a
k = (s- ϵ)/ σ
probability = minimum(1,k^{-2})
 # Determine the integral probability
integrateds[**i**] = integrate (s-ϵ) from [**i**- 2τ] to [**i**+ 2τ]
set integrateds where positive to σ
k_{integ} = (integrateds/ σ)
probability = probability * minimum of (1, k_{integ}^{-2})
 # Determine the derivative probability
$\mathbf{g}_{\text{deriv}}$ = derivative of $\mathbf{g}_a$
ϵ_d = median of derivative of $\mathbf{g}_a$
σ_d = standard deviation of derivative of $\mathbf{g}_a$
$\mathbf{g}^*_{\text{deriv}}$ = derivative of $\mathbf{g}^*$ with respect to time
$\boldsymbol{k}_{\text{deriv}}$ = ($\mathbf{g}^*_{\text{deriv}}$ - ϵ_d)/ σ_d
probability = probability * minimum of (1,k_{deriv}^{-2})
 # Determine differential probability
$\mathbf{g}_{df}$ = change of $\mathbf{g}_a$ with respect to time in steps of $\tau/2$
$\mathbf{g}^*_{df}$ = change of $\mathbf{g}^*$ with respect to time in steps of $\tau/2$
σ_{df} = standard deviation of $\mathbf{g}_{df}$
ϵ_d = median of $\mathbf{g}_{df}$
k_{df} = ($\mathbf{g}^*_{df}$ - ϵ_{df})/ σ_{df}
probability = probability * minimum of (1, k_{df}^{-2})
 # find the initial guess for events
events = indices where probability <= threshold
combine event indices within $\tau/4$ of each other
 # update the events to remove adhesions
$z_{\text{approach,surface}}$ = last point where approach force > 0
$z_{\text{retraction, surface}}$ = where retract $z_{\text{retraction}}$ crosses approach $z_{\text{approach,surface}}$
$z_{\text{retraction, surface}}$ = maximum of ($z_{\text{retraction, surface}}$, first time k_{deriv}=1)
remove events containing $z_{\text{retraction, surface}}$
re-zero retract force to median of all points after last event
update all fits to the retraction and probabilities to where $z_{\text{retraction}} \geq \mathbf{z}_{\text{retraction, surface}}$
 # update the events to remove stretching and low-force noise
remove with positive derivatives and re-zero force as above
remove where $\mathbf{g}^*$- $\mathbf{g}^*_{df} \leq (\epsilon_{df}+\sigma_{df})$ or where $\mathbf{g}^*+(\mathbf{g}^*_{\text{deriv}} \cdot \tau/4 \cdot \mathbf{dt}) < \sigma_{df}$
re-zero force as above
remove where the average F with a window size of 2τ is less than $\sigma + \epsilon + \sigma_{df}$
remove where the average F difference with a step size of 2τ is greater than -($\sigma + \sigma_{df}$)
remove events within $\tau/4$ of the boundaries
return events

Table 4.6: Variable and performance metric definitions. BCC stands for Bhattacharya coefficient's complement. Throughout, 'k' refers to the index of a force-extension curve, and 'i' and 'j' refer to either true or predicted. For example, $d_{t\rightarrow p,\mathbf{4}}$ represents the distances from the true to the predicted events in force-extension curve four.

Name	**Notation or definition**	**Range**	**Optimum**
K	Number of curves	—	—
N_k	Number of points in force-extension curve k	—	—
$d_{i\rightarrow p}$	Distribution of pointwise distances in 'k' from 'i' ruptures to the closest 'j' rupture or N_k if none, where i and j are true (t) or predicted (p)	—	—
ΔZ_x	the 'x'-th % of concatenated $\frac{1}{N_k} d_{t\rightarrow p,k}$ and $\frac{1}{d_{p\rightarrow t,k}}$ k	—	—
ν_i	histogram of 'i' loading rates over all k	—	—
F_i	histogram of 'i' rupture forces over all k	—	—
$d_{(\nu,F),i}$	joint histogram of ν_i and F_i divided by K	—	—
relative error	ΔZ_{95}	[0,1]	0
rupture BCC	1 - $< d^{\frac{1}{2}}_{(\nu,F),t} \vert d^{\frac{1}{2}}_{(\nu,F),p}$	[0,1]	0

Table 4.7: Table Title The Bhattacharya coefficient's complement (BCC) and ΔZ_{95} for FEATHER, as applied to the simulated data. FEATHER's performance on simulated data is more than an order of magnitude improved over the experimental results shown in Table 4.1. The symbol (↓) indicates a lower value is better.

Name	BCC (↓)	ΔZ_{95} (↓)
FEATHER	**0.00014**	**0.000012**

Table 4.8: Parameters for simulated force-extension curves. This table lists the parameters used for simulating $F_{\mathrm{WLC,i}}(q_\mathrm{n})$. A sample from the uniform distribution between numbers x_0 and x_f is denoted as Unif (x_0, x_f), $L_{0,\mathrm{i}}$ is the contour length in state i, F_R is the mean rupture force, and Δz_i is the total pulling distance spent in state i. Note that Δz_i is proportional to time and to the number of simulated points spent in a state, since the velocity, v, and sampling rate, Δt, are constant.

State i	$\boldsymbol{L_{0,\mathrm{i}}}$	$\Delta \boldsymbol{z_\mathrm{i}}$	$\boldsymbol{F_\mathrm{R}}$ **(pN)**
1	220 nm – 20 Unif[1,2]	2000 points (60 ms)	NA
2	$L_{0,i\text{-}1}$	50 * Unif (1,3)	138
3-6	$L_{0,i\text{-}1}$ + 20 Unif[1,3]		98
7	$L_{0,i\text{-}1}$ + 20 Unif[10,100]		25
8	N/A, F_{WLC}=0	250 Unif[1,2]	NA

Table 4.9: Definition and values of physical parameters used in Equation 4.3. Definition and values of physical parameters used in Equation 4.3.

Parameter	**Description**	**Value used**
D_q	Probe diffusion coefficient	250 nm^2/ms
Δt	Time step	30 µs
g_n	Noise source	Random numbers from a unit Gaussian dist.
i	Simulation state index	0 (equilibration) to 8 (after final detachment).
k	Probe stiffness	0.5 pN/nm
R	Loading rate	25 pN/s
v	Probe velocity	R/k = 50 nm/s, except state 0 (v=0)
$\frac{\partial V}{\partial q_n}_i$	State-dependent force	k (q_n – z_n) + $F_{\mathrm{WLC},i}(q_\mathrm{n})$, where $F_{\mathrm{WLC},i}$ is determined as described in the text

Chapter 5

Improved free-energy landscape reconstruction of bacteriorhodopsin highlights local variations in unfolding energy

Reprinted from

Patrick R. Heenan, Hao Yu, Matthew G. W. Siewny, and Thomas T. Perkins. Improved free-energy landscape reconstruction of bacteriorhodopsin highlights local variations in unfolding energy. **The Journal of Chemical Physics**, 148(12):123313, December 2017.

with the permission of AIP Publishing.

5.1 Abstract

Precisely quantifying the energetics that drive the folding of membrane proteins into a lipid bilayer remains challenging. More than 15 years ago, atomic force microscopy (AFM) emerged as a powerful tool to mechanically extract individual membrane proteins from a lipid bilayer. Concurrently, fluctuation theorems, such as the Jarzynski equality, were applied to deduce equilibrium free energies (ΔG_0) from non-equilibrium single-molecule force spectroscopy (SMFS) records. The combination of these two advances in single-molecule studies deduced the free-energy of the model membrane protein bacteriorhodopsin in its native lipid bilayer. To elucidate this free-energy landscape at a higher resolution, we applied two recent developments. First, as an input to the recon-

struction, we used force-extension curves acquired with a 100-fold higher time resolution and 10-fold higher force precision than traditional AFM studies of membrane proteins. Next, by using an inverse Weierstrass transform and the Jarzynski equality, we removed the free energy associated with the force probe and determined the molecular free-energy landscape of the molecule under study, bacteriorhodopsin. The resulting landscape yielded an average unfolding free energy per amino acid (aa) of 1.0 $\pm$ 0.1 kcal/mol, in agreement with past single-molecule studies. Moreover, on a smaller spatial scale, this high-resolution landscape also agreed with an equilibrium measurement of a particular three-aa transition in bacteriorhodopsin that yielded 2.7 kcal/mol/aa, an unexpectedly high value. Hence, while average unfolding ΔG_0 per aa is a useful metric, the derived high-resolution landscape details significant local variation from the mean. More generally, we demonstrated that, as anticipated, the inverse Weierstrass transform is an efficient means to reconstruct free-energy landscapes from AFM data.

5.2 Introduction

Membrane proteins perform critical biological functions, such as light harvesting, signaling, and transport. To carry out these and other diverse functions, they fold into equilibrium structures within a lipid bilayer [137]. Yet, predicting the structure and stability of membrane proteins significantly lags behind the success for globular proteins [137]. For instance, models still struggle to predict the tilt and overall packing of transmembrane (TM) α-helices. Hence, there is an ongoing need to better quantify the molecular forces that drive and stabilize the folding of membrane proteins. As with globular proteins [53], the energy landscape provides the fundamental framework for understanding membrane-protein folding and structure stabilization [138].

Single-molecule force spectroscopy (SMFS) has emerged as an important tool in determining the energetics underlying the folding and unfolding of individual proteins [25–28]. For membrane proteins, atomic force microscopy (AFM) is the modality of choice [140], since individual proteins

Figure 5.1: High-resolution studies of bacteriorhodopsin (BR) (A) A cartoon illustrating BR being unfolded from its C-terminal end using a modified, ultrashort cantilever. Each helix is denoted by a letter. Color coding highlights the unfolding topology as helix pairs or the terminal A helix are extracted. (B) A canonical force-extension curve while stretching at v = 300 nm/s shows the major intermediates corresponding to pulling on the top of the E, C and A helix. The initial portion of the force-extension curves was not analyzed due to the confounding effects of non-specific surface adhesion (grey box). The colored bars correspond to the colored helical regions from panel a. (C) Force-vs-time record of the highlighted black box in panel b shows near-equilibrium unfolding and refolding at the top of helix A over a 13-amino-acid (aa) segment. (D) Multiple force-extension curves of BR show numerous detected unfolding intermediates. Curves were well modeled by worm-like chain model within a particular state (dashed lines). (E) Force-vs-time record shows repeated unfolding and refolding of a 3-aa segment during an equilibrium assay (v = 0 nm/s) near the top of helix E. For clarity, 5-MHz data (light purple) was smoothed to 25 kHz (dark purple). (F) A reconstructed 1D free-energy landscape based on ~100-ms records of equilibrium data with 1-µs resolution tilted to $F_{1/2}$, the force at which the two states are equally likely to be occupied. Reconstruction was based on p_{fold} [139]. Error bars represent the standard error of the mean. Dashed line represent the location of transition state determined from a Bell analysis of state lifetime, with the grey box denoting the standard deviation in that localization. The data for Figure 5.1 *B*–*F* are from [72].

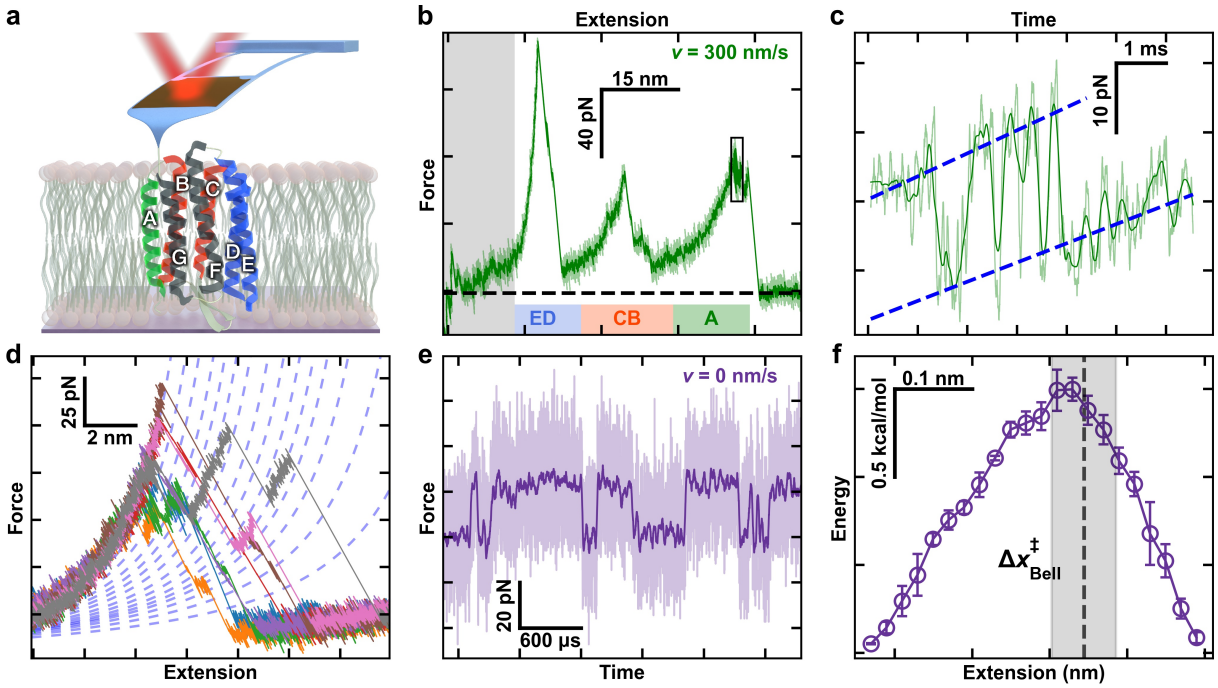

can be mechanically extracted from their native bilayer [141]. In the canonical assay, the tip of a cantilever is pressed into bacteriorhodopsin (BR) embedded in its native lipid bilayer to promote nonspecific attachment [141]. The tip is then retracted at constant velocity while force is deduced from the bending of the cantilever, revealing a series of unfolding peaks in the force-extension curve (Figure 5.1 *A*–*B*). The dominant peaks correspond to pulling on the top of TM helix pairs or a terminal helix, notably the ED and CB helix pairs as well as the A helix. Importantly, these AFM-based studies provide insight into the energetics of membrane proteins in lipid bilayers, rather than in detergent. Moreover, AFM studies provide a reproducible reference state, the fully unfolded protein. In contrast, the "unfolded" protein in ensemble unfolding assays retains α-helical content and therefore provides a poor reference state [137].

Complementing experimental advances that led to SMFS studies of individual proteins and nucleic-acid structures, theoretical advances enabled the determination of equilibrium free-energy values (ΔG_0) from analysis of non-equilibrium force-extension curves [57]. Such analysis provides important information beyond the distances to transition states ($\Delta x^{\ddagger}$) and the zero-force dissociation rate constant (k_{off}) determined using Bell-Evans analysis of dynamic force spectroscopy data [30, 111]. In particular, as demonstrated in pioneering studies of structured RNA using optical tweezers [51, 142], a 1D free-energy landscape can be obtained by extending the Jarzynski equality [143] via the weighted histogram method developed by Hummer and Szabo [57]. Salient to this present work, Hummer and Szabo's original paper applied the weighted histogram method to deduce the free-energy landscape for the ED helix pair bacteriorhodopsin, yielding an average of ΔG_0 of 1.1 per amino acid (aa) estimated from eight force-extension curves. Using significantly more traces ($N \approx 600$), Preiner *et al.* extended this analysis over five helices (E–A) reported an average ΔG_0 of 1.3 ± 0.2 kcal/mol/aa (mean ± SD) [144].

A higher-resolution description of the free-energy landscape enables a more quantitative comparison between the location and lifetimes of short-lived unfolding intermediates and the underlying energy landscape. Recent advances in applying modified ultrashort cantilevers optimized for 1-μs

resolution SMFS [145, 146] enabled the measurement of bacteriorhodopsin with a 100-fold higher time resolution and 10-fold higher force precision that, in turn, revealed rapid near-equilibrium folding (Figure 5.1 *C*) and a multitude of previously unresolved, transiently occupied intermediates (Figure 5.1 *D*) [72]. These cantilevers also enabled the first equilibrium study of membrane protein folding, where a particular three-amino-acid transition near the top of the E helix repeatedly unfolded and refolded (Figure 5.1 *E*). Reconstruction of the free-energy landscape underlying this transition (Figure 5.1 *F*) revealed an unexpectedly large ΔG_0 per aa (2.7 kcal/mol) at $F = 0$ pN. Here, we merged these experimental advances in acquiring high-resolution force-extension curves with theoretical advances in reconstructing the landscape from non-equilibrium records. In particular, we used the inverse Weierstrass transform (IWT) applied in conjunction with the Jarzynski free-energy integral to avoid convolving the compliance of the AFM cantilever into the resulting free-energy landscape [39]. Importantly, the IWT works best for studies using a stiffer force probe [39] —making it particularly suitable for AFM-based assays ($k \approx$ 6–100 pN/nm)—due to their higher probe stiffness relative to earlier application in an optical-trapping-based assay ($k = 0.4$ pN/nm) [147]. The resulting landscape yielded an average unfolding free energy per amino acid (aa) of 1.0 ± 0.1 kcal/mol (mean ± SEM), in close agreement with past single-molecule studies [57, 144, 148]. Moreover, on a smaller spatial scale, this landscape also agreed with the recent equilibrium measurement that showed an unexpectedly high ΔG_0 per aa near the top of the E helix. Hence, while average unfolding ΔG_0 per aa is a useful metric, the resulting high-resolution landscape confirmed significant local variations from the mean.

5.3 Free-energy landscape reconstruction

As background, the Jarzynski equality is remarkable because it relates the work done during many repetitions of a non-equilibrium process to the equilibrium free-energy difference as a function of an experimental parameter. For our work, the experimental parameter was the position of the cantilever base relative to the surface, or 'z' [38]. More precisely, the Jarzynski equality is a

thermodynamic relationship between the Helmholtz free energy of a system $A(z)$ and the measured work $W(z)$:

$$e^{-\beta A(z)} = \langle e^{\beta W(z)} \rangle_N \tag{5.1}$$

where z is the zero-force equilibrium position of the force probe, β is the inverse of the thermal energy $k_B T$, and the average is taken over N independent stretching trajectories, each starting and ending at the same choice of z [39, 143, 149]. The Jarzynski equality is exact only in the limit as $N \to \infty$, but is approximately true for finite N. In practice, SMFS experiments apply the Jarzynski equality by repeatedly folding or unfolding a single molecule of interest using a force probe. In this case, the work is the integral of the force as a function of the cantilever position z. For example, in the constant velocity experiments used in our AFM assay, $z(t)=vt+z_i$, and the integral for each stretching experiment starts at the same well-defined $z_\mathbf{i}$ associated with the aligned curves (see below). Tip-sample separation, which is also the molecular extension (x) in an AFM assay, is not uniquely defined at all values of z. The molecule may be in different folding states and therefore different molecular extensions, referred to henceforth as q as is common in landscape-reconstruction literature [39]. The Jarzynski equality requires that all molecules included in the calculation start (z_i) and finish (z_f) in an equilibrium state.

Hummer and Szabo's original extension of the Jarzynski equality for SMFS studies determines the landscape as a function of molecular extension (q), instead of SMFS probe position (z), and also removes the energetic contribution of the force probe via a weighted histogram method [57]. In subsequent work, they applied an IWT to simplify this calculation and make more efficient use of a limited set of force-extension curves by assuming a stiff, harmonic pulling apparatus[39, 147]. Put differently, the curvature (*i.e.*, the second spatial derivative) of the true underlying energy landscape should not exceed the stiffness of the force probe. Indeed, the consequence of not fulfilling this assumption was theoretically anticipated [39] and experimentally demonstrated for a RNA pseudo-

knot studied using an optical trap [147]. In that case, the derived landscape was filtered by the soft probe leading to a lower barrier height (akin to applying a spatial filter that smooths out sharp features). Hence, energy landscape reconstruction by the IWT is well suited to AFM-based assays due to the higher stiffness of AFM cantilevers in comparison to optical traps [39, 147].

As input for IWT reconstruction of BR, we used a set of 106 force-extension curves of BR extracted from its native lipid bilayer (purple membrane for BR) acquired using focused-ion-beam modified BioLever Fast cantilevers (AC10DS, Olympus). The details of this data acquisition and the force-extension curves have been previously published [72]. Briefly, modified cantilevers ($k \approx$ 10–40 pN/nm) were pressed into the purple membrane at ~1 nN for 1 s and retracted from the surface at a constant velocity (v) of 300 nm/s. Data were recorded at 5 MHz on a commercial AFM (Cypher ES, Asylum Research) and then smoothed with a second-order, 500-point Savitsky-Golay filter for all subsequent analysis. As is standard for SMFS-studies of BR [140], the curves were laterally aligned to superimpose the major obligate intermediate associated with pulling on the top of the E helix. These aligned traces (Figure 5.2 *A*) then served as input to calculate the free-energy landscape via the IWT. The unfolding of the GF helix pair was not analyzed due to the confounding effects of non-specific tip-sample adhesion.

The IWT reconstructs the free-energy landscape, approximately removing the contribution of the force probe, by calculating statistics on an ensemble of N force-extension curves. For a particular curve n with measured force $F_n(z)$, the work used by the IWT is defined as

$$W_n(z) = \int_{z_i}^{z} F_n(z^{'})dz^{'} \tag{5.2}$$

where z runs from $z_{\mathbf{i}}$ to $z_{\mathbf{f}}$ at a given velocity v for all N force-extension curves. The Jarzynski equality determines the Helmholtz free energy $A(z)$, which includes energy from the probe. The IWT approximately removes the contribution of the probe by calculating the so-called work-

weighted ensemble statistics. The work-weighted force and force squared, denoted with double brackets, are defined at each z as:

$$<< F(z) >>= \frac{\langle e^{\beta W_n(z)} F_n(z) \rangle_N}{e^{-\beta A(z)}} \text{ and } << F^2(z) >>= \frac{\langle e^{\beta W_n(z)} F_n^2(z) \rangle_N}{e^{-\beta A(z)}} \tag{5.3}$$

where $<X>_N$ denotes an average of X over the ensemble of force-extension curves at a fixed z. These work-weighted values are related to the first and second spatial derivatives of the Helmholtz free energy as follows:

$$\dot{A}(z) =<< F(z) >> \text{ and } 1 - \frac{\ddot{A}(z)}{k} = \frac{\beta}{k}(<< F^2(z) >> - << F(z) >>^2) \tag{5.4}$$

The IWT-based reconstruction uses the first and second derivatives to reconstruct the free-energy landscape as a function of molecular extension [39]:

$$G(q = z - \frac{\dot{A}(z)}{k}) \approx A(z) - \frac{\dot{A}(z)^2}{2k} + \frac{1}{2\beta} \ln(1 - \frac{\ddot{A}(z)}{k}) \tag{5.5}$$

Importantly, $G(q)$ is approximately the free energy of the molecule, instead of the free energy of the molecule and the probe. To avoid errors associated with numerical derivatives of noisy data, we calculated the energy derivatives, $\dot{A}(z)$ and $\ddot{A}(z)$, directly from the primary work-weighted force and force squared (see Figure 5.4) which, in turn, allowed $G(q)$ to be determined. To avoid errors in combining data sets acquired using different cantilever stiffnesses (k), we chose z_i = 18 nm + (20 pN/k), which corresponded to approximately F = 20 pN at an extension of 18 nm when pulling on the top of the ED helix pair. Each set of data, containing a minimum of 20 force-extension curves, corresponded to one cantilever and was reconstructed separately. After the transform was completed, the resulting free-energy landscapes were functions of molecular extension q (instead of z) and were averaged based on the number of traces associated with each cantilever data set. As

Figure 5.2: Process for free-energy landscape reconstruction of BR using an inverse Weierstrass transform (IWT). (A) A heat map of all force-extension curves used in this work. Data within ~18 nm of the surface are excluded due to surface adhesion. (B) Different components for calculating the molecular free energy ΔG_0 as a function of the molecular extension when using the IWT. The three components used in computing ΔG_0 as defined in Equation 5.5: A, (aqua, dot-dash) and terms involving its first and second derivative (pink, solid line and brown, dashed line; respectively). To promote comparison to panels a and c, the plotted lateral axis is q, molecule extension. (C) The ΔG_0 free energy as a function of molecular extension. Shaded region reports the standard deviation as deduced from a bootstrap analysis.

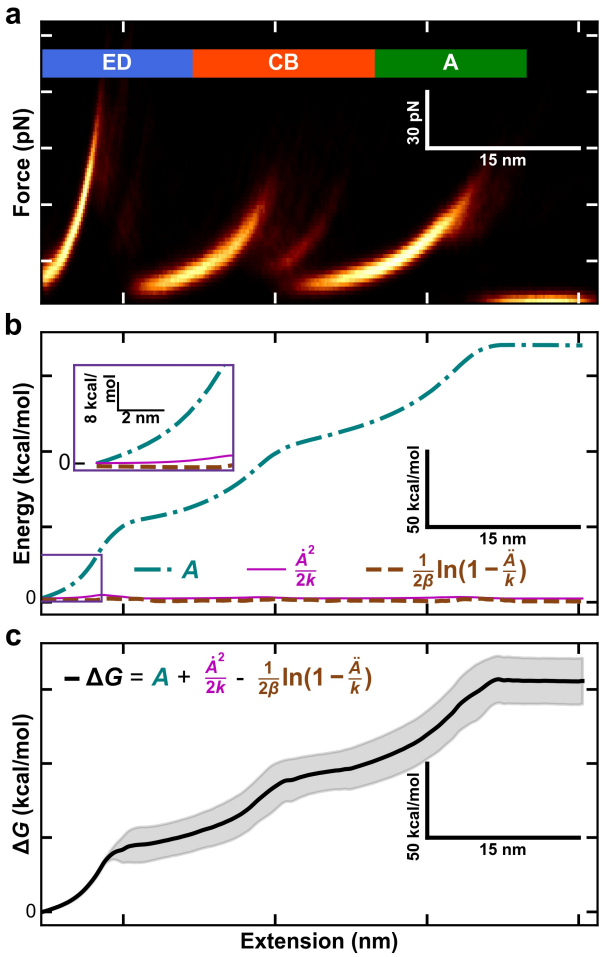

in previous work, [144] we found that we needed a minimum of 20 traces per cantilever to limit reconstruction error to reasonable levels.

Uncertainties in the landscape and its first derivative were determined by a bootstrap analysis[150]. In brief, 250 synthetic data sets were generated from the original set of 106 curves using random resampling with replacement. Only synthetic data sets with $1 - \frac{\ddot{A}(z)}{k} > 0$, as required by the IWT, were counted towards the total of 250. From the resulting ensemble of 250 landscapes, the standard deviation in simulated mean values was calculated after smoothing with a third order, piecewise polynomial to 0.4 nm. This smoothing choice was chosen to approximately minimize the product of error in $\dot{G}(q)$ and in the least-squared fitting of $G(q)$ across the bootstrapping rounds (see Figure 5.5). Future work with more traces from individual cantilevers and from cantilevers with a narrower range in k will decrease the uncertainties in landscape reconstruction.

We illustrate the process of calculating the IWT for BR from Equation 5.5 in Figure 5.2. The starting data consists of 106 aligned force-extension curves. As shown in Figure 5.2 *A*, the resulting heat map represents the ensemble of measurements needed to apply Jarzynski's inequality and the inverse Weierstrass transform. To highlight the contributions of the three components in Equation 5.5 in determining $G(q)$, we color coded a plot of $A(z)$ and the IWT corrections (Figure 5.2 *B*). The corrections were obtained as described above, using work-weighted histogram statistics[39, 149]. The resulting $G(q)$ was deduced from the sum of these three components and represents the free energy of the ED, CB, and A helical pairs of bacteriorhodopsin (Figure 5.2 *C*). Shaded regions represent the standard deviation deduced from the aforementioned bootstrap analysis.

5.4 Results and discussion

The local unfolding free energy of BR depended on the individual structural element being unfolded. Our resulting high-resolution free-energy landscape of BR's final five helices showed significant variation in slope as a function of extension and therefore unfolding energy per amino

acid (Figure 5.2 *C*). To highlight this variation, we computed the free-energy landscape and ΔG_0 per nm as a function extension for the individual major structural components (ED, CB, and A helices) (Figure 5.3 *A*–*C*). The mean ΔG_0 per aa is 1.0 ± 0.1 kcal/mol (mean ± SD) when calculated from the unfolding of the ED, CB, and A helices [156 ±15 kcal/mol (mean ± SD) over 160 amino acids of helices, traditionally taken as the top of the E-helix in AFM-based assays [151]]. This average value is slightly larger than bulk denaturation studies that report ~0.5 kcal/mol/aa [152] and similar to past single-molecule results of 1.1–1.3 kcal/mol per aa [57, 144, 148].

For completeness, we note that most rigorous to-date experimental determination of the total ΔG_0 for the E–A helices is 227 ± 38 kcal/mol (mean ± SD) and is therefore significantly higher than our value of 156 ±15 kcal/mol, a result not precisely reflected in the reported 1.3 kcal/mol per aa [144]. The origin of this difference is that this prior work used 171 amino acids in their analysis, which includes an extra 11 amino acids associated with the loop between the top of E and F helices and the first turn of the F-helix. If we reanalyze this earlier result with the same number of amino acids as used in this present work, their value now becomes 1.4 ± 0.2 kcal/mol per aa. Our average unfolding energy per amino acid therefore lies below this prior experimental result. Possible origins of this difference could be the improved precision of our force-extension curves and/or some reduction in the total ΔG_0 values due to the IWT poorly resolving stiff portions of the landscapes compared to the weighted histogram method (see below) [147]. Finally, a recent coarse-grained molecular dynamics simulation predicts a free energy of transfer from bulk water to lipid of -130 kcal/mol for the 160-aa sequence in our work, or about 0.8 kcal/mol per aa for unfolding BR from its lipid bilayer (see Section S1) [153].

Our work also documented that ΔG_0 per nm varied more than 15-fold, from 11 kcal/mol at the top of the ED helix pair to 0.6 kcal/mol at the bottom of the same helix pair. While it has long been known that hydrophobicity of the amino-acid sequence within the lipid bilayer and inter- and intra-helix interactions contribute to this variation [154], recent work also shows variations in the strength of hydrogen bonds within TM helices [155]. To convert this local, single-

molecule force spectroscopy derived metric to the more commonly reported ΔG_0 per aa, we note that there are ~3 amino acid residues per nm of contour length for an unstructured peptide based on crystallography (0.36 nm/aa) [156]. Given the elevated forces experienced during unfolding portions of the records, we approximated extension with contour length and therefore approximated a local value for ΔG_0 per aa as 1/3 of ΔG_0 per nm after taking the spatial derivative of the reconstructed free-energy landscape (*e.g.*, Figure 5.2 *C*). As described in the methods section, the landscapes and its derivatives were calculated for each set of data derived from a cantilever of fixed stiffness, after smoothing with a piecewise polynomial to 0.4 nm. At the top of the ED helix pair, we observed the highest local ΔG_0 per aa followed by the top of the CB and A helices.

One immediate trend from this data was a higher ΔG_0 per aa when BR was more fully folded. Thus, looking forward, an assay that probes the initial unfolding of a membrane protein where most, if not all of intra- and inter-helix bonds are still intact, offers the best opportunity to precisely quantify ΔG_0 per aa under native-like conditions. Unfortunately, while a few studies have quantified the initial unfolding of the GF helix [151, 157], precise quantification remains hindered by non-specific adhesion between the tip and the surface [140, 141, 144]. Another trend in our data was that ΔG_0 per aa for unwinding the first portion of a TM helix pair was higher than when unfolding the second helix. Put more simply, once the first helix in a TM helix pair was extracted, the second helix took significantly less energy to extract.

Interestingly, we also achieved agreement between the unfolding free energies obtained by equilibrium and dynamic assays. As discussed in the introduction, we had previously deduced an unexpectedly high ΔG_0 per aa [2.7 ± 0.1 kcal/mol (mean ± SEM)] for a particular transition near the top of the ED helix pair after reconstruction of the free-energy landscape from equilibrium data (Figure 5.1 *F*) [72]. The present IWT analysis of dynamic data yielded an average ΔG_0 per aa near the top of the ED helix, 2.9 ± 0.5 kcal/mol (mean ± SD), in agreement with the previous equilibrium result for a specific three amino-acid transition [72].

We emphasize that the ΔG_0 per aa measured here does not correspond to breaking a particular hydrogen-bond or fully solvating an amino acid out of a lipid bilayer, but results from a convolution of angstrom-scale motion of each amino acid along the stretching axis. We also note that the reported values include the contribution of the extended, unfolded protein. In other words, since the ED helix was folded at the start of the analysis, the entropic contribution to stretching unfolded polypeptides to high force is part of the resulting ΔG_0. Future experimental advances and/or applying more sophisticated analysis can minimize or theoretically separate out the energy associated with stretching these compliant unfolded peptides [7]. However, the situation for BR is distinctly different from standard optical-trapping assays which use much longer, 300–600-nm double-stranded nucleic acids handles to accommodate the geometry of optical-trapping studies [36, 158, 159].

Figure 5.3: Local unfolding free energies as a function of extension vary broadly between and within BR's major structural elements (the ED, CB and A helices, respectively). (A) Local unfolding free energy per nm (left axis) and reconstructed energy landscape (right axis) for the ED helix pair. The local unfolding free-energy is the spatial first derivative of the reconstructed landscape. The standard deviations in the deduced values are the shaded region around the measured value as deduced by a bootstrap analysis. (B,C) Same analysis for the BC helix pair and the A helix, respectively.

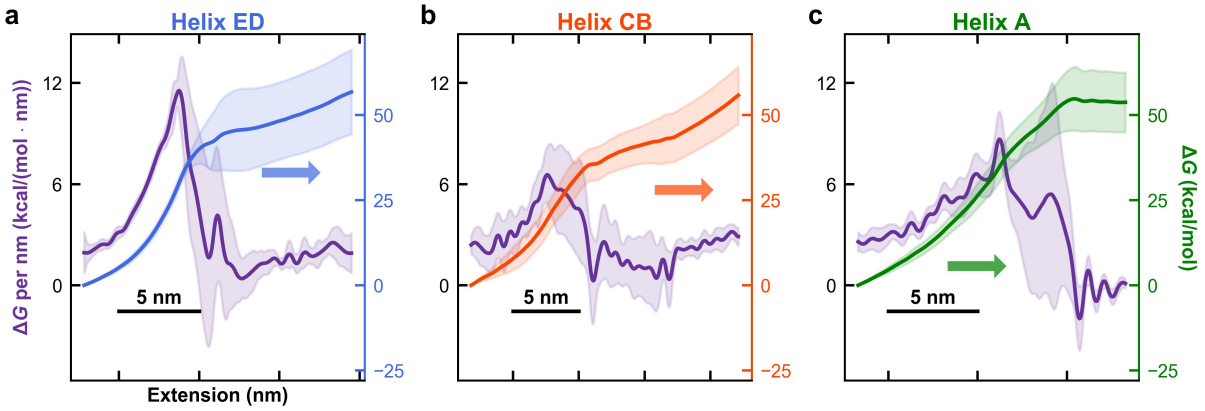

Somewhat unexpectedly, we observed a local landscape stiffness—the second derivative of the reconstructed landscape—greater than any particular cantilever stiffness used. Yet, Hummer and Szabo's implementation of the IWT assumed a stiff probe, which should limit the reconstructed landscape from having a stiffness that exceeds the force probe [39]. More quantitatively, the greatest

landscape curvature for BR was 8 kcal/(mol nm^2) or 55 pN/nm, larger than the stiffest cantilever used (40 pN/nm). We attribute this small discrepancy to errors in polynomial fitting and numerical differentiation. On the scientific front, it is therefore likely that our reconstructed landscape represents a lower bound on the local value of ΔG_0 per nm, akin to early studies of RNA pseudoknots studied with optical traps[147]. Hence, as shown in that optical-trapping work, [147] the weighted histogram method is better for reconstructing landscapes containing such "stiff" features. For the vast majority of BR's landscape, the stiff-spring approximation of the IWT was fulfilled and yielded a more accurate landscape reconstruction (Figure 5.6). In addition, the almost-negligible correction to the landscape from the $\ddot{A}$ term outside of the ED Helix (Figure 5.2 *B*, brown) confirmed that higher-order corrections were unlikely to affect the landscape of the CB and A helices. In fact, the corrections of the IWT to the Jarzynski equality were small except near the top of the E helix, which interestingly is also the same location where equilibrium flickering was previously reported (Figure 5.1 *E*). Looking forward, using a stiffer cantilever is the obvious means to fulfill the stiff probe assumption. Yet, stiffer ultrashort cantilevers are not overdamped (quality factor $Q > 0.5$) [145], violating an assumption underlying traditional force spectroscopy theories [52, 111, 160]. Hence, there is also ongoing need to optimize modified ultrashort cantilevers for higher k but low Q.

5.5 Conclusion

As anticipated [39, 147], the IWT provides an efficient and accessible means to reconstruct free-energy landscapes when using AFM, even for complicated landscapes such as BR. The energy landscape reconstruction presented here highlights significant variation along the unfolding free-energy landscape. The overall trend is similar to early work [144] but with improvements associated with reconstruction of the landscape from much higher resolution force-extension curves [72, 145] and using the IWT [39] that efficiently removes the energy contribution associated with the bending of the cantilever. As a result, we achieved a more accurate and higher-resolution reconstruction. The resulting landscape yielded an average ΔG_0 per aa of 1.0 $\pm$ 0.1 kcal/mol, in much better

agreement with past single-molecule studies than our one prior determination of ΔG_0 per aa (2.7 kcal/mol) derived from an equilibrium assay probing a particular three aa transition near the top of the ED helix pair. Importantly, on a smaller spatial scale, this high-resolution landscape also agreed with that prior equilibrium measurement of the three-aa transition ($\Delta G_0 = 2.9 \pm 0.5$ kcal/mol/aa). Indeed, the highest-measured curvature of the free-energy landscape (~55 pN/nm) was limited by cantilever stiffness (~10–40 pN/nm), and hence represents a lower bound of local determination of ΔG_0 per aa due to the underlying assumption of a stiff probe in applying the IWT [39, 147]. Future developments that enable efficient unfolding and refolding over reversible transitions would enable comparing energy landscapes deduced from state-based models [37] with those used here, providing another method for investigating and verifying local free-energy landscape reconstruction of membrane proteins.

5.6 Acknowledgements

We thank Michael Woodside for useful discussions.

5.7 Supporting Information

5.7.1 Figures

Figure 5.4: Work-weighted statistics are necessary for accurate landscape reconstruction. (a) For an example landscape, the Helmholtz free energy, A, is plotted versus molecular extension (q). A representative region is highlighted in red and detailed in an inset. A(q) has been smoothed with a second-order, 500-point Savitsky-Golay filter. (b) The change in Helmholtz energy, $dA(q)$, is plotted versus extension. This derivative was obtained by the finite difference method (black) and via the work-weighted force (pink). The finite difference method yields curves with significantly higher noise. The high noise can be attributed to the fact that A(q) and q are noisy outputs of the IWT. (**c**) The "Helmholtz force", $\dot{A}(q)$, obtained by work-weighted statistics, yields the expected shape and order of magnitude of a force-extension curve. Note the extension starts with pulling on at the top of the E helix as opposed to experimental records that start at the top of the G helix (e.g., Figure 5.1 *B*).

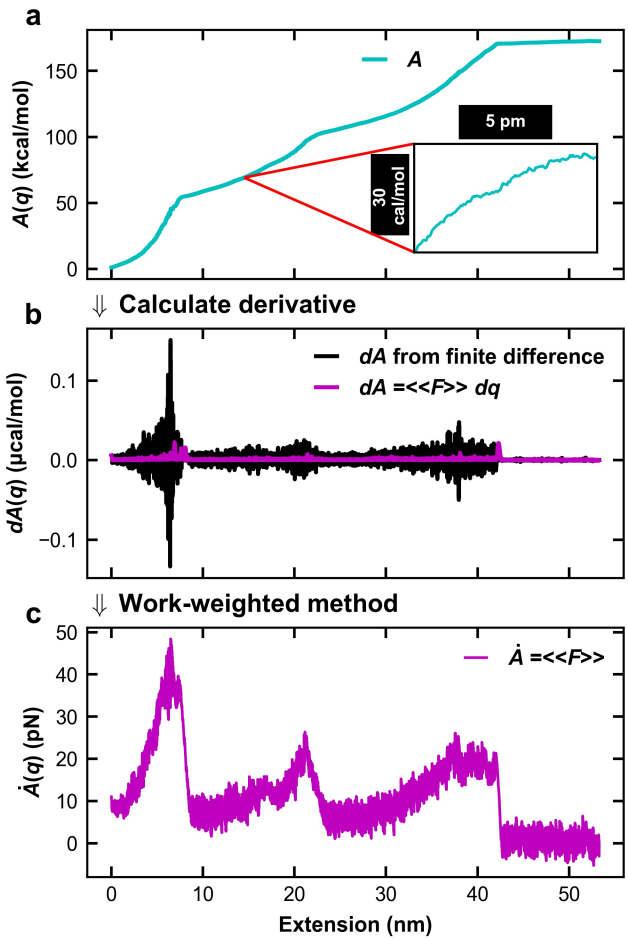

Figure 5.5: Filtering choice balances fitting and derivative error with spatial resolution. This figure plots error versus filtering size. Error is defined as the product of the fitting error and derivative error. For a fixed filtering size, the fitting error is the mean over bootstrapping iterations of the summed least-squared residuals of a spline fit to $G(q)$, and the derivative error is the variance in $\dot{G}(q)$ over bootstrapping iterations. The error changes very little (<5%) between 0.3 nm and 1 nm. The choice of 0.4 nm, highlighted in red, was chosen as a compromise between landscape resolution and error minimization.

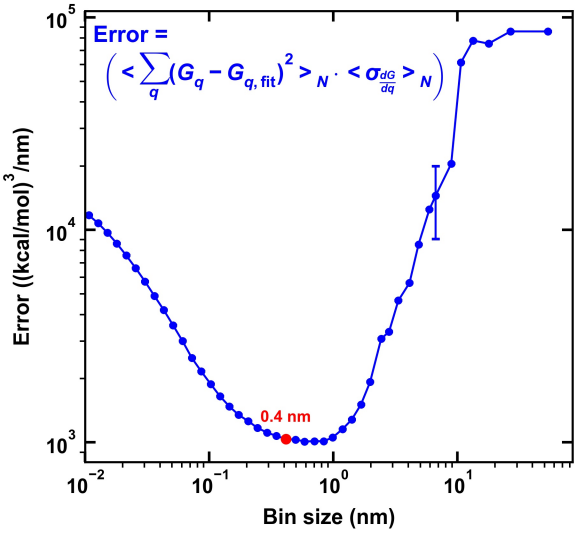

Figure 5.6: The mean landscape curvature (or stiffness) plotted versus extension relative to the start of the ED helix. Each helical region is color-coded, with a labeled bar underneath. The landscape stiffness is almost always less than the cantilever stiffness. A typical cantilever stiffness of 25 pN/nm is plotted as a dotted magenta line. The ED helix is the only helix with a significant region exceeding the cantilever stiffness.

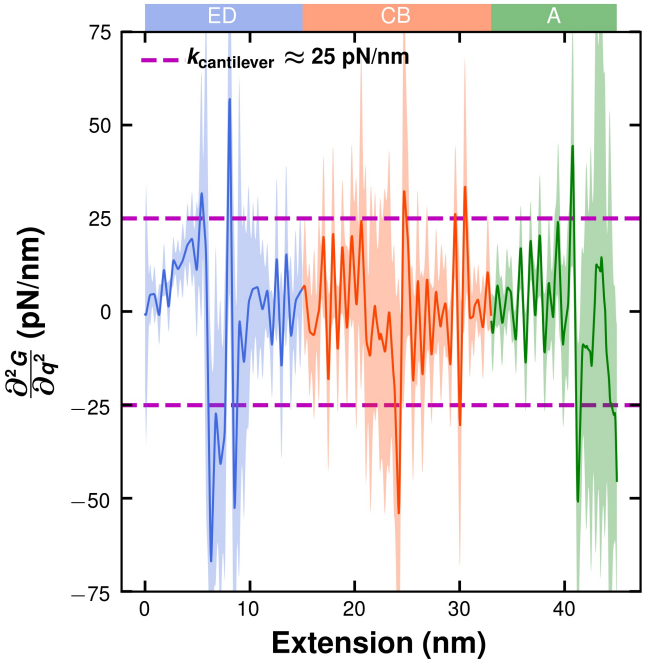

5.7.2 Methodology for comparison with coarse-grained MD simulation

The amino acid sequence of BR which was unfolded for this work is (listed from C to N terminus): [72]

AKSTFGFFLVYLIYLMAATSIAWWVFRYSYVKTLAGVLGTGIMIGDAGVLALI
TGQDADVLLALDLLLLPTTFLWDAYRAWYIPNQEGGFPVMTLGYGLLMSLYMTF
AIAPVLTTIAYFKKADPDSVGMGKVLFYLTGLGMLATGLALWIWEPRGTIQAQ

We used the following table 5.1 (adapted from Yamada et al [153]) to determine the free energy of transfer from water to lipid. For the purposes of comparison, the unfolding energy of bR out of lipid into buffer was assumed to be equal and opposite to the energy of transfer of bR from water to lipid:

Table 5.1: Amino acid transfer energies Free energy of transfer from water to lipid used by Yamada et al [153] in coarse-grained MD simulations.

Amino Acid	**Energy of Transfer (kJ/mol)**
Ala	-3.5
Arg	21
Asn	9.6
Asp	23.9
Cys	-2.7
Gln	6.2
Glu	19.3
Gly	-1.3
His	2.2
Ile	-11.7
Leu	-11.7
Lys	11.8
Met	-6.8
Phe	-14.3
Pro	-7
Ser	5.8
Thr	4.5
Trp	-13.4
Tyr	-9.7
Val	-8.8
N Terminus	9.8

Chapter 6

Conclusions and future directions

AFM-based single molecule imaging and force spectroscopy techniques are powerful tools for investigating biological systems at physiologically relevant buffer conditions. Although applications of the present work improve the biological relevance of data acquired by AFM-based imaging and SMFS, new possibilities enabled by the present work will lead to further progress, as detailed below.

Chapter 5 details how energy landscape reconstructions obtained from SMFS data measure the variations in free energy associated with dissociating specific portions of membrane proteins. The adoption of site-specific chemistry increases the throughput and quality of data and enables reproducible unfolding and refolding of near-native biomolecular structure. Such unfolding and refolding data provide more insight into the energy landscape of the system under interest (see Chapter 1. Therefore, experiments which leverage site-specific chemistry will be much better positioned for unfolding and refolding studies. In addition, performing unfolding-refolding experiments with site-specific chemistry as a function of perturbation (*e.g.* protein mutation, buffer conditions, cantilever attachment point), will provide more insight into the molecular structures or energy landscapes.

Chapter 4 demonstrates how to accurately and automatically extract unfolding event locations (and therefore the loading rate and rupture force) from SMFS data. As mentioned above, experiments which unfold *and* refold a system improve biophysical insight. Therefore, extending

the method detailed in Chapter 4 from only detecting unfolding events to also detecting refolding events would greatly improve its utility as an SMFS analysis technique.

Chapter 3 describes a technique for imaging surface-bound DNA, resulting in DNA bound strong enough for imaging and maintaining a structure consistent with equilibrated, B-form DNA. As of publication of this method, all other AFM techniques performed in liquid featured kinetically trapped DNA and therefore DNA with an artificially low apparent two-dimensional persistence length (*i.e.* artificially high flexibility). By extension, and perhaps more interestingly, any AFM imaging method of protein-bound DNA strongly perturbed the system of interest. Therefore, future work should identify previously studied systems of interest (*e.g.* DNA-protein complexes exclusively studied in air or kinetically trapped in liquid) and determine if the prior results hold with surface-equilibrated samples. In addition, DNA-protein systems which have never been studied via AFM but which are expected to have a mechanical difference along the DNA contour (*e.g.* bending, morphological change, oligomerization) are also good applications of the experimental method outlined in Chapter 3.

Bibliography

[1] Taekjip Ha and Philip Tinnefeld. Photophysics of Fluorescent Probes for Single-Molecule Biophysics and Super-Resolution Imaging. Annual Review of Physical Chemistry, 63(1):595–617, May 2012.

[2] Rahul Roy, Sungchul Hohng, and Taekjip Ha. A practical guide to single-molecule FRET. Nature Methods, 5(6):507–16, June 2008.

[3] Benjamin Schuler and William A Eaton. Protein folding studied by single-molecule FRET. Current Opinion in Structural Biology, 18(1):16–26, February 2008.

[4] Chirlmin Joo, Hamza Balci, Yuji Ishitsuka, Chittanon Buranachai, and Taekjip Ha. Advances in Single-Molecule Fluorescence Methods for Molecular Biology. Annual Review of Biochemistry, 77(1):51–76, June 2008.

[5] William J. Greenleaf, Michael T. Woodside, and Steven M. Block. High-resolution, single-molecule measurements of biomolecular motion. In Annual Review of Biophysics and Biomolecular Structure, volume 36 of Annual Review of Biophysics, pages 171–190. 2007.

[6] Keir C. Neuman and Attila Nagy. Single-molecule force spectroscopy: optical tweezers, magnetic tweezers and atomic force microscopy. Nature Methods, 5(6):491–505, June 2008.

[7] Michael T. Woodside and Steven M. Block. Reconstructing Folding Energy Landscapes by Single-Molecule Force Spectroscopy. Annual Review of Biophysics, 43(1):19–39, 2014.

[8] G. Binnig, C. F. Quate, and Ch. Gerber. Atomic Force Microscope. Physical Review Letters, 56(9):930–933, March 1986.

[9] H. G. Hansma, J. Vesenka, and et al. Reproducible Imaging and Dissection of Plasmid DNA Under Liquid with the Atomic Force Microscope. Science, 256(5060):1180, May 1992.

[10] H G Hansma, M Bezanilla, F Zenhausern, M Adrian, and R L Sinsheimer. Atomic force microscopy of DNA in aqueous solutions. Nucleic Acids Research, 21(3):505–512, February 1993.

[11] Y L Lyubchenko, P I Oden, D Lampner, S M Lindsay, and K A Dunker. Atomic force

microscopy of DNA and bacteriophage in air, water and propanol: the role of adhesion forces. Nucleic Acids Research, 21(5):1117–1123, March 1993.

[12] Michael J. Allen, X. Fan Dong, Timothy E. O'Neill, Peter Yau, Stephen C. Kowalczykowski, Joe Gatewood, Rod Balhorn, and E. Morton Bradbury. Atomic force microscope measurements of nucleosome cores assembled along defined DNA sequences. Biochemistry, 32(33):8390–8396, August 1993.

[13] M. Guthold, M. Bezanilla, D. A. Erie, B. Jenkins, H. G. Hansma, and C. Bustamante. Following the assembly of RNA polymerase-DNA complexes in aqueous solutions with the scanning force microscope. Proceedings of the National Academy of Sciences, 91(26):12927–12931, December 1994.

[14] H.G. Hansma, K.J. Kim, D.E. Laney, R.A. Garcia, M. Argaman, M.J. Allen, and S.M. Parsons. Properties of Biomolecules Measured from Atomic Force Microscope Images: A Review. Journal of Structural Biology, 119(2):99–108, July 1997.

[15] Sandor Kasas, Neil H. Thomson, Bettye L. Smith, Helen G. Hansma, Xingshu Zhu, Martin Guthold, Carlos Bustamante, Eric T. Kool, Mikhail Kashlev, and Paul K. Hansma. Escherichia coli RNA Polymerase Activity Observed Using Atomic Force Microscopy. Biochemistry, 36(3):461–468, January 1997.

[16] Darren J. Ellis, David T. F. Dryden, Torunn Berge, J. Michael Edwardson, and Robert M. Henderson. Direct observation of DNA translocation and cleavage by the *Eco*KI endonuclease using atomic force microscopy. Nature Structural & Molecular Biology, 6(1):15–17, January 1999.

[17] M. Lysetska, A. Knoll, D. Boehringer, T. Hey, G. Krauss, and G. Krausch. UV light-damaged DNA and its interaction with human replication protein A: an atomic force microscopy study. Nucleic Acids Research, 30(12):2686–2691, June 2002.

[18] Neal Crampton, William A. Bonass, Jennifer Kirkham, Claudio Rivetti, and Neil H. Thomson. Collision events between RNA polymerases in convergent transcription studied by atomic force microscopy. Nucleic Acids Research, 34(19):5416–5425, November 2006.

[19] Isabelle Sorel, Olivier Piétrement, Loïc Hamon, Sonia Baconnais, Eric Le Cam, and David Pastré. The EcoRI−DNA Complex as a Model for Investigating Protein−DNA Interactions by Atomic Force Microscopy. Biochemistry, 45(49):14675–14682, December 2006.

[20] Atsushi Miyagi, Toshio Ando, and Yuri L. Lyubchenko. Dynamics of Nucleosomes Assessed with Time-Lapse High-Speed Atomic Force Microscopy. Biochemistry, 50(37):7901–7908, September 2011.

[21] Yuri L. Lyubchenko. Preparation of DNA and nucleoprotein samples for AFM imaging. Micron, 42(2):196–206, February 2011.

[22] Toshio Ando, Takayuki Uchihashi, and Noriyuki Kodera. High-Speed AFM and Applications to Biomolecular Systems, May 2013.

[23] Divakaran Murugesapillai, Serge Bouaziz, L. James Maher, Nathan E. Israeloff, Craig E. Cameron, and Mark C. Williams. Accurate nanoscale flexibility measurement of DNA and DNA–protein complexes by atomic force microscopy in liquid. Nanoscale, August 2017.

[24] Mikihiro Shibata, Hiroshi Nishimasu, Noriyuki Kodera, Seiichi Hirano, Toshio Ando, Takayuki Uchihashi, and Osamu Nureki. Real-space and real-time dynamics of CRISPR-Cas9 visualized by high-speed atomic force microscopy. Nature Communications, 8(1):1430, December 2017.

[25] Matthias Rief, Mathias Gautel, Filipp Oesterhelt, Julio M. Fernadez, and Hrmann E. Gaub. Reversible unfolding of individual titin immunoglobulin domains by AFM. Science; Washington, 276(5315):1109–12, May 1997.

[26] Miklos S. Z. Kellermayer, Steven B. Smith, Henk L. Granzier, and Carlos Bustamante. Folding-unfolding transitions in single titin molecules characterized with laser tweezers. Science; Washington, 276(5315):1112–6, May 1997.

[27] Alessandro Borgia, Philip M. Williams, and Jane Clarke. Single-molecule studies of protein folding. In Annual Review of Biochemistry, volume 77, pages 101–125. Annual Reviews, Palo Alto, 2008. WOS:000257596800006.

[28] Keir C. Neuman and Attila Nagy. Single-molecule force spectroscopy: optical tweezers, magnetic tweezers and atomic force microscopy. Nature Methods, 5(6):491–505, June 2008.

[29] V. T. Moy, E. L. Florin, and H. E. Gaub. Intermolecular forces and energies between ligands and receptors. Science (New York, N.Y.), 266(5183):257–259, October 1994.

[30] R. Merkel, P. Nassoy, A. Leung, K. Ritchie, and E. Evans. Energy landscapes of receptor-ligand bonds explored with dynamic force spectroscopy. Nature, 397(6714):50–3, January 1999.

[31] S. Kasas, N. H. Thomson, B. L. Smith, P. K. Hansma, J. Miklossy, and H. G. Hansma. Biological applications of the AFM: From single molecules to organs. International Journal of Imaging Systems and Technology, 8(2):151–161, January 1997.

[32] D Fotiadis. Imaging and manipulation of biological structures with the AFM. Micron, 33(4):385–397, January 2002.

[33] Andrea Alessandrini and Paolo Facci. AFM: a versatile tool in biophysics. Measurement Science and Technology, 16(6):R65–R92, June 2005.

[34] Elias M Puchner and Hermann E Gaub. Force and function: probing proteins with AFM-based force spectroscopy. Current Opinion in Structural Biology, 19(5):605–614, October 2009.

[35] Daniel J. Müller and Yves F. Dufrêne. Atomic force microscopy: a nanoscopic window on the cell surface. Trends in Cell Biology, 21(8):461–469, August 2011.

[36] Michael T. Woodside, Peter C. Anthony, William M. Behnke-Parks, Kevan Larizadeh, Daniel Herschlag, and Steven M. Block. Direct Measurement of the Full, Sequence-Dependent Folding Landscape of a Nucleic Acid. Science, 314(5801):1001–1004, November 2006.

[37] Yaojun Zhang and Olga K. Dudko. A transformation for the mechanical fingerprints of complex biomolecular interactions. Proceedings of the National Academy of Sciences of the United States of America, 110(41):16432–16437, October 2013.

[38] C. Jarzynski. Nonequilibrium Equality for Free Energy Differences. Physical Review Letters, 78(14):2690–2693, April 1997.

[39] Gerhard Hummer and Attila Szabo. Free energy profiles from single-molecule pulling experiments. Proceedings of the National Academy of Sciences of the United States of America, 107(50):21441–21446, 2010.

[40] C. Rivetti, M. Guthold, and C. Bustamante. Scanning force microscopy of DNA deposited onto mica: Equilibration versus kinetic trapping studied by statistical polymer chain analysis. Journal of Molecular Biology, 264(5):919–932, December 1996. WOS:A1996VZ95100007.

[41] Hugo K. Christenson and Neil H. Thomson. The nature of the air-cleaved mica surface. Surface Science Reports, 71(2):367–390, June 2016.

[42] P. K. Hansma, J. P. Cleveland, M. Radmacher, D. A. Walters, P. E. Hillner, M. Bezanilla, M. Fritz, D. Vie, H. G. Hansma, C. B. Prater, J. Massie, L. Fukunaga, J. Gurley, and V. Elings. Tapping mode atomic force microscopy in liquids. Applied Physics Letters, 64(13):1738–1740, March 1994.

[43] A. L. Weisenhorn, P. K. Hansma, T. R. Albrecht, and C. F. Quate. Forces in atomic force microscopy in air and water. Applied Physics Letters, 54(26):2651–2653, June 1989.

[44] H G Hansma, R L Sinsheimer, M Q Li, and P K Hansma. Atomic force microscopy of single- and double-stranded DNA. Nucleic Acids Research, 20(14):3585–3590, July 1992.

[45] N. H. Thomson, S. Kasas, Smith, H. G. Hansma, and P. K. Hansma. Reversible Binding of DNA to Mica for AFM Imaging. Langmuir, 12(24):5905–5908, January 1996.

[46] Magdalena Bezanilla, Srinivas Manne, Daniel E. Laney, Yuri L. Lyubchenko, and Helen G. Hansma. Adsorption of DNA to Mica, Silylated Mica, and Minerals: Characterization by Atomic Force Microscopy. Langmuir, 11(2):655–659, February 1995.

[47] H G Hansma and D E Laney. DNA binding to mica correlates with cationic radius: assay by atomic force microscopy. Biophysical Journal, 70(4):1933–1939, April 1996.

[48] Yuri L. Lyubchenko and Luda S. Shlyakhtenko. AFM for analysis of structure and dynamics of DNA and protein–DNA complexes. Methods, 47(3):206–213, March 2009.

[49] Qi Zhang, Jasna Brujic, and Eric Vanden-Eijnden. Reconstructing Free Energy Profiles from Nonequilibrium Relaxation Trajectories. Journal of Statistical Physics, 144(2):344–366, 2011.

[50] Gavin E. Crooks. Entropy production fluctuation theorem and the nonequilibrium work relation for free energy differences. Physical Review E, 60(3):2721–2726, September 1999.

[51] D. Collin, F. Ritort, C. Jarzynski, S. B. Smith, I. Tinoco, and C. Bustamante. Verification of the Crooks fluctuation theorem and recovery of RNA folding free energies. Nature, 437(7056):231–234, September 2005.

[52] Olga Dudko. Intrinsic Rates and Activation Free Energies from Single-Molecule Pulling Experiments. Physical Review Letters, 96(10), 2006.

[53] J. N. Onuchic, Z. LutheySchulten, and P. G. Wolynes. Theory of protein folding: The energy landscape perspective. Annual Review of Physical Chemistry, 48:545–600, 1997. WOS:A1997YB98900019.

[54] J. N. Onuchic and P. G. Wolynes. Theory of protein folding. Current Opinion in Structural Biology, 14(1):70–75, 2004.

[55] Ken A. Dill, S. Banu Ozkan, M. Scott Shell, and Thomas R. Weikl. The Protein Folding Problem. Annual Review of Biophysics, 37(1):289–316, May 2008.

[56] E. Evans. Energy landscapes of biomolecular adhesion and receptor anchoring at interfaces explored with dynamic force spectroscopy. Faraday Discussions, (111):1–16, 1998.

[57] Gerhard Hummer and Attila Szabo. Free energy reconstruction from nonequilibrium single-molecule pulling experiments. Proceedings of the National Academy of Sciences of the United States of America, 98(7):3658–3661, March 2001.

[58] J. P. Hobbs, M. Anand, and B. A. Campion. Fluorinated High-Density Polyethylene Barrier Containers. In Barrier Polymers and Structures, volume 423 of ACS Symposium Series, pages 280–294. American Chemical Society, May 1990.

[59] Wei Wang. Protein aggregation and its inhibition in biopharmaceutics. International Journal of Pharmaceutics, 289(1-2):1–30, January 2005.

[60] S. Nema and Ke Avis. Freeze-Thaw Studies of a Model Protein, Lactate-Dehydrogenase, in the Presence of Cryoprotectants. Journal of Parenteral Science and Technology, 47(2):76–83, April 1993. WOS:A1993LX95900006.

[61] W. W. Cleland. Dithiothreitol, a New Protective Reagent for SH Groups*. Biochemistry, 3(4):480–482, April 1964.

[62] Artur Kr żel, Wojciech Leśniak, Małgorzata Jeżowska-Bojczuk, Piotr Młynarz, Justyna Brasuñ, Henryk Kozłowski, and Wojciech Bal. Coordination of heavy metals by dithiothreitol, a commonly used thiol group protectant. Journal of Inorganic Biochemistry, 84(1):77–88, March 2001.

[63] Wolfgang Walther, Ulrike Stein, Carsten Voss, Torsten Schmidt, Martin Schleef, and Peter M

Schlag. Stability analysis for long-term storage of naked DNA: impact on nonviral in vivo gene transfer. Analytical Biochemistry, 318(2):230–235, July 2003.

[64] Darryl L. Davis, Edward P. O'Brie, and Catherine M. Bentzley. Analysis of the Degradation of Oligonucleotide Strands During the Freezing/Thawing Processes Using MALDI-MS. Analytical Chemistry, 72(20):5092–5096, October 2000.

[65] J. P. Cleveland, S. Manne, D. Bocek, and P. K. Hansma. A nondestructive method for determining the spring constant of cantilevers for scanning force microscopy. Review of Scientific Instruments, 64(2):403–405, February 1993.

[66] Paul A. Wiggins, Thijn Van Der Heijden, Fernando Moreno-herrero, Andrew Spakowitz, Rob Phillips, Jonathan Widom, Cees Dekker, and Philip C. Nelson. High flexibility of DNA on short length scales probed by atomic force microscopy. Nature Nanotechnology, 1(2):137–41, November 2006.

[67] Peter Markiewicz and M. Cynthia Goh. Atomic force microscopy probe tip visualization and improvement of images using a simple deconvolution procedure. Langmuir, 10(1):5–7, January 1994.

[68] Nagaraju Chada, Krishna P. Sigdel, Raghavendar Reddy Sanganna Gari, Tina Rezaie Matin, Linda L. Randall, and Gavin M. King. Glass is a Viable Substrate for Precision Force Microscopy of Membrane Proteins. Scientific Reports, 5:12550, July 2015.

[69] Robert Walder, Marc-André LeBlanc, William J. Van Patten, Devin T. Edwards, Jacob A. Greenberg, Ayush Adhikari, Stephen R. Okoniewski, Ruby May A. Sullan, David Rabuka, Marcelo C. Sousa, and Thomas T. Perkins. Rapid Characterization of a Mechanically Labile -Helical Protein Enabled by Efficient Site-Specific Bioconjugation. Journal of the American Chemical Society, 139(29):9867–9875, July 2017.

[70] Robert Walder, William J. Van Patten, Ayush Adhikari, and Thomas T. Perkins. Going Vertical To Improve the Accuracy of Atomic Force Microscopy Based Single-Molecule Force Spectroscopy. ACS Nano, 12(1):198–207, January 2018.

[71] Abraham. Savitzky and M. J. E. Golay. Smoothing and Differentiation of Data by Simplified Least Squares Procedures. Analytical Chemistry, 36(8):1627–1639, July 1964.

[72] Hao Yu, Matthew G. W. Siewny, Devin T. Edwards, Aric W. Sanders, and Thomas T. Perkins. Hidden dynamics in the unfolding of individual bacteriorhodopsin proteins. Science, 355(6328):945–950, March 2017.

[73] Patrick R. Heenan and Thomas T. Perkins. Imaging DNA Equilibrated onto Mica in Liquid Using Biochemically Relevant Deposition Conditions. ACS Nano, 13(4):4220–4229, April 2019.

[74] Yanwei Wang, Shiyong Ran, and Guangcan Yang. Single molecular investigation of DNA looping and aggregation by restriction endonuclease BspMI. Scientific Reports, 4, July 2014.

[75] Divakaran Murugesapillai, Micah J. McCauley, Ran Huo, Nelson Holte, Molly H, Armen Stepanyants, L. James Maher, Nathan E. Israeloff, and Mark C. Williams. DNA bridging and looping by HMO1 provides a mechanism for stabilizing nucleosome-free chromatin. Nucleic Acids Research, 42(14):8996–9004, August 2014.

[76] Maria V. Sukhanova, Sanae Abrakhi, Vandana Joshi, David Pastre, Mikhail M. Kutuzov, Rashid O. Anarbaev, Patrick A. Curmi, Loic Hamon, and Olga I. Lavrik. Single molecule detection of PARP1 and PARP2 interaction with DNA strand breaks and their poly(ADP-ribosyl)ation using high-resolution AFM imaging. Nucleic Acids Research, 44(6):e60–e60, April 2016.

[77] M. Bezanilla, B. Drake, E. Nudler, M. Kashlev, P. K. Hansma, and H. G. Hansma. Motion and enzymatic degradation of DNA in the atomic force microscope. Biophysical Journal, 67(6):2454–2459, December 1994.

[78] Aleksandre Japaridze, Dusan Vobornik, Ewelina Lipiec, Andrea Cerreta, Jacek Szczerbinski, Renato Zenobi, and Giovanni Dietler. Toward an Effective Control of DNA's Submolecular Conformation on a Surface. Macromolecules, 49(2):643–652, January 2016.

[79] David Pastré, Olivier Piétrement, Stéphane Fusil, Fabrice Landousy, Josette Jeusset, Marie-Odile David, Loïc Hamon, Eric Le Cam, and Alain Zozime. Adsorption of DNA to Mica Mediated by Divalent Counterions: A Theoretical and Experimental Study. Biophysical Journal, 85(4):2507–2518, October 2003.

[80] Olivier Piétrement, David Pastré, Stéphane Fusil, Josette Jeusset, Marie-Odile David, Fabrice Landousy, Loïc Hamon, Alain Zozime, and Eric Le Cam. Reversible Binding of DNA on NiCl2-Treated Mica by Varying the Ionic Strength. Langmuir, 19(7):2536–2539, April 2003.

[81] Alice Pyne, Ruth Thompson, Carl Leung, Debdulal Roy, and Bart W. Hoogenboom. Single-Molecule Reconstruction of Oligonucleotide Secondary Structure by Atomic Force Microscopy. Small, 10(16):3257–3261, August 2014.

[82] L. S. Shlyakhtenko. Structure and dynamics of three-way DNA junctions: atomic force microscopy studies. Nucleic Acids Research, 28(18):3472–3477, September 2000.

[83] Yuri L. Lyubchenko, Luda S. Shlyakhtenko, and Alexander A. Gall. Atomic Force Microscopy Imaging and Probing of DNA, Proteins, and Protein-DNA Complexes: Silatrane Surface Chemistry. In DNA-Protein Interactions, Methods in Molecular Biology™, pages 337–351. Humana Press, 2009.

[84] Pj Hagerman. Flexibility of Dna. Annual Review of Biophysics and Biophysical Chemistry, 17:265–286, 1988. WOS:A1988P532200012.

[85] Willem Vanderlinden and Steven De Feyter. Chain relaxation dynamics of DNA adsorbing at a solid–liquid interface. Nanoscale, 5(6):2264, 2013.

[86] D. J. Billingsley, A. J. Lee, N. A. B. Johansson, A. Walton, L. Stanger, N. Crampton, W. A.

Bonass, and N. H. Thomson. Patchiness of ion-exchanged mica revealed by DNA binding dynamics at short length scales. Nanotechnology, 25(2):025704, 2014.

[87] M. L. Sushko, A. L. Shluger, and C. Rivetti. Simple model for DNA adsorption onto a mica surface in 1 : 1 and 2 : 1 electrolyte solutions. Langmuir, 22(18):7678–7688, August 2006. WOS:000239921800033.

[88] Andrew J. Lee, Michal Szymonik, Jamie K. Hobbs, and Christoph Wälti. Tuning the translational freedom of DNA for high speed AFM. Nano Research, 8(6):1811–1821, June 2015.

[89] Valeria Cassina, Davide Seruggia, Giovanni Luca Beretta, Domenico Salerno, Doriano Brogioli, Stefano Manzini, Franco Zunino, and Francesco Mantegazza. Atomic force microscopy study of DNA conformation in the presence of drugs. European Biophysics Journal, 40(1):59–68, January 2011.

[90] L. D. Landau and E. M. Lifshits. Statistical physics. Number v. 5 in Their Course of theoretical physics, v. 5. Pergamon Press ; Addison-Wesley Pub. Co, London : Reading, Mass, 1958.

[91] S. B. Smith, L. Finzi, and C. Bustamante. Direct mechanical measurements of the elasticity of single DNA molecules by using magnetic beads. Science, 258(5085):1122–1126, November 1992.

[92] C. Bustamante, J. F. Marko, E. D. Siggia, and S. Smith. Entropic elasticity of lambda-phage DNA. Science, 265(5178):1599–1600, September 1994.

[93] A. Bensimon, A. Simon, A. Chiffaudel, V. Croquette, F. Heslot, and D. Bensimon. Alignment and sensitive detection of DNA by a moving interface. Science, 265(5181):2096–2098, September 1994.

[94] D. Bensimon, A. J. Simon, V. Croquette, and A. Bensimon. Stretching DNA with a Receding Meniscus: Experiments and Models. Physical Review Letters, 74(23):4754–4757, June 1995.

[95] Richard R. Sinden. DNA structure and function. Academic Press, San Diego, 1994.

[96] Jianxun Mou, Daniel M. Czajkowsky, Yiyi Zhang, and Zhifeng Shao. High-resolution atomic-force microscopy of DNA: the pitch of the double helix. FEBS Letters, 371(3):279–282, September 1995.

[97] Shinichiro Ido, Kenjiro Kimura, Noriaki Oyabu, Kei Kobayashi, Masaru Tsukada, Kazumi Matsushige, and Hirofumi Yamada. Beyond the Helix Pitch: Direct Visualization of Native DNA in Aqueous Solution. ACS Nano, 7(2):1817–1822, February 2013.

[98] Kfir Kuchuk and Uri Sivan. Hydration Structure of a Single DNA Molecule Revealed by Frequency-Modulation Atomic Force Microscopy. Nano Letters, 18(4):2733–2737, April 2018.

[99] D. Rhodes and A. Klug. Helical periodicity of DNA determined by enzyme digestion. Nature, 286(5773):573–578, August 1980.

[100] Christoph G. Baumann, Steven B. Smith, Victor A. Bloomfield, and Carlos Bustamante. Ionic effects on the elasticity of single DNA molecules. Proceedings of the National Academy of Sciences, 94(12):6185–6190, June 1997.

[101] Torunn Berge, Darren J. Ellis, David T.F. Dryden, J.Michael Edwardson, and Robert M. Henderson. Translocation-Independent Dimerization of the EcoKI Endonuclease Visualized by Atomic Force Microscopy. Biophysical Journal, 79(1):479–484, July 2000.

[102] Kelly J. Neaves, Laurie P. Cooper, John H. White, Stewart M. Carnally, David T. F. Dryden, J. Michael Edwardson, and Robert M. Henderson. Atomic force microscopy of the EcoKI Type I DNA restriction enzyme bound to DNA shows enzyme dimerization and DNA looping. Nucleic Acids Research, 37(6):2053–2063, April 2009.

[103] Abigail J. Bath, Susan E. Milsom, Niall A. Gormley, and Stephen E. Halford. Many Type IIs Restriction Endonucleases Interact with Two Recognition Sites before Cleaving DNA. Journal of Biological Chemistry, 277(6):4024–4033, February 2002.

[104] Jochen Felix Kepert, Katalin Fejes Tóth, Maïwen Caudron, Norbert Mücke, Jörg Langowski, and Karsten Rippe. Conformation of Reconstituted Mononucleosomes and Effect of Linker Histone H1 Binding Studied by Scanning Force Microscopy. Biophysical Journal, 85(6):4012–4022, December 2003.

[105] Luda S. Shlyakhtenko, Alexander Y. Lushnikov, and Yuri L. Lyubchenko. Dynamics of Nucleosomes Revealed by Time-Lapse Atomic Force Microscopy. Biochemistry, 48(33):7842–7848, August 2009.

[106] Xueyin Wang, Richard D. Paucek, Anne R. Gooding, Zachary Z. Brown, Eva J. Ge, Tom W. Muir, and Thomas R. Cech. Molecular analysis of PRC2 recruitment to DNA in chromatin and its inhibition by RNA. Nature Structural and Molecular Biology, page nsmb.3487, October 2017.

[107] Yuri L. Lyubchenko, Luda S. Shlyakhtenko, and Toshio Ando. Imaging of nucleic acids with atomic force microscopy. Methods, 54(2):274–283, June 2011.

[108] Daniel J Müller and Andreas Engel. Atomic force microscopy and spectroscopy of native membrane proteins. Nature Protocols, 2(9):2191–2197, September 2007.

[109] Daniel J. Müller, Dimitrios Fotiadis, Simon Scheuring, Shirley A. Müller, and Andreas Engel. Electrostatically Balanced Subnanometer Imaging of Biological Specimens by Atomic Force Microscope. Biophysical Journal, 76(2):1101–1111, February 1999.

[110] Patrick R. Heenan and Thomas T. Perkins. FEATHER: Automated Analysis of Force Spectroscopy Unbinding and Unfolding Data via a Bayesian Algorithm. Biophysical Journal, 115(5):757–762, September 2018.

[111] E Evans and K Ritchie. Dynamic strength of molecular adhesion bonds. Biophysical Journal, 72(4):1541–1555, April 1997.

[112] E Evans and K Ritchie. Strength of a weak bond connecting flexible polymer chains. Biophysical Journal, 76(5):2439–2447, May 1999.

[113] Patrick D. Bosshart, Patrick L.T.M. Frederix, and Andreas Engel. Reference-Free Alignment and Sorting of Single-Molecule Force Spectroscopy Data. Biophysical Journal, 102(9):2202–2211, May 2012.

[114] M. Kuhn, H. Janovjak, M. Hubain, and D. J. Müller. Automated alignment and pattern recognition of single-molecule force spectroscopy data. Journal of Microscopy, 218(2):125–132, May 2005.

[115] C Gergely, B Senger, J. C Voegel, J. K. H Hörber, P Schaaf, and J Hemmerlé. Semi-automatized processing of AFM force-spectroscopy data. Ultramicroscopy, 87(1–2):67–78, March 2001.

[116] Charles Roduit, Bhaskar Saha, Livan Alonso-sarduy, Andrea Volterra, Giovanni Dietler, and Sandor Kasas. OpenFovea: open-source AFM data processing software. Nature Methods; New York, 9(8):774–5, August 2012.

[117] Sandor Kasas, Beat M. Riederer, Stefan Catsicas, Brunero Cappella, and Giovanni Dietler. Fuzzy logic algorithm to extract specific interaction forces from atomic force microscopy data. Review of Scientific Instruments, 71(5):2082–2086, May 2000.

[118] Xavier García-Massó, Matthias C. Huber, Jacqueline. Friedmann, Luis M. Gonzalez, Stefan M. Schiller, and José L. Toca-Herrera. Automated detection of protein unfolding events in atomic force microscopy force curves. Microscopy Research and Technique, 79(11):1105–1111, November 2016.

[119] R. Benítez and V. J. Bolós. Searching events in AFM force-extension curves: A wavelet approach. Microscopy Research and Technique, 80(1):153–159, January 2017.

[120] Nicola Galvanetto, Andrea Perissinotto, Andrea Pedroni, and Vincent Torre. Fodis: Software for Protein Unfolding Analysis. Biophysical Journal, 114(6):1264–1266, March 2018.

[121] Kostyantyn R. Partola and George Lykotrafitis. FRAME (Force Review Automation Environment): MATLAB-based AFM data processor. Journal of Biomechanics; Kidlington, 49(7):1221–1224, 2016.

[122] Yi Cao, Rachel Kuske, and Hongbin Li. Direct Observation of Markovian Behavior of the Mechanical Unfolding of Individual Proteins. Biophysical Journal, 95(2):782–788, July 2008.

[123] Jim Pitman. Probability. Springer texts in statistics. Springer-Verlag, New York, 1993.

[124] Eric Jones, Travis Oliphant, Pearu Peterson, and others. SciPy: Open source scientific tools for Python. 2001.

[125] A. Bhattacharyya. On a Measure of Divergence between Two Multinomial Populations. Sankhyā: The Indian Journal of Statistics (1933-1960), 7(4):401–406, 1946.

[126] Devin T. Edwards, Jaevyn K. Faulk, Marc-André LeBlanc, and Thomas T. Perkins. Force Spectroscopy with 9- s Resolution and Sub-pN Stability by Tailoring AFM Cantilever Geometry. Biophysical Journal, 113(12):2595–2600, December 2017.

[127] Matthew S. Bull, Ruby May A. Sullan, Hongbin Li, and Thomas T. Perkins. Improved Single Molecule Force Spectroscopy Using Micromachined Cantilevers. ACS Nano, 8(5):4984–4995, May 2014.

[128] John F. Marko and Eric D. Siggia. Stretching DNA. Macromolecules, 28(26):8759–8770, December 1995.

[129] P. Dierckx. An algorithm for smoothing, differentiation and integration of experimental data using spline functions. Journal of Computational and Applied Mathematics, 1(3):165–184, September 1975.

[130] Mehryar Mohri, Afshin Rostamizadeh, and Ameet Talwalkar. Foundations of machine learning. Adaptive computation and machine learning. The MIT Press, Cambridge, Massachusetts, second edition edition, 2018. OCLC: 1041560990.

[131] Allison B. Churnside, Ruby May A. Sullan, Duc M. Nguyen, Sara O. Case, Matthew S. Bull, Gavin M. King, and Thomas T. Perkins. Routine and Timely Sub-picoNewton Force Stability and Precision for Biological Applications of Atomic Force Microscopy. Nano Letters, 12(7):3557–3561, July 2012.

[132] J. W. Bryson, J. R. Desjarlais, T. M. Handel, and W. F. DeGrado. From coiled coils to small globular proteins: design of a native-like three-helix bundle. Protein Science : A Publication of the Protein Society, 7(6):1404–1414, June 1998.

[133] Sehat Nauli, Brian Kuhlman, and David Baker. Computer-based redesign of a protein folding pathway. Nature Structural & Molecular Biology, 8(7):602–605, July 2001.

[134] R. Proksch, T. E. Schäffer, J. P. Cleveland, R. C. Callahan, and M. B. Viani. Finite optical spot size and position corrections in thermal spring constant calibration. Nanotechnology, 15(9):1344, 2004.

[135] M D Wang, H Yin, R Landick, J Gelles, and S M Block. Stretching DNA with optical tweezers. Biophysical Journal, 72(3):1335–1346, March 1997.

[136] Patrick R. Heenan, Hao Yu, Matthew G. W. Siewny, and Thomas T. Perkins. Improved free-energy landscape reconstruction of bacteriorhodopsin highlights local variations in unfolding energy. The Journal of Chemical Physics, 148(12):123313, December 2017.

[137] Ann Marie Stanley and Karen G. Fleming. Process of folding proteins into membranes: Challenges and progress. Archives of Biochemistry and Biophysics, 469(1):46–66, January 2008. WOS:000251824800006.

[138] Harald Janovjak, K. Tanuj Sapra, Alexej Kedrov, and Daniel J. Mueller. From valleys to

ridges: Exploring the dynamic energy landscape of single membrane proteins. Chemphyschem, 9(7):954–966, May 2008. WOS:000255845500001.

[139] Young Min Rhee and Vijay S. Pande. One-Dimensional Reaction Coordinate and the Corresponding Potential of Mean Force from Commitment Probability Distribution. The Journal of Physical Chemistry B, 109(14):6780–6786, April 2005.

[140] Christian A. Bippes and Daniel J. Muller. High-resolution atomic force microscopy and spectroscopy of native membrane proteins. Reports on Progress in Physics, 74(8):086601, 2011.

[141] F. Oesterhelt, D. Oesterhelt, M. Pfeiffer, A. Engel, H. E. Gaub, and D. J. Müller. Unfolding pathways of individual bacteriorhodopsins. Science (New York, N.Y.), 288(5463):143–146, April 2000.

[142] Jan Liphardt, Sophie Dumont, Steven B. Smith, Ignacio Tinoco, and Carlos Bustamante. Equilibrium information from nonequilibrium measurements in an experimental test of Jarzynski's equality. Science, 296(5574):1832–5, June 2002.

[143] Sanghyun Park, Fatemeh Khalili-Araghi, Emad Tajkhorshid, and Klaus Schulten. Free energy calculation from steered molecular dynamics simulations using Jarzynski's equality. The Journal of Chemical Physics, 119(6):3559–3566, July 2003.

[144] Johannes Preiner, Harald Janovjak, Christian Rankl, Helene Knaus, and et al. Free Energy of Membrane Protein Unfolding Derived from Single-Molecule Force Measurements. Biophysical Journal; New York, 93(3):930–7, August 2007.

[145] Devin T. Edwards, Jaevyn K. Faulk, Aric W. Sanders, Matthew S. Bull, Robert Walder, Marc-Andre LeBlanc, Marcelo C. Sousa, and Thomas T. Perkins. Optimizing 1- s-Resolution Single-Molecule Force Spectroscopy on a Commercial Atomic Force Microscope. Nano Letters, 15(10):7091–7098, October 2015.

[146] Devin T. Edwards and Thomas T. Perkins. Optimizing force spectroscopy by modifying commercial cantilevers: Improved stability, precision, and temporal resolution. Journal of Structural Biology, 197(1):13–25, January 2017.

[147] Megan C. Engel, Dustin B. Ritchie, Daniel A. N. Foster, Kevin S. D. Beach, and Michael T. Woodside. Reconstructing Folding Energy Landscape Profiles from Nonequilibrium Pulling Curves with an Inverse Weierstrass Integral Transform. Physical Review Letters, 113(23), 2014.

[148] Max Kessler, Kay E. Gottschalk, Harald Janovjak, Daniel J. Muller, and Hermann E. Gaub. Bacteriorhodopsin Folds into the Membrane against an External Force. Journal of Molecular Biology, 357(2):644–654, March 2006.

[149] David D. L. Minh and Artur B. Adib. Optimized Free Energies from Bidirectional Single-Molecule Force Spectroscopy. Physical Review Letters, 100(18):180602, May 2008.

[150] William H. Press, Brian P. Flannery, Saul A. Teukolsky, and William T. Vetterling. Numerical Recipes in C: The Art of Scientific Computing. Cambridge University Press, New York, NY, USA, 1988.

[151] Daniel J. Muller, Max Kessler, Filipp Oesterhelt, Clemens Moller, and et al. Stability of bacteriorhodopsin (alpha)-helices and loops analyzed by single-molecule force spectroscopy. Biophysical Journal; New York, 83(6):3578–88, December 2002.

[152] Florian Cymer, Gunnar von Heijne, and Stephen H. White. Mechanisms of Integral Membrane Protein Insertion and Folding. Journal of Molecular Biology, 427(5):999–1022, March 2015.

[153] Tatsuya Yamada, Takahisa Yamato, and Shigeki Mitaku. Forced Unfolding Mechanism of Bacteriorhodopsin as Revealed by Coarse-Grained Molecular Dynamics. Biophysical Journal, 111(10):2086–2098, November 2016.

[154] Stephen H. White and William C. Wimley. Membrane protein folding and stability: Physical principles. Annual Review of Biophysics and Biomolecular Structure; Palo Alto, 28:319, 1999.

[155] Zheng Cao, James M. Hutchison, Charles R. Sanders, and James U. Bowie. Backbone Hydrogen Bond Strengths Can Vary Widely in Transmembrane Helices. Journal of the American Chemical Society, 139(31):10742–10749, August 2017.

[156] L. Pauling and R. B. Corey. The Pleated Sheet, A New Layer Configuration of Polypeptide Chains. Proceedings of the National Academy of Sciences, 37(5):251–256, May 1951.

[157] Max Kessler and Hermann E. Gaub. Unfolding Barriers in Bacteriorhodopsin Probed from the Cytoplasmic and the Extracellular Side by AFM. Structure, 14(3):521–527, March 2006.

[158] J. Liphardt, B. Onoa, S. B. Smith, I. Tinoco, and C. Bustamante. Reversible unfolding of single RNA molecules by mechanical force. Science (New York, N.Y.), 292(5517):733–737, April 2001.

[159] C. Cecconi. Direct Observation of the Three-State Folding of a Single Protein Molecule. Science, 309(5743):2057–2060, September 2005.

[160] G. I. Bell. Models for the specific adhesion of cells to cells. Science, 200(4342):618–627, May 1978.